Universität Bonn

Physikalisches Institut

Construction and First Measurements of a GridPix based X-ray Detector

Christoph Krieger

Although the axion particle is not part of the standard model, it is predicted by some extensions to the standard model. In strong electric and magnetic fields photons can convert into axions and vice versa. Therefore, the sun is expected to be an axion source. Experiments looking for solar axions, such as the CERN Axion Solar Telescope (CAST), are called helioscopes. These experiments exploit the conversion of solar axions to photons in the low energy X-ray regime in strong magnetic fields. Because of small coupling constants axion events are expected to be rare so that X-ray detectors with extremely low background rates are required.
In this thesis a gaseous X-ray detector with a pixelized readout structure was constructed and tested. It is based on a combination of the Timepix ASIC with a Micromegas gas amplification stage, called GridPix. Characteristics of this detector such as energy resolution and gas amplification are studied. As the detector was designed to have low intrinsic background rates, these were measured for different shielding setups.

Physikalisches Institut der
Universität Bonn
Nußallee 12
D-53115 Bonn

BONN-IB-2012-05
Februar 2012

Universität Bonn

Physikalisches Institut

Construction and First Measurements of a GridPix based X-ray Detector

Christoph Krieger

Dieser Forschungsbericht wurde als Masterarbeit von der Mathematisch-Naturwissenschaftlichen Fakultät der Universität Bonn angenommen.

Angenommen am:	31.10.2011
Referent:	Prof. Dr. Klaus Desch
Koreferent:	Prof. Dr. Hartmut Schmieden

Contents

Chapter 1

Introduction

All through man's history mankind has increased its knowledge about the universe. Starting with first astronomical observations in early centuries by going through several discoveries of new phenomena, anomalies and physics laws the understanding of processes in the universe and the universe itself have been rising with time.

But still the universe as we observe it cannot be explained fully by what we know. The fact that the universe is almost flat requires an energy density in the universe which is much higher than the energy density derived from baryonic matter which can be observed in the universe. From various observations, such as the shape of galaxies or the rotational velocities in spiral arms of galaxies which do not decrease with the distance from the center but stay constant, one has to conclude that a large amount of matter has to exist which we cannot see.

Results of the **W**ilkinson **M**icrowave **A**nisotropy **P**robe (WMAP) experiment [1] which looked for anisotropies in the cosmic microwave background by precisely mapping it, hint at the hypothesis that the total energy density in the universe is dominated by two contributions, dark energy and dark matter. While only few things are known about dark energy despite the fact that it is the largest contribution to the energy density of the universe. For dark matter some candidates already exist. Dark matter has to couple gravitationally otherwise we would not observe its influence on e.g. the shape of the universe. Also it has to be electrical neutral as else it would couple to photons and we could 'see' it. Its couplings to known types of matter has to be weak. Dark matter particles have to be stable or at least their lifetime has to be at the order of the age of the universe.

One possible component for dark matter is the axion. This particle is introduced at the solution of the strong CP-problem by the Peccei-Quinn mechanism [2] and fits the requirements of a dark matter candidate. One approach for detecting axions is to look for axions generated in the sun. These could convert into photons inside a strong magnetic field. This is done at the **C**ERN **A**xion **S**olar **T**elescope (CAST). The rate of photons originating from converted axions is very low. Therefore one needs (in case of CAST) x-ray detectors with very low background rates to be able to detect axions or at least to set upper limits on their mass and couplings.

In this thesis a gaseous x-ray detector was constructed and tested which uses a GridPix as gas amplification and readout structure. GridPix is a combination of a pixelized readout with Micromegas like gas amplification structure. The latter one is fabricated on the pixelized readout by means of photolithographic postprocessing. GridPix based detectors deliver high spatial resolution in combination with the capability of detecting single electrons. The high spatial resolution can be deployed for an improved event shape analysis which can be used for discriminating background events. As this detector is a first test for a GridPix based low background detector, this thesis is a first study for a future CAST detector. The detector was set up and characterized in measurements. In addition first background rates were measured employing different shielding.

Chapter 2

Axions and the CERN Axion Solar Telescope

The detector constructed and tested in this thesis is a study for a new x-ray detector of the CAST experiment (CERN Axion Solar Telescope). Since the requirements on the detector are derived from a potential operation in CAST, a short introduction of the physics of this experiment will be given in this chapter. Additionally, the CAST experiment itself will be presented. The requirements on the detector will be discussed later in chapter 5 in combination with a description of the detector itself.

2.1 Axions

The possible existence of axions arises from the most elegant way of solving the CP-problem of strong interaction. This section will give a short summary of the CP-problem, its consequences and a solution by introducing the axion.

2.1.1 CP-problem of the strong interaction

The strong interaction is described by the theory of Quantum Chromodynamics (QCD) which describes the interactions of quarks and gluons where the gluons are the mediator bosons of the interaction. They can selfinteract as they carry color charge different from the photons as mediators of the electromagnetic interaction which do not carry electromagnetic charge. One can write the Lagrangian of QCD in the following way

$$\mathcal{L}_{\mathrm{QCD}} = \sum_n \bar{q}_n(\gamma^\mu i D_\mu - m_n)q_n - \frac{1}{4}G^a_{\mu\nu}G_a^{\mu\nu} \tag{2.1}$$

where q_n are the quark fields with quark flavor n, m_n the quark masses and G_a the gluon field tensors with color index $a = 1 \ldots 8$. D_μ is the covariant derivative which is defined as

$$D_\mu = \partial_\mu - igT^a G^a_\mu \tag{2.2}$$

with g the coupling constant and T^a the generators of the group SU(3).

This Lagrangian is invariant under global axial and vector transformations in case of vanishing quark masses. The invariance under vector transformations leads to conservation of the baryon number and is experimentally confirmed. The invariance under axial transformations ($\mathrm{U(1)_A}$) would lead to symmetry between left and right handed quarks of which no evidence has been found so far in nature. The spontaneous breaking of $\mathrm{U(1)_A}$ gives rise to the existence of eight massless Goldstone bosons. For non vanishing quark masses these Goldstone bosons acquire mass. This pseudoscalar octet can be identified with the experimentally observed bosons π, K and η. But also the existence of another light (mass $\leq \sqrt{3}m_\pi$) isoscalar pseudoscalar particle is predicted. From view of quantum numbers the best candidate is the η', but it is much too heavy ($m_{\eta'} = 957.78\,\mathrm{MeV}/c^2$ while $m_\pi \sim 135\,\mathrm{MeV}/c^2$). This is known as the $\mathrm{U(1)_A}$ problem [3].

The $U(1)_A$ problem can be solved by introducing an anomalous breaking of $U(1)_A$ [4, 5]. This results in an additional term $\mathcal{L}_\theta$ which adds to $\mathcal{L}_{QCD}$

$$\mathcal{L}_\theta = \theta \frac{g^2}{32\pi^2} G^a_{\mu\nu} \tilde{G}^{\mu\nu}_a \tag{2.3}$$

where g is the coupling constant and $G^a_{\mu\nu}$ the field strength tensor of the gluons with $\tilde{G}^{\mu\nu}_a$ its dual which is given by

$$\tilde{G}^{\mu\nu}_a = \frac{1}{2} \epsilon^{\mu\nu\rho\sigma} G^a_{\rho\sigma} \tag{2.4}$$

and θ is an arbitrary parameter between 0 and 2π. Taking into account electroweak interactions one has to replace θ with $\bar{\theta}$.

$$\bar{\theta} = \theta + \theta_{\text{weak}} \tag{2.5}$$

With $\mathcal{L}_{\bar{\theta}}$ added to $\mathcal{L}_{QCD}$ the Lagrangian of strong interaction looses its invariance under CP-transformations. Therefore, one would expect large CP violation in strong interaction unless $\bar{\theta}$ would be very small. The CP violation in the strong interaction was not observed in experiments.

The term $\mathcal{L}_{\bar{\theta}}$ also leads to an electric dipole moment d_n for the neutron which is related with the parameter $\bar{\theta}$ and should be at the order of $d_n \sim \bar{\theta} \times 10^{-16}\, e\,\text{cm}$ [6] while experiments set a bound of $|d_n| < 2.9 \times 10^{-26}\, e\,\text{cm}$ [7]. Therefore, $\bar{\theta}$ would have to be below 10^{-10} or the two contributions to $\bar{\theta}$ (equation 2.5) would have to be both very small or they would have to cancel each other. A very small value for $\bar{\theta}$ is not forbidden but it would result in fine-tuning the two parameters contributing to it and of course there is so far no physics reason why the strong interaction should not violate CP as it is not forbidden from the theory itself. The question why the parameter $\bar{\theta}$ is of such small value is also known as the strong CP problem.

There are three possible solutions to this problem. The first one eliminates the parameter θ from the Lagrangian by setting one of the quark masses to zero. However, one has to justify this with physics beyond the Standard model. The second approach just fixes θ to 0 which still does not cause $\bar{\theta}$ to vanish as θ_{weak} is still not zero. Also the latter approach causes other difficulties regarding the violation of weak CP. The third solution based on the Peccei-Quinn mechanism is a much more elegant way to solve the strong CP problem.

2.1.2 Where axions come in - The Peccei-Quinn mechanism

The solution using the Peccei-Quinn mechanism is in fact the most popular and most promising solution to the strong CP problem. It was introduced by Peccei and Quinn [2] in the year 1977. They introduced a new global, chiral symmetry $U(1)_{PQ}$ (Peccei-Quinn-Symmetry) which is spontaneously broken at an energy scale f_a. By introducing this symmetry, $\bar{\theta}$ becomes a dynamic variable of the theory instead of being a parameter of the theory. Therefore different values of $\bar{\theta}$ do not imply different theories anymore but different vacuum states of the given theory. By showing that $\bar{\theta} = 0$ is the true vacuum state one gets a quite elegant solution for the strong CP problem.

As the Peccei-Quinn mechanism is similar to the Higgs mechanism one also has to perform a spontaneous breaking of the symmetry where a Goldstone boson appears. This Goldstone boson is called axion and is massless and pseudoscalar. But through the axial anomaly and instanton interactions it acquires a small mass [8, 9]. The Lagrangian introducing the axion field a and describing the axions coupling to gluons is given by

$$\mathcal{L}_a = \frac{a}{f_a} \xi \frac{g^2}{32\pi^2} G^{\mu\nu}_b \tilde{G}^b_{\mu\nu} \tag{2.6}$$

here ξ denotes a theory parameter which model-dependent, f_a is the energy scale at which the Peccei-Quinn symmetry is broken and $G_b^{\mu\nu}$ is again the field strength tensor for gluons. This Lagrangian $\mathcal{L}_a$ represents the axions contribution to the effective potential of the QCD Lagrangian. Therefore, this potential is minimal at the expectation value $\langle a \rangle$ of the axion field which can be calculated as

$$\langle a \rangle = -\frac{f_a}{\xi}\bar{\theta} \tag{2.7}$$

which cancels the afore mentioned $\bar{\theta}$ term in the QCD Lagrangian [10]. Looking at the curvature of the effective potential around its minimum $\langle a \rangle$ it is possible to derive a relation for the axion mass.

$$m_a^2 = -\frac{\xi}{f_a}\frac{g^2}{32\pi^2}\frac{\partial}{\partial a}\left\langle G_b^{\mu\nu}\tilde{G}_{\mu\nu}^b\right\rangle\Big|_{\langle a\rangle=-\bar{\theta}f_a/\xi} \tag{2.8}$$

The experimental discovery of the axion would therefore be the ultimate proof for the Peccei-Quinn solution to the strong CP problem.

Just as an amusing fact, the pseudoscalar Goldstone boson which arises by the breaking of the Peccei-Quinn symmetry was named **axion** by Frank Wilczek after the american detergent axion, probably because it washes out the strong CP problem of QCD.

2.1.3 How do axions interact with normal matter?

The axion is a pseudoscalar particle. As it has not been observed experimentally yet, it is supposed to be of light mass and to have just weakly interactions with other matter. Its properties depend mainly on the energy scale f_a at which the Peccei-Quinn symmetry is broken. For describing the axion one needs its mass m_a and its couplings g_{ai} to other particles i. Both are antiproportional to f_a.

$$m_a \propto \frac{1}{f_a} \qquad g_{ai} \propto \frac{1}{f_a} \tag{2.9}$$

In the following the main interactions between axions and normal matter will be described. The major contribution which is common for most axion models are the couplings to gluons and photons, but also the coupling to fermions is present in some models. In all cases the coupling constants for the interactions with the different particles can be expressed as functions of the parameter f_a.

The coupling of axions to gluons is described by the interaction part of the Lagrangian

$$\mathcal{L}_{aG} = -\frac{\alpha_s}{8\pi f_a} a G_b^{\mu\nu}\tilde{G}_{\mu\nu}^b \tag{2.10}$$

where α_s denotes the finestructure constant of strong interactions. Due to its coupling to gluons the axion can mix with the neutral pion (see Feynman graph in figure 2.1) as they share the same quantum numbers. By means of the possible mixing of axion and the neutral pion one can express the axion mass in terms of the pion mass ($m_{\pi^0} = 135\,\mathrm{MeV}/c^2$) and its decay constant $f_{\pi^0} = 93\,\mathrm{MeV}/c^2$

$$m_a = \frac{m_{\pi^0} f_{\pi^0}}{f_a}\left(\frac{z}{(1+z+w)(1+z)}\right)^{1/2} \tag{2.11}$$

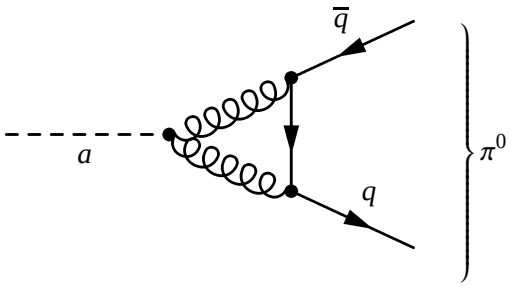

Figure 2.1: Feynman graph showing the mixing between the axion and the neutral pion by means of the axion-gluon coupling.

where z and w are the quark mass ratios which can be obtained experimentally [11].

$$z = m_u/m_d = 0.568 \pm 0.042 \tag{2.12}$$

$$w = m_u/m_s = 0.029 \pm 0.003 \tag{2.13}$$

Although these values vary depending on the model used one finds a rough estimate for the axion mass in dependence of f_a [10].

$$m_a \approx 0.6\,eV \frac{10^7\ \text{GeV}}{f_a} \tag{2.14}$$

As the axion can mix up with the neutral pion, a coupling of the axion to two photons (see figure 2.2a) is possible because the neutral pion couples to two photons. Therefore, the axion coupling to photons can be described by the Primakoff effect [10]. Therefore one gets

$$\mathcal{L}_{a\gamma} = -\frac{1}{4} g_{a\gamma} F_{\mu\nu} \tilde{F}^{\mu\nu} a = g_{a\gamma} \vec{E} \cdot \vec{B} a \tag{2.15}$$

where $g_{a\gamma}$ is the constant describing the coupling between axion and photons, again a is the axion field.

With α the fine structure constant one can express $g_{a\gamma}$ as

$$g_{a\gamma} = \frac{\alpha}{2\pi f_a} \left| \frac{E}{N} - \frac{2(4+z+w)}{3(1+z+w)} \right| \tag{2.16}$$

where E is the electromagnetic anomaly and N the color anomaly. However, in this case E/N represents a parameter which depends on the used axion model and varies between 0 and 6. If also a coupling between axions and fermions is present (which depends on the axion model) further contributions arise to the axion photon coupling as then the axion couples also to two photons by a fermion triangle as shown in figure 2.2b.

The coupling to fermions is possible if the axion model includes Peccei-Quinn charges (PQ charge) for the fermions. In this case the interaction is described by

$$\mathcal{L}_{af} = \frac{C_f}{2 f_a} \bar{\psi}_f \gamma^\mu \gamma_5 \psi_f \partial_\mu a = \frac{g_{af}}{2 m_f} \bar{\psi}_f \gamma^\mu \gamma_5 \psi_f \partial_\mu a \tag{2.17}$$

where C_f is the PQ charge of the fermion and $g_{af} = C_f m_f / f_a$ acts as coupling constant for a Yukawa coupling with a fermion of mass m_f.

As mentioned before axions have a coupling to two photons. Of course, one of the photons can also

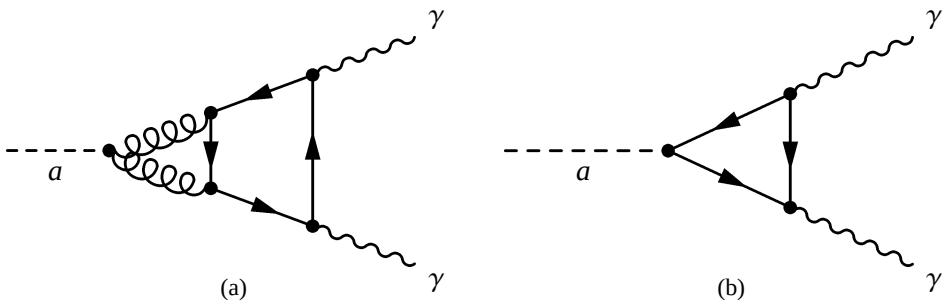

Figure 2.2: Feynman graphs for the coupling of the axion to two photons via its mixing with the neutral pion (a) and in case of axion-fermion coupling directly via a fermion triangle (b).

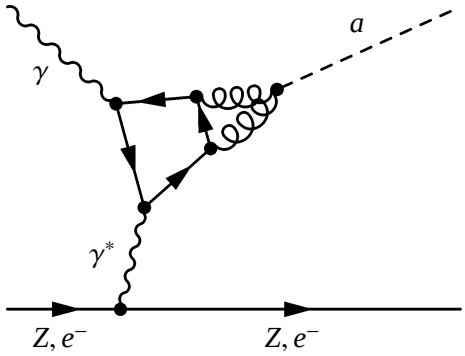

Figure 2.3: Feynman graph describing the Primakoff effect realized with the coupling of axion to gluons.

be virtual, therefore, it is possible for a photon to convert into an axion in presence of an electric or magnetic field. So, photons can convert into axions in the electric field of an nucleus. This is known as the Primakoff effect which is illustrated in the Feynman graph in figure 2.3. This effect is very important for the detection of axions as it is realized in all axion models which have all the coupling of axions to two photons at least via its coupling to gluons and its mixing with the neutral pion.

The axion models differ mainly by the implementation of the Peccei-Quinn mechanism, thus creating small differences in axion masses and coupling strengths. By using the energy scale f_a at which the Peccei-Quinn symmetry is broken, as a characteristic size (f_a determines mainly the axion mass and the coupling strengths) one can divide the different models into two main branches. Those with small f_a and therefore large m_a (visible axion models) and those with large f_a and therefore small axion mass m_a (invisible axion models).

The visible axion model was also the first axion model proposed by Peccei, Quinn, Weinberg and Wilczek [8, 9, 12] and assumes f_a to be less than 42 GeV which would lead to an axion mass of about 200 keV. As it would also imply rather large coupling constants this model would create an axion which should be rather simple to detect. But the visible axion model has already been ruled out by experiments and astrophysical considerations, as for example the estimation of the theoretical branching ratio of the K^+ decay into a positive charged pion and an axion which is about one order of magnitude higher than the experimentally obtained limit for this branching ration [13].

The invisible axion models use an energy scale f_a much larger than the energy scale of the symmetry breaking of the weak interaction f_{weak}. This leads to very weak interactions between axions and ordinary matter and of course to low axion masses which imply rather long lifetimes for axions. This already justifies the name invisible axion models as those axions would be very hard to detect in experiments. The two main models for invisible axions are the model introduced by Kim, Shifman, Vainshtein and

Zakharov (KSVZ model) [14, 15] and the one introduced by Dine, Fischler and Srednicki (DFSZ model) [16]. The main difference between these models is the coupling of axions to ordinary matter.

In the KSVZ model axions decouple completely from normal particles which means that interactions between axions and matter are realized only by the coupling between axions and gluon introduced by Peccei and Quinn which is generic to all axion models. The main drawback of the KSVZ model is that it needs an additional exotic quark which would couple directly to the axion and would therefore be involved in all loop interactions with axions. No evidence for this exotic quark has been found.

In contrast to the KSVZ model the DFSZ model does not need the introduction of such an exotic heavy quark. Couplings between axions and charged leptons as well as between axions and nucleons and photons are introduced instead by giving PQ charges to standard fermions. Therefore, the axion would couple directly to Standard model particles. The fact that the DFSZ model could easily be introduced in Grand Unified Theories makes this model rather attractive.

2.1.4 The axion as a dark matter candidate

As the entire universe is believed to be almost flat it is accepted in general that the observed mass and energy density in the universe does not suffice to create a universe as we observe it. The density contributions of baryonic matter, photons (mainly background radiation) and neutrinos add only up to 5% of the energy density necessary. Therefore, about 95% of the energy density come from unknown contributions of dark energy ($\sim$ 72%) and dark matter ($\sim$ 23%) [1]. Dark matter is of unknown nature but already many candidates exist for the dark matter to consist of. Just to mention two of them there are MAssive Compact Halo Objects (MACHOs) and Weakly Interacting Massive Particles (WIMPs). As candidates for dark matter are expected to be electrically and color neutral as well as to be of long lifetime and to only interact weakly the axion provides an attractive candidate for dark matter. Of course the axion could coexist with other dark matter candidates [10].

Looking at the axion lifetime determined by its decay into photons ($a \rightarrow \gamma\gamma$) one gets

$$\tau_a \approx 4.6 \times 10^{40}\,\mathrm{s}\left(\frac{E}{N} - 1.92\right)^{-2}\left(\frac{f_a/N}{10^{10}\,\mathrm{GeV}}\right)^{5} \tag{2.18}$$

so that for $E/N = 0$ and $f_a/N \geq 3 \times 10^5\,\mathrm{GeV}$ [17] the axion lifetime is longer than the age of the universe ($\sim 10^{17}\,\mathrm{s}$). With these values the axion mass would be lower than 20 eV which is also favored by astrophysical and cosmological constraints. Several of these constraints can also set upper limits on the coupling strengths of the axion to photons or other particles.

2.1.5 Detection of axions

The intuitive approach to search for axions is to make use of the Primakoff effect, respectively the inverse Primakoff effect. As photons can convert into axions in presence of virtual photons coming from external electric or magnetic fields, axions can be produced from photons in the Coulomb field of a nucleus, the electric field created by charged particles in a hot plasma or in magnetic fields. Axions can (re)convert to photons in such electric or magnetic field by the inverse Primakoff effect. Experimental approaches to search for invisible axions [18, 19] can be divided into three main branches:

- Axion haloscopes
- Axion helioscopes
- Laboratory experiments

While axion haloscopes are looking for axions with galactic origin, helioscopes are looking for axions produced in the sun by the Primakoff effect and laboratory experiments try to produce axions by guiding lasers in strong magnetic fields.

In case of axion haloscopes one uses in most cases microwave cavities. In these resonant cavities one can apply strong magnetic fields at a frequency determined by the cavity size. This would enhance the conversion of axions into photons for a narrow axion mass range. By changing the resonance frequency of the cavity (i.e changing its size) one can scan different axion mass regions. If axions would convert inside the cavity this would increase the number of photons inside which could be detected by sensitive microwave receivers as an increase of power inside the cavity. With axion haloscopes one can scan for axions in the μeV mass range. The Axion Dark Matter eXperiment (ADMX) located at Laurence Livermore National Laboratory could exclude axions in the mass window of [20, 21]

$$2.9\,\mu\text{eV} < m_a < 3.53\,\mu\text{eV}. \tag{2.19}$$

Laboratory experiments make use of the Primakoff effect by shining an intense laser beam into a strong magnetic field. A low amount of photons could convert into axions. To look for this conversion two approaches are possible. The conversion into axions and the reconversion back into photons during the beams propagation through the magnetic field should change the polarization of the beam which can be measured. Another way to look for invisible axions with lasers are the so-called shining-light-through-a-wall experiments or regeneration experiments. At this type of experiments a polarized laser beam guided through a transverse magnetic field is blocked by a wall. Photons converting into axions can propagate through the wall as invisible axions coupling to matter is quite weak. Behind the wall these axions can reconvert into photons which then can be detected. With the first experiment of this kind the Brookhaven-Fermilab-Rutherford-Trieste Collaboration could set an upper limit of [22]

$$g_{a\gamma} < 6.7 \times 10^{-7}\,\text{GeV}^{-1} \tag{2.20}$$

for axion masses lower than 1 μeV. Other experiments (also) looking for invisible axions with shining-light-through-a-wall experiments are OSQAR (**O**ptical **S**earch for **Q**ED v**A**cuum bi**R**efringence, Axions and photon Regeneration) located at CERN or the ALPS collaboration looking for **W**eakly **I**nteracting **S**ub-eV **P**articles (WISPs) using a HERA dipole magnet at DESY (**D**eutsches **E**lektronen **SY**nchrotron). One attractive advantage of the laboratory experiments is that they, in contrast to axion haloscopes and helioscopes, do not rely on models of the processes in stars.

Helioscope experiments use the sun as potential axion source as based on the well established Standard Solar Model the sun should produce axions in its core and therefore generate an axion flux towards the earth. The mean energy of axions in this flux is expected to be approximately 4 keV. This would result in an axion wavelength which is in the order of the lattice spacings in a crystal. So, one way to look for solar axions is to use the Bragg reflection with different crystals expecting a high signal if constructive interference takes place in the crystal. This technique has the advantage of being almost independent of the axion mass. Different experiments could therefore set an upper limit for the axions coupling to photons of [10]

$$g_{a\gamma} < 1.7 \times 10^{-9}\,\text{GeV}^{-1} \tag{2.21}$$

for axion masses lower than 1 keV. Another type of helioscope experiments use a strong magnet pointing towards the sun. Axions reconverting into photons inside the magnet would result in photons in the low x-ray regime. Therefore, at the end of the magnet x-ray detectors and sometimes also x-ray optics (telescopes) are used to detect the reconverted photons. Such devices are the most sensitive ones. The mass ranges in which these magnet helioscopes are sensitive is restricted by coherence conditions

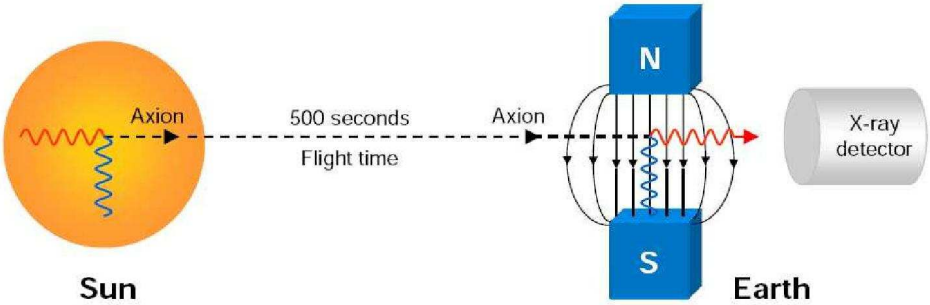

Figure 2.4: Working principle of magnet helioscopes, extracted from [10].

(mainly length of the magnet) and can go up to 1 eV. The working principle of magnet helioscopes is illustrated in figure 2.4. Magnet helioscopes could set the most stringent limits on the axion photon coupling:

- Lazurus et al. $g_{a\gamma} < 7.7 \times 10^{-9}\,\mathrm{GeV}^{-1}$ for $0.03\,\mathrm{eV} < m_a < 0.11\,\mathrm{eV}$ [23]
- Tokyo Axion Helioscope $g_{a\gamma} < 6.0 \times 10^{-10}\,\mathrm{GeV}^{-1}$ for $m_a < 0.03\,\mathrm{eV}$ [24]
- CERN Axion Solar Telescope $g_{a\gamma} < 8.8 \times 10^{-11}\,\mathrm{GeV}^{-1}$ for $m_a < 0.02\,\mathrm{eV}$ [25]
- CERN Axion Solar Telescope $g_{a\gamma} < 2.17 \times 10^{-10}\,\mathrm{GeV}^{-1}$ for $0.02\,\mathrm{eV} < m_a < 0.26\,\mathrm{eV}$ [26]

The CERN Axion Solar Telescope (CAST) has set the most stringent limits on the axion photon coupling and will be described in detail in the following section.

2.1.6 Axion flux from the sun

In the dense core of the sun photons can convert into axions via the Primakoff effect. In this case the conversion takes place in the electric field of the nuclei in the sun's core. Assuming the established Standard Solar Model and the axion photon interactions described in the section before one can derive the axion luminosity L_a and the differential solar axion flux $\frac{\mathrm{d}\Phi_a}{\mathrm{d}E_a}$ arriving at the earth [25]

$$L_a = g_{10}^2 \cdot 1.85 \times 10^{-3} \cdot L_{\mathrm{sun}} \tag{2.22}$$

$$\frac{\mathrm{d}\Phi_a}{\mathrm{d}E_a} = g_{10}^2 \cdot 6.02 \times 10^{10} \cdot E^{2.481} e^{-E/1.205} \mathrm{cm}^{-2}\mathrm{s}^{-1}\mathrm{keV}^{-1} \tag{2.23}$$

where E_a is the axion energy, L_{sun} the solar luminosity taken from [27] and $g_{10} \equiv g_{a\gamma} \cdot 10^{10}\,\mathrm{GeV}$. The differential flux in terms of g_{10}^2 is plotted in figure 2.5 as function of E_a showing the intensity maximum of the axion flux at 3 keV while one gets for the average axion energy $< E_a >$ a value of 4.2 keV. Integrating equation 2.23 delivers a total axion flux of

$$\Phi_a = g_{10}^2 \cdot 3.75 \times 10^{11}\,\mathrm{cm}^{-2}\,\mathrm{s}^{-1} \tag{2.24}$$

which is quite enormous even for $g_{a\gamma} < 10^{-12}\,\mathrm{GeV}^{-1}$ ($g_{10}^2 < 10^{-4}$) making the helioscope approach a promising technique for discovering (or excluding) the invisible axion in certain axion mass regions.

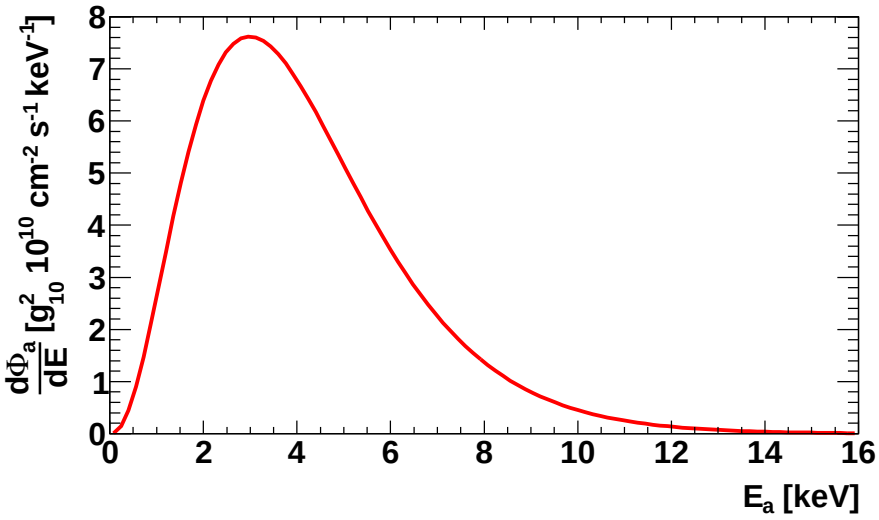

Figure 2.5: Differential solar axion flux (equation 2.23) arriving at the earth in terms of g_{10}^2 and as function of axion energy E_a.

2.1.7 Reconversion of axions into photons

When axions (e.g. originating from the sun) reach the earth they can reconvert to photons inside a magnetic field transverse to their propagation direction due to the inverse Primakoff effect. The probability for an axion with energy E_a to convert into a photon inside a magnetic field of field strength B is given by [18]

$$P_{a\to\gamma} = \left(\frac{Bg_{a\gamma}}{2}\right)^2 \frac{1}{q^2 + \Gamma^2/4}\left(1 + e^{-\Gamma L} - 2e^{-\Gamma L/2}\cos(qL)\right) \tag{2.25}$$

where L is the length of the magnetic field. Γ is the inverse absorption length for photons in the medium (e.g. a special gas) inside the magnetic field and q is the momentum difference between axion and photon. The photon has the same energy E_a as the axion from which it originated. The momentum difference q is given by

$$q = \frac{|m_a^2 - m_\gamma^2|}{2E_a} \tag{2.26}$$

with m_a the axion mass and m_γ the photon mass. If a medium is inside the magnetic field photons propagating through this medium acquire an effective mass which can be expressed with the plasma frequency inside the medium, using natural units:

$$m_\gamma^2 = \omega_{\mathrm{pl}}^2 = \frac{4\pi\alpha n_e}{m_e} \tag{2.27}$$

where m_e is the electron mass, α the fine structure constant and n_e the electron density in the medium. The conversion of axions into photons can only take place if the coherence condition $qL < \pi$ is fulfilled, i.e. that axions and photons are in phase along the distance L.

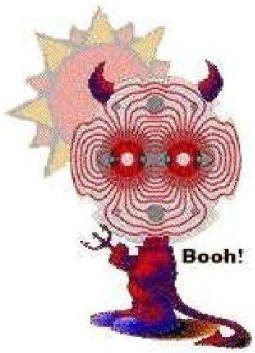

Figure 2.6: Logo of the CAST experiment, taken from [29].

In the case of vacuum inside the magnetic field m_γ vanishes and equation 2.25 simplifies to

$$P_{a\to\gamma} = \left(\frac{Bg_{a\gamma}}{2}\right)^2 \sin^2\left(\frac{qL}{2}\right) \tag{2.28}$$

with then $q = m_a^2/(2E_a)$.

The expected energy spectrum of the solar axions (figure 2.5) shows that the photons resulting from axion conversion inside the magnetic field will be dominantly in the low x-ray regime.

2.2 CERN Axion Solar Telescope

This section will describe the principle used for axion search at the **C**ERN **A**xion **S**olar **T**elescope (CAST) and the CAST experiment itself. Also an overview on the x-ray detectors used at CAST will be given. The logo of the CAST experiment is shown in figure 2.6. Just as a short side remark, in the first proposal [28] the experiment was named SATAN (**S**olar **A**xion **T**elescopic **AN**tenna) which may explain the CAST logo.

2.2.1 The CAST setup

The CAST experiment uses a decommissioned Large Hadron Collider prototype magnet [30, 31] which is mounted on a movable platform to track the sun. As the magnet is operated at cryogenic temperature ($\sim 1.8\,\mathrm{K}$) and therefore needs to be supplied with liquid helium the possible range of movement (especially tilting the magnet) is limited. Still it is possible to point the magnet towards the sun during sunrise and sunset for about 1.5 h each. The remaining time of the day the magnet rests in a defined position while the detectors are taking background or calibration data. The magnet has two bores each with a length of 9.26 m and an aperture of $14.5\,\mathrm{cm}^2$ which can be evacuated. It can create magnetic fields inside the bores of up to 9 T. Figure 2.7 shows a drawing of the CAST experimental setup whereas in figure 2.8 a photo of the CAST experimental area is shown.

The differential photon flux while tracking the sun can be derived from the solar axion flux (equation 2.23) and the probability for axions to convert into a photon (equation 2.25) by

$$\frac{\mathrm{d}\Phi_\gamma}{\mathrm{d}E} = \frac{\mathrm{d}\Phi_a}{\mathrm{d}E} P_{a\to\gamma}. \tag{2.29}$$

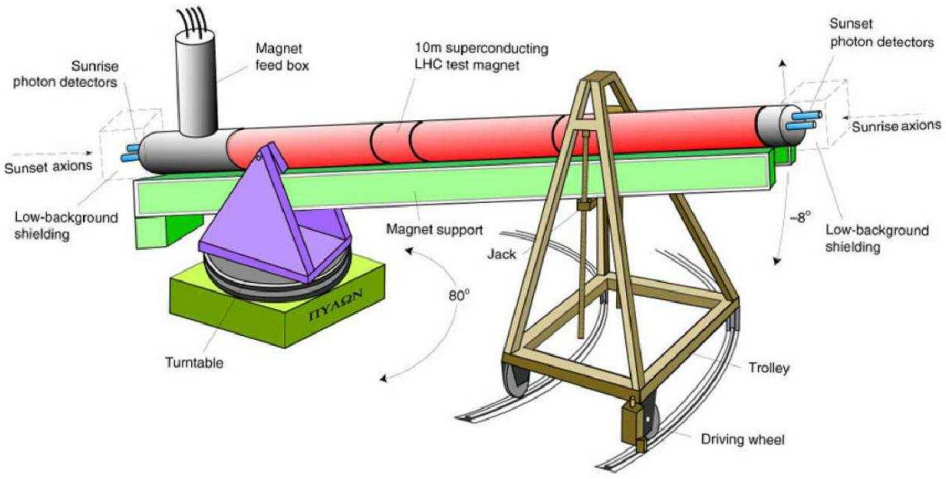

Figure 2.7: Drawing of the CAST experimental setup, extracted from [10].

Figure 2.8: Photo showing the CAST experimental area, taken from [6]. The (shielded) x-ray detectors are mounted at the ends of the magnet.

Inserting the magnet parameters of the CAST experiment and assuming coherent axion conversion ($qL < 1$) one gets [25]

$$\frac{\mathrm{d}\Phi_\gamma}{\mathrm{d}E} = 0.088\,\mathrm{cm}^{-2}\mathrm{d}^{-1}\mathrm{keV}^{-1} g_{10}^4 E^{2.481} e^{-E/1.205} \tag{2.30}$$

where the coherence condition is equivalent to axion masses below 0.02 eV. As the magnet bores are evacuated during operation they have to be sealed. But as the x-ray detectors are mounted at the end of the bores, the sealings have to be transparent for x-rays. To achieve this in coincidence with vacuum tightness special windows are used which consist of a very thin polypropylene foils (4 μm) and a strongback made of stainless steel. In its first operation phase (also called **CAST Phase I**) CAST could set the most stringent limits on the axion photon coupling for axion masses lower than 0.02 eV. For higher axion masses the conversion probability and, therefore, the experiments sensitivity drops dramatically (see figure 2.9). To recover the sensitivity for higher axion masses the magnet bores were filled with a buffer gas of low density. This rise to an effective photon mass extends the sensitivity beyond the established limits for a narrow axion mass region around the achieved photon mass. This retaining of sensitivity is also illustrated in figure 2.9. By rising the density of the buffer gas (rising its pressure

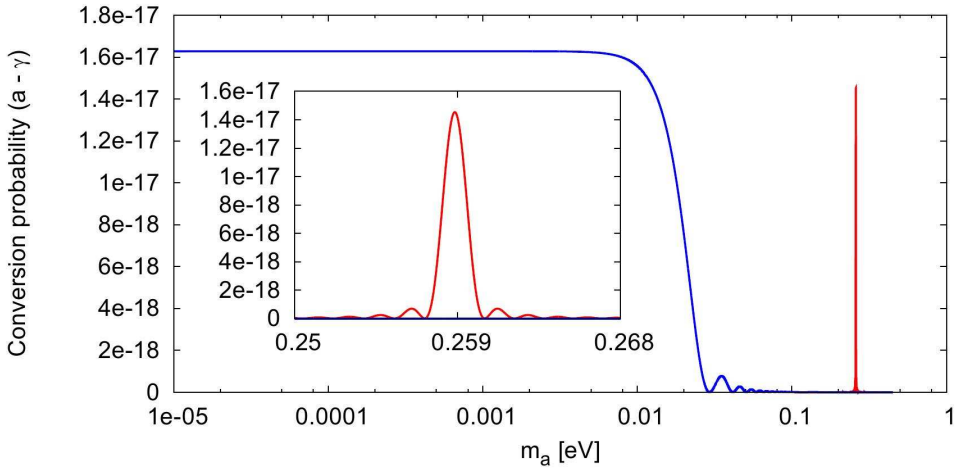

Figure 2.9: Axion conversion probability with and without buffer gas. Without buffer gas (blue) the conversion probability drops rapidly for axion masses larger than 0.01 eV. By using a buffer gas the probability can be restored for a narrow axion mass range (red, for use of ^{3}He at 6 mbar pressure). Taken from [10].

inside the bores) in steps which lead to overlapping axion mass regions one can scan higher axion mass regions. The effective photon mass for a certain buffer gas can be calculated with [10]

$$m_\gamma \approx 28.77\,\text{eV} \cdot \sqrt{\frac{Z}{M}\rho\left[\text{g cm}^{-3}\right]} \tag{2.31}$$

where Z is the atomic number of the buffer gas, M its molar mass and ρ the density of the gas which is correlated with its pressure.

The scanning of higher axion mass regions by using a buffer gas was done in CAST Phase II. Special systems for metering the amount of gas (and therefore the achieved pressure) injected into the magnet bores were therefore installed at CAST. Systems to prevent thermoacoustic oscillations inside the gas-filled bores had to be implemented as well as additional windows inside the magnet for sealing the gas-filled volume of the still evacuated volumes. First ^{4}He was used as buffer gas up to a pressure of 16.4 mbar which corresponds to axion masses up to 0.39 eV [32]. Higher axion masses cannot be reached with CAST and ^{4}He as buffer gas. This is due to the fact that the magnet bores are at a temperature of ~ 1.8 K which would lead the ^{4}He gas to condensate in the bores at higher pressures [6]. Therefore, ^{3}He was used as buffer gas to look for even higher axion masses. As ^{3}He is very expensive special systems had to be build to retain the gas in case of a magnet quench instead of simply blowing it out to prevent the windows from bursting. With ^{3}He, CAST is sensitive for axion masses up to ~ 1.2 eV. The upper limits provided by CAST (Phase I and Phase II) are shown in figure 2.10.

2.2.2 X-ray detectors used at CAST

As the experimental parameters of CAST are mainly fixed by its magnet's properties, the performance of the x-ray detectors mounted at sunrise and sunset side of the CAST magnet play an important role in determining the sensitivity of CAST. The coupling constant $g_{a\gamma}$ to which CAST could detect axions is proportional to [33]

$$g_{a\gamma} \propto \frac{b^{1/8}}{t^{1/8}\epsilon^{1/4}} \tag{2.32}$$

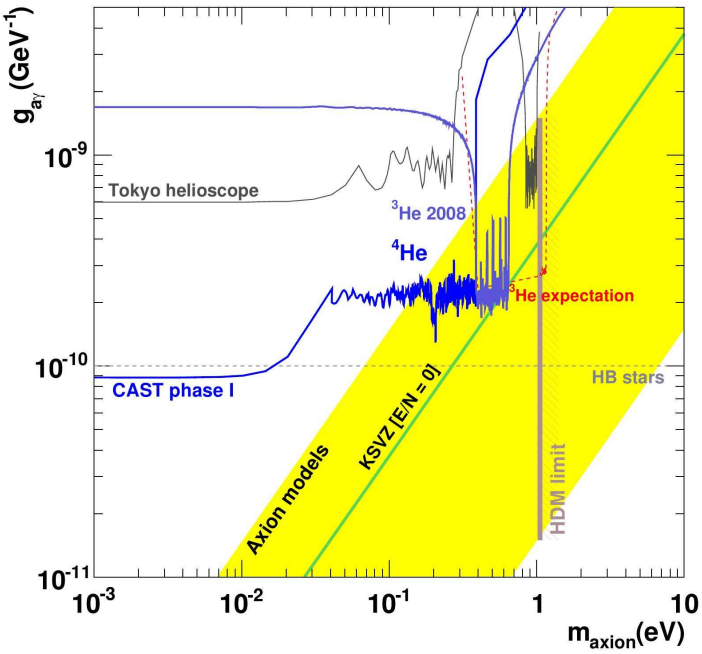

Figure 2.10: Axion exclusion plot, CAST has set the most stringent limits in the shown mass range. Results of CAST Phase I are plotted in black, results of CAST Phase II (^{4}He) are shown in blue. Prospects for CAST Phase II with ^{3}He are drawn in red, early results in violet. The yellow band represents theoretical favored axion models while astrophysical and cosmological constraints are indicated by lines (HDM limit and HB stars). Plot extracted from [10].

where b is the background rate of the detectors, t the total exposure time and ϵ the detector efficiency including losses caused by the windows inside the magnet. An important contribute to the good results of CAST is the detector performance with respect to low background rates and high efficiencies.

During its operation three types of x-ray detectors were used in the CAST experiment. The sunrise side of the magnet was all the time equipped with a Micromegas detector and a pnCCD detector which is combined with an x-ray mirror telescope (see figure 2.11). The x-ray telescope enhances the sensitivity of the detector placed behind it by focusing photons coming from the bore on a 9 mm^2 spot in the focal plane where the pnCCD is mounted.

Until 2007 the sunset side was covered by a Time Projection Chamber (TPC) which used anode wires as gas amplification stage and a pad-based readout in addition to readout of the wires. In 2007 the chamber was replaced by two MicroBulk Micromegas detectors as those detectors had shown on the sunrise side very good performance with respect of background rates and efficiency. In figure 2.12 CAST MicroBulk Micromegas are shown.

2.2.3 Shielding of the CAST detectors

To reduce the background rates observed with the x-ray detectors the TPC and the Micromegas detectors are equipped with a special shielding which was developed involving detailed measurements of background sources in the experimental area and simulations [35]. The shielding consists from inside to outside of:

- 5 mm copper as Faraday cage

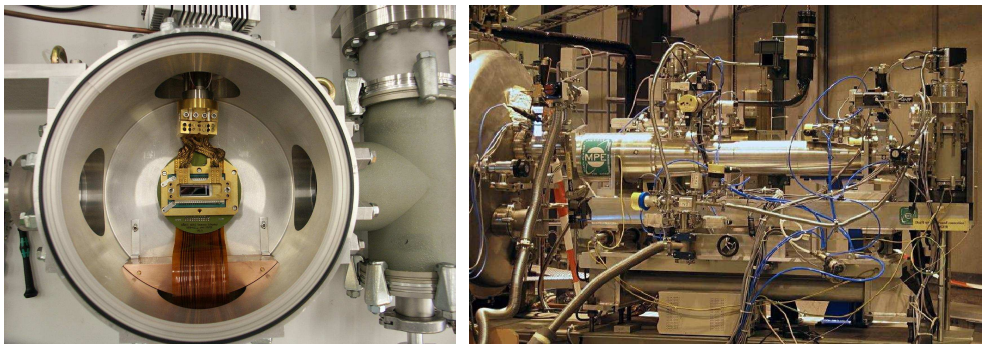

(a) (b)

Figure 2.11: Pictures showing the pnCCD used at CAST inside its vacuum vessel (a) and the x-ray telescope (b) it is mounted on. Taken from [6] and [10] respectively.

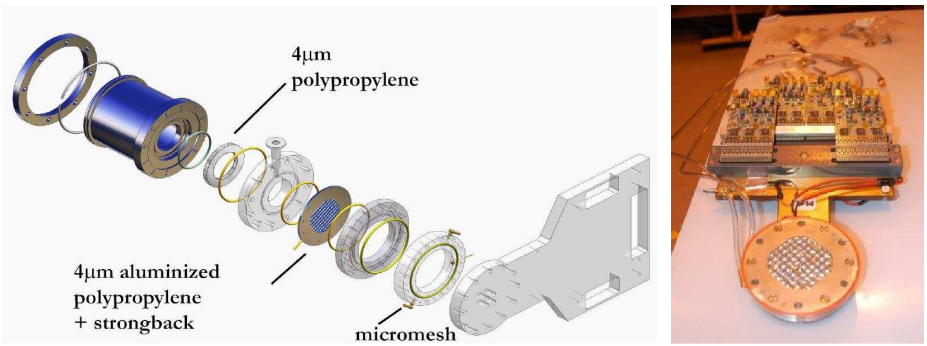

(a) (b)

Figure 2.12: Pictures of MicroBulk Micromegas used in CAST: Blow up drawing of a CAST MicroBulk Micromegas (a) and picture of a CAST MicroBulk Micromegas (b). Taken from [6] and [34] respectively.

- 2.5 cm roman lead to catch low energy particles
- 1 mm cadmium sheet to catch thermal neutrons
- $\sim$ 20 cm polyethylene blocks to moderate thermal neutrons
- PVC bag flushed with pure nitrogen to keep the volume around the detector free from radioactive radon
- Scintillators to veto cosmic ray events

In figure 2.13 a schematic cut through this shielding is shown.

For the Micromegas detectors the copper box surrounding the detector itself is flushed with nitrogen instead of flushing a bag containing the whole detector including the shielding. Also for the pnCCD detector additional shieldings were installed, lead shielding inside and outside its vacuum vessel and a Faraday cage made of copper inside the vessel.

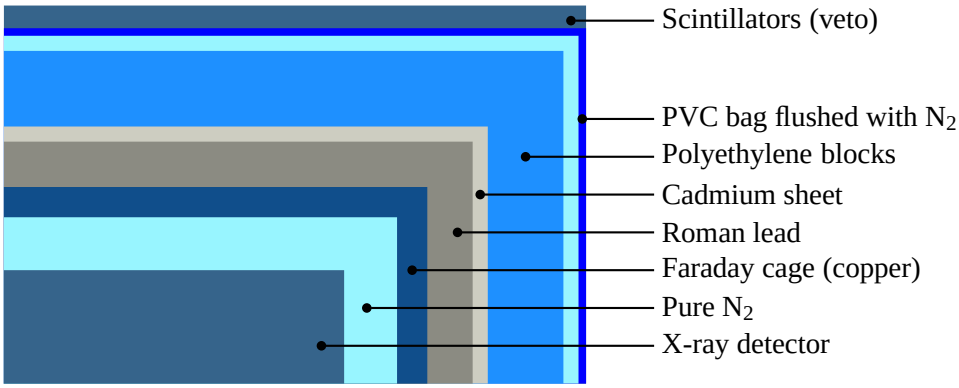

Figure 2.13: Sketch illustrating the shielding of the CAST detectors (not to scale).

Chapter 3

Gaseous Detectors

This chapter will describe the basic processes taking place in gaseous detectors. Starting with the separation of charges (electrons and ions) in a gaseous medium through ionization by charged particles traversing or (x-ray) photons being absorbed in the gas. The transport of the electrons to the readout plane in an electric field will be explained regarding the phenomena of drift and diffusion. Before arriving at the readout the electrons enter the strong electric fields where gas amplification (multiplication of incoming electrons) happens so that the charge finally ending at the readout is large enough to be detected. Also a short remark on the creation of the signal detected will be given.

As for the measurements done in this thesis often a ^{55}Fe source was used some remarks on the x-ray lines emitted by such a radioactive source will be given along with a short summary of what happens when the emitted x-ray photons are absorbed in a gas.

3.1 Ionization and Energy loss

Particles traversing or being stopped (respectively absorbed in case of photons) in the gas of a gaseous detector leave an ionization trace. In encounters with gas atoms (respectively gas molecules) they loose energy which is transferred to the gas atoms or their shell electrons. The energy transfer is mediated by the electromagnetic force as other forces (strong or weak) do not play a dominant role on the typical distance scale of these encounters. The energy transfer leads to ionization or excitation of the gas atoms. If one separates the charges (electrons and gas ions) created through ionization by applying an electric field one can detect the electrons on a readout plane and can therefore 'see' the particles trace in the detector. This information may be used to reconstruct the particle itself respectively its trajectory.

Of course, the x-ray detector built in this thesis is intended to detect x-ray photons. Therefore, along with interactions of charged particles with matter also the interactions of photons with matter will be explained. As the ionization processes for charged particles and photons are completely different they will be considered separately. Because the ionization by charged particles is needed to understand the complete chain from the x-ray photon interaction with the gas to the observed ionization trace, beginning with the interaction of charged particles is most reasonable.

3.1.1 Charged Particles

For a charged particle traversing a gas, encounters with the gas atoms will occur. These encounters occur completely randomly. The mean free path λ is the distance a charged particle will travel in mean between two encounters. It can be calculated from the electron density n_e in the gas and the ionization cross section σ_I as

$$\lambda = \frac{1}{\sigma_I n_e}. \tag{3.1}$$

For a thin gas the number of encounters on a length L is distributed according to the Poisson distribution with mean L/λ. Of course σ_I and so λ depends on the charged particles charge, mass and energy.

When encounters of a charged particle (e.g. a muon $\mu^\pm$) with a gas atom A happen, different mechanisms lead to ionization. The gas atom may get directly ionized, resulting in one or more free electrons:

$$\mu^\pm A \rightarrow \mu^\pm A^+ e^-, \mu^\pm A^{++} e^- e^-, \ldots \tag{3.2}$$

This is called primary ionization. It may also happen that the gas atom is not ionized but excited

$$\mu^\pm A \rightarrow \mu^\pm A^*. \tag{3.3}$$

If the detector gas is not pure but a mixture containing gas atoms B which have an ionization energy below the energy of the excitation state of A, B can get ionized by collisions with A^*

$$A^* B \rightarrow A B^+ e^- \tag{3.4}$$

which is called Penning effect. The Penning effect lowers the mean energy needed to ionize atoms in a gas mixture. If electrons freed by primary ionization got enough energy to ionize gas atoms by themselves this will also happen:

$$e^- A \rightarrow e^- A^+ e^-, e^- A^{++} e^- e^-, \ldots \tag{3.5}$$

The latter ionization processes are called secondary ionization, most ionization on particles trace results from secondary ionization. Electrons receiving large energies so that they create ionization traces themselves are called δ-electrons, they are emitted preferentially perpendicular to the incident particle's track.

The maximum kinetic energy transferred from the charged particle to an electron of a gas atom is given by [36]

$$T_{\max} = \frac{2 m_e c^2 \beta^2 \gamma^2}{1 + 2\gamma m_e/m + (m_e/m)^2} \tag{3.6}$$

where m_e is the electron mass, m the mass of the charged particle, $\beta = v/c$ its velocity in terms of the speed of light and γ the charged particles Lorentz factor. In case of particles heavier than electrons ($m > m_e$) which is true for all charged particles except for electrons, equation 3.6 becomes

$$T_{\max} = \frac{m^2 \beta^2 \gamma^2}{\gamma m + m^2/2m_e} = \frac{p^2}{E + (mc)^2/2m_e} \tag{3.7}$$

with $E = \gamma m c^2$ the incident particles energy and $p = \beta\gamma mc$ its momentum. The mean energy loss per length for heavy particles can be described with the formula of Bethe and Bloch [37]

$$-\left\langle \frac{\mathrm{d}E}{\mathrm{d}x} \right\rangle = 4\pi N_A r_e^2 m_e c^2 \frac{Z}{A} \rho \frac{1}{\beta^2} z^2 \left(\frac{1}{2} \ln \frac{2 m_e c^2 \beta^2 \gamma^2 T_{\max}}{I^2} - \beta^2 - \frac{\delta(\beta)}{2} \right) \tag{3.8}$$

N_A	Avogadro's number $N_A = 6.022 \times 10^{-23}\,\mathrm{mol}^{-1}$
r_e	Classical electron radius $r_e = \frac{e^2}{4\pi\epsilon_0 m_e c^2} = 2.82\,\mathrm{fm}$
m_e	Electron mass $m_e = 511\,{}^{\mathrm{keV}}/_{c^2}$
c	Speed of light $c = 299\,792\,458\,{}^{\mathrm{m}}/_{\mathrm{s}}$
Z	Atomic number of absorber material

A Atomic mass of absorber material
ρ Density of absorber material
I Mean excitation energy, can be approximated by $I = 16 \cdot Z^{0.9}\text{eV}$ for $Z > 1$ [36]
$\delta(\beta)$ density correction term

which is valid for $0.1 \lesssim \beta\gamma \lesssim 1000$. Often, not the energy loss per length dx is given but the energy loss per surface mass density d$X = \rho$dx

$$-\left\langle \frac{\mathrm{d}E}{\mathrm{d}X} \right\rangle = -\frac{1}{\rho}\left\langle \frac{\mathrm{d}E}{\mathrm{d}x} \right\rangle \tag{3.9}$$

which is almost independent of the absorber material. In figure 3.1 the energy loss per surface mass density (also known as stopping power) is plotted for muons in copper in dependence of their $\beta\gamma$. Particles with low $\beta\gamma$, slow particles (velocities in the regime of or slower than atomic electrons) are deflected in the electric field of the nuclei and loose thereby energy or even by interactions with the nuclei. For $\beta\gamma \gtrsim 0.1$ the energy loss decreases with $1/\beta^2$ until it reaches a minimum at $\beta\gamma \approx 4$.

$$-\left\langle \frac{\mathrm{d}E}{\mathrm{d}X} \right\rangle\Bigg|_{\beta\gamma\approx 4} \approx 1.5\,\text{MeV}/(\text{g}/\text{cm}^2) \tag{3.10}$$

Relativistic particles with $\beta\gamma \gtrsim 4$ are therefore called minimum ionizing particles (MIPS). Behind the minimum the energy loss rises again logarithmically with $\beta\gamma$. This logarithmic rise originates mostly from large energy transfers to a few electrons. The density correction $\delta(\beta)$ in equation 3.8 reduces the energy loss for highly relativistic particles as their transverse electric field is screened by the charge density of atomic electrons [36]. This correction is important for dense materials, for gases it can be neglected. For particles with $\beta\gamma \gtrsim 1000$ radiative losses like bremsstrahlung dominate, as equation 3.8 does only include energy losses due to ionization and excitation it is not valid anymore. As for a fixed energy (or momentum) equation 3.8 becomes a function of the incident particle's mass. Therefore, one can use the energy loss per length for particle identification in certain energy or momentum ranges. For thin absorbers the total energy deposited is distributed according to a Landau distribution resulting in a very long tail and large fluctuations. Therefore, the mean of the distribution does not fit with its most probable value. For thick absorbers the distribution of the deposited energy becomes Gaussian according to the central limit theorem.

As already mentioned equation 3.8 does only describe heavy charged particles, electrons have to be treated differently as they are identical with the target electrons which energy is transferred to. Also for electrons the emission of bremsstrahlung happens at lower energies due to their low mass. They suffer much more multiple scattering. The maximum transferable energy for electrons with energy E in one encounter with gas atoms is

$$T_{\max} = E - m_e c^2 \tag{3.11}$$

and their energy loss resulting from ionization and excitation can be calculated to [36]

$$-\left\langle \frac{\mathrm{d}E}{\mathrm{d}x} \right\rangle = 4\pi N_A r_e^2 m_e c^2 \frac{Z}{A}\rho\frac{1}{\beta^2}z^2\left(\ln\frac{m_e c^2\beta^2\gamma^2\sqrt{\gamma-1}}{\sqrt{2}I} + \frac{1-\beta^2}{2} - \frac{2\gamma-1}{2\gamma^2}\ln 2 + \frac{1}{16}\left(\frac{\gamma-1}{\gamma}\right)^2\right) \tag{3.12}$$

including kinematics of electron-electron collisions and screening effects.

The effective range R of electrons (distance between entering and stopping point) in a medium with density ρ can be calculated from the empirical relation given in [38]

$$R(E) = \frac{AE}{\rho}\left(1 - \frac{B}{1+CE}\right) \tag{3.13}$$

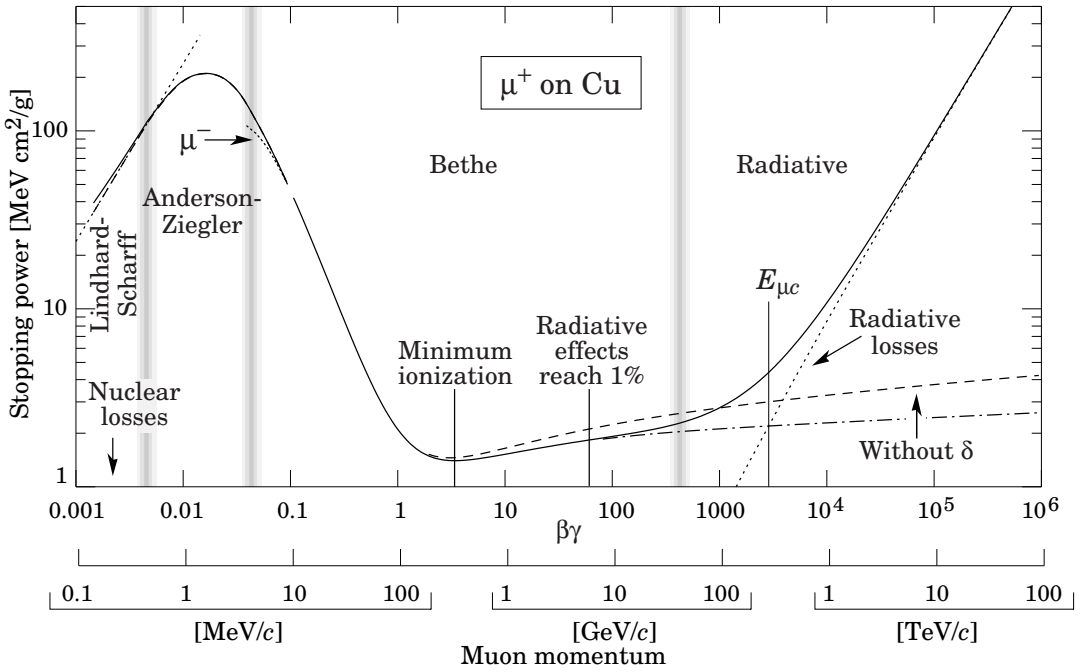

Figure 3.1: Stopping power for muons in copper, taken from [37]

with $A = 5.37 \times 10^{-4}\,\mathrm{g\,cm^{-2}\,keV^{-1}}$, $B = 0.9815$ and $C = 3.123 \times 10^{-3}\,\mathrm{keV^{-1}}$.

3.1.2 Photons

For photons the mechanisms of ionization are quite different to the ones for charged particles. They interact with medium, thereby charged particles are produced. In a gaseous x-ray detector, the x-ray photons are detected indirectly by detecting the charged particles they produced. In the interactions the photons are either absorbed or scattered in a relatively large angle. These interactions happen randomly making it impossible to define a range for photons in a medium. But as the absorption and scattering are statistical processes one can calculate how much a photon beam of initial intensity I_0 is attenuated after a distance x in a medium

$$I(x) = I_0 e^{-\mu x} \tag{3.14}$$

with μ the attenuation coefficient for the medium. μ can be calculated from the cross sections σ_i for the different interactions for photons

$$\mu = \rho \frac{N_A}{A} \sum_i \sigma_i. \tag{3.15}$$

Of course μ is highly dependent on the photon energy as the cross sections are. The charges (mainly electrons) produced by the interactions of the photons with the material will after the production loose energy through ionization until they get stopped. By this they create an ionization trace which can be detected.

For detector purposes there are only three interactions of photons relevant, the photoelectric effect, Compton scattering and pair production. Other processes like e.g. interactions with photons with the nuclei have very low cross sections and might be of interest for study of fundamental physics but can be neglected for the application of a detector.

Photoelectric effect

A photon can transfer its whole energy on an atomic electron, this only possible for atomic electrons as the nucleus is needed as recoil partner to conserve energy and momentum. Due to the energy transfer the electron is liberated.

$$\gamma A \rightarrow A^{+} e^{-} \tag{3.16}$$

As this interaction is mediated through the electromagnetic force its cross section is dominated by the interaction with electrons on the deepest atomic shell because of the short distance to the recoil partner and low screening by the atomic shells allowing to transfer a higher recoil momentum. Of course, the initial photon has to have at minimum the ionization energy needed to liberate an electron in the atom. The cross section for the photoelectric effect regarding only electrons on the deepest shell (K-shell) and assuming not to be at absorption edges of the atom is given by [36]

$$\sigma_{\mathrm{pe}}^{\mathrm{K}} = \sqrt{32}\left(\frac{m_e c^2}{E_\gamma}\right)^{3.5} \alpha^4 Z^5 \sigma_{\mathrm{Th}} \tag{3.17}$$

using the non-relativistic Born approximation, α is the finestructure constant, E_γ the photon energy and $\sigma_{\mathrm{Th}} = \frac{8}{3}\pi r_e^2$ the Thomson cross section for elastic photon electron scattering. It is obvious that the photoelectric effect is relevant only at low photon energies ($E_\gamma \lesssim 5\,\mathrm{MeV}$) and that it dominates especially for materials with high atomic numbers. Of course, the cross section is enhanced for photon energies near to the absorption lines of an atom.

When an electron of an inner shell (e.g. the K-shell) is kicked out by the photoelectric effect, an electron from a higher shell will fill this gap. The energy difference can be emitted as an x-ray photon of characteristic energy. But it might also happen that the energy difference is transferred to an electron in the same atom. If the transferred energy is larger than the energy necessary to ionize this electron it will be liberated. The latter process is called Auger effect and an electron emitted through this effect is called Auger electron. For one initial photon, several Auger electrons may be emitted in addition to the photoelectron liberated in the first step.

The emission angle of the photoelectron is not independent of the initial photons direction. For the differential cross section one obtains [39]

$$\frac{\mathrm{d}\sigma_{\mathrm{pe}}^{\mathrm{K}}}{\mathrm{d}\Omega} \propto \frac{\sin^2\theta \cos^2\phi}{(1-\beta\cos\theta)^4} \tag{3.18}$$

where θ is the angle between the initial photons direction and the direction of the emitted photoelectron (see figure 3.2a), ϕ is the angle between the emitted photoelectron and the photon's polarization (see figure 3.2b) and β is the velocity of the photoelectron divided by the speed of light. One sees that an almost perpendicular emission of the photoelectron is preferred and from its direction also polarization of the photon can be obtained. In figure 3.3 the differential photoelectric cross section is drawn as function of θ for a photoelectron energy of roughly 5.9 keV ($\beta = 0.15$).

Compton scattering

A photon can be scattered at quasi-free atomic electrons (binding energy is neglected), resulting in energy transferred to the electron and the photon being deflected. Both, electrons and photon are considered free. The cross section for Compton scattering on single electrons is independent of the atomic number of the material. Only for the atomic cross section the atomic number plays a role as it determines

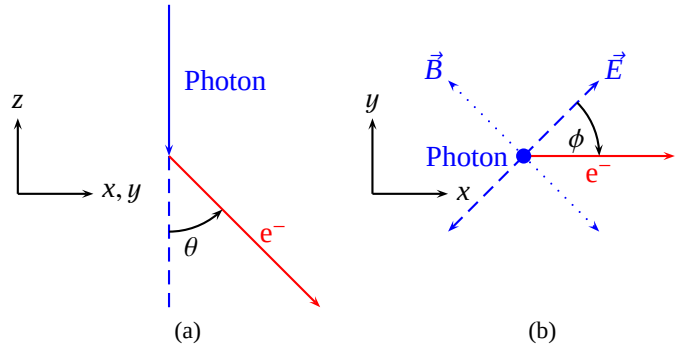

Figure 3.2: Drawings illustrating the angle definitions for the photoelectric effect: θ is the angle between the initial photons direction and the emitted photoelectron (a) and ϕ is the angle between the photoelectron and the photon's polarization (b). The photon's polarization is given by its electric field vector $\vec{E}$. In (b) the photon is entering the x, y plane.

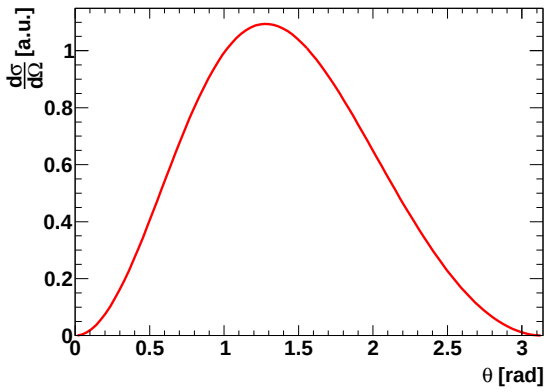

Figure 3.3: Differential photoelectric cross section (in arbitrary units) as function of angle θ. A value of 0.15 is assumed for β which corresponds to a photoelectron energy of roughly 5.9 keV.

the number of electrons which are available for the photon to scatter off one atom. For high energies the cross section's dependency on the energy can be approximated [36]

$$\sigma_{\mathrm{cs}} \propto \frac{\ln E_\gamma}{E_\gamma} \tag{3.19}$$

revealing that its importance decreases for very high photon energies.

The photon's energy E'_γ after scattering depends on its initial energy E_γ and the scattering angle Θ

$$\frac{E'_\gamma}{E_\gamma} = \frac{1}{1 + \frac{E_\gamma}{m_e c^2}(1 - \cos\Theta)} \tag{3.20}$$

and can be calculated from fourmomentum conservation. The maximum scattering angle ($\Theta = \pi$) is called backscattering. For backscattering the energy transferred to the electron becomes maximal. As the electron is expected to be at rest before the scattering, its direction (angle φ) after scattering with

respect to the initial photon direction is given by

$$\cot\varphi = \left(1 + \frac{E_\gamma}{m_e c^2}\right) \tan\frac{\Theta}{2}. \tag{3.21}$$

The energy transferred to the scattered electron is $E_\gamma - E'_\gamma$.

Pair production

A photon can convert into an electron positron pair,

$$\gamma P \rightarrow P e^- e^+ \tag{3.22}$$

but only if a charged particle P is present to absorb the recoil which is needed to assure conservation of energy and momentum. The creation of electron positron pairs might therefore happen in the electric field of a nucleus but also in the electric field of an electron although the latter is quite unlikely. Of course the photon has to have minimum energy to make pair production possible. This threshold energy can be calculated from four-momentum conservation and one gets

$$E_\gamma \geq 2 m_e c^2 + 2\frac{m_e^2}{m_{\text{recoil}}} c^2 \tag{3.23}$$

where m_{recoil} is the mass of the particle absorbing the recoil. For nucleons ($m_{\text{recoil}} = m_{\text{nucleus}} >> m_e$) the threshold energy becomes

$$E_\gamma \geq 2 m_e c^2 \approx 1\,\text{MeV}. \tag{3.24}$$

For low photon energies, pair production can only occur if the photon gets close to the nucleus and 'sees' it naked without screening through the atomic electrons. In this case the cross section can be given as [36]

$$\sigma_{\text{pair}} = 4\alpha r_e^2 Z^2 \left(\frac{7}{9}\ln 2\frac{E_\gamma}{m_e c^2} - \frac{109}{54}\right) \tag{3.25}$$

and for complete screening of the nucleus

$$\sigma_{\text{pair}} = 4\alpha r_e^2 Z^2 \left(\frac{7}{9}\ln\frac{183}{Z^{1/3}} - \frac{1}{54}\right) \tag{3.26}$$

and therefore for high photon energies, the cross section becomes energy independent. Pair production is dominant for high photon energies in combination with materials with high atomic number.

Total cross section

The total cross section for photon interactions with the absorber material are calculated from the before mentioned cross sections for the single processes. The total photon cross sections in dependence on the photon energy are shown in figure 3.4 for carbon ($Z = 6$) and lead ($Z = 84$). The different contributions are also indicated in the plots. Clearly visible are the enhancements of the photoelectric cross section originating from absorption lines of the target material.

For photons in the low x-ray regime $E_\gamma \leq 10\,\text{keV}$ only the photoelectric effect needs to be taken into account as other processes in this energy range contribute less than 1% to the total cross section.

3.2 Number of Ionizations

When a particle looses the energy ΔE in a medium, the number of created ionizations created (number of freed electrons) n_I can be calculated from the mean ionization energy w

$$n_I = \frac{\Delta E}{w} \tag{3.27}$$

of course w is larger than the ionization energy I in the medium. This is because also electrons from deep atomic shells are ionized and also not all lost energy leads to ionization but also to excitation which does not generally contribute to ionization.

For particles loosing their total energy E (by being stopped or absorbed) the number of ionizations would be expected to fluctuate according to Poisson distribution, so

$$\sigma_I^2 = n_I \tag{3.28}$$

in case of the particular ionization processes being independent. But as these are not independent from each other, the width of the distribution is reduced by a factor F called Fano factor

$$\sigma_I^2 = F n_I \tag{3.29}$$

which has a value of ~ 0.25 for noble gases but can become quite small (~ 0.05) for certain gas mixtures with small amounts ($\sim 1\%$) of quencher gases.

3.3 Drift and Diffusion

As the produced ionization trace consists of electrons and ions with opposite charge one has to separate these. Else electrons and ions would recombine emitting photons. Separation of electrons and ions is achieved by applying an electric field, electrons will move in one direction while ions move in the opposite direction. The movement of charged particles in an electric field is called drift. For the drift of a particle with charge e and mass m in presence of an electric field $\vec{E}$ and a magnetic field $\vec{B}$ one can write an equation of motion

$$m\frac{\mathrm{d}\vec{v}(t)}{\mathrm{d}t} = e\vec{E} + e\left[\vec{v}(t) \times \vec{B}\right] - K\vec{v}(t) \tag{3.30}$$

where $\vec{v}(t)$ is the particles velocity and $-K\vec{v}(t)$ acts as a frictional force due to collisions of the drifting particle with the gas atoms. Of course this equation of motion is only a macroscopic model but has been found to describe drift for large time scales to very good approximation [38]. The ratio

$$\tau = \frac{m}{K} \tag{3.31}$$

defines a characteristic timescale so that for $t >> \tau$ one can assume a steady state. As for a steady state $\vec{v}(t)$ becomes time independent, equation 3.30 is reduced from an inhomogeneous linear differential equation to a linear equation

$$\frac{1}{\tau}\vec{v} - \frac{e}{m}\left[\vec{v} \times \vec{B}\right] = \frac{e}{m}\vec{E}. \tag{3.32}$$

This equation is solved by the Langevin formula

$$\vec{v} = \frac{e}{m}\tau|\vec{E}|\frac{1}{1+\omega^2\tau^2}\left(\frac{\vec{E}}{|\vec{E}|} + \omega\tau\left[\frac{\vec{E}}{|\vec{E}|}\times\frac{\vec{B}}{|\vec{B}|}\right] + \omega^2\tau^2\left(\frac{\vec{E}}{|\vec{E}|}\cdot\frac{\vec{B}}{|\vec{B}|}\right)\frac{\vec{B}}{|\vec{B}|}\right) \tag{3.33}$$

with $\omega = \frac{e}{m}|\vec{B}|$ the cyclotron frequency and assuming τ to be independent of the particles energy.

For vanishing magnetic fields ($\omega\tau = 0$) particles drift in the direction of the electric field and their velocity becomes

$$\vec{v} = \frac{e}{m}\tau\vec{E} = \mu\vec{E} \tag{3.34}$$

where μ is called the mobility of the particle. Of course the mobility for ions is much lower than the mobility for electrons as the mass of ions is much larger than the electron mass. Electron and ion mobility also differ in sign as the mobility already defines the direction of drift.

For a magnetic field in the drift region the drift velocity can be expressed in terms of the drift velocity without a magnetic field

$$\left|\vec{v}(\vec{B})\right|^2 = \left|\vec{v}(\vec{B}=\vec{0})\right|^2 \frac{1+\omega^2\tau^2\cos^2\phi}{1+\omega^2\tau^2} \tag{3.35}$$

with ϕ the angle between $\vec{E}$ and $\vec{B}$. For $\vec{E} \parallel \vec{B}$ the drift velocity as well as the drift direction remain unchanged. In case of $\vec{E} \perp \vec{B}$ the drift direction is no longer parallel to the electric field but has an angle

$$\theta = \arctan(-\omega\tau) \tag{3.36}$$

with respect to the direction of the electric field. This angle is called the Lorentz angle.

Comparing the results of this macroscopic approach with a microscopic model which takes into account the random collisions between the drifting particle and the gas atoms [38] one finds that in case of $\vec{B} = \vec{0}$ the characteristic timescale τ of the macroscopic approach can be identified with the mean time between two collisions of the drifting particle and gas atoms. Of course, τ is related to the cross section for elastic collisions and the number density of the gas atoms.

The cross section depends on the energy of the drifting particle and therefore τ too. Equation 3.33 can be used as approximation, especially for the drift direction and the influence of a magnetic field. However, the cross sections dependence on the energy can also be taken as a dependence on the electric field as this determines the energy gain between the collisions. This results in the mobility μ depending on the electric field. Therefore, simulations have to be used for getting the mobility of a gas (mixture) at a certain value for the electric drift field. The calculation of the cross section needs quantum mechanical treatment as measurements counterfeit classical expectations e.g. the Ramsauer effect.

The collisions with gas atoms lead to the drifting particles being scattered randomly. Therefore, a particle cloud starting point-like will become Gaussian distributed in all directions so that its density distribution after a time t can be given as

$$n(\vec{x}) = \left(\frac{1}{\sqrt{4\pi Dt}}\right)^3 \exp\left(\frac{-|\vec{x}-\vec{v}T|^2}{4Dt}\right) \tag{3.37}$$

with D the diffusion constant and assuming the particle cloud starting at the origin. The mean squared deviation for this Gaussian distribution is given by $\sigma^2 = 2Dt$ and is equal for all directions. So the charge cloud widens with the time it is drifting. Using the microscopic model mentioned before one can

relate the diffusion constant with the mean particle energy ϵ and its mobility μ

$$D = \frac{2}{3}\frac{\epsilon\mu}{e}. \tag{3.38}$$

When the particles energy is only its thermal energy $\epsilon = \frac{3}{2}kT$ one arrives at the Nernst-Townsend or Einstein formula

$$\frac{D}{\mu} = \frac{kT}{e} \tag{3.39}$$

which defines a lower limit for the diffusion constant. Often the width of the density distribution after a drift distance L instead of the time t is needed or more applicable. By inserting $t = L/(\mu|\vec{E}|)$ one gets

$$\sigma^2 = 2Dt = \frac{2DL}{\mu|\vec{E}|} = \frac{4\epsilon L}{3e|\vec{E}|}. \tag{3.40}$$

Splitting the diffusion constant D in a diffusion constant D_T for the diffusion transverse to the drift direction and a diffusion constant D_L for diffusion in drift direction (longitudinal diffusion) one can define

$$D_\mathrm{t} = \sqrt{\frac{2D_\mathrm{T}}{\mu|\vec{E}|}} \tag{3.41}$$

$$D_\mathrm{l} = \sqrt{\frac{2D_\mathrm{L}}{\mu|\vec{E}|}} \tag{3.42}$$

so that the width of the density distribution is given by

$$\sigma = \sigma_\mathrm{t/l} = D_\mathrm{t/l}\sqrt{L}. \tag{3.43}$$

The transverse and longitudinal diffusion are not the same. This was first observed in experiments by Wagner et al. [40] in 1967. The reason for this electric anisotropy [38] is the energy dependence of the cross section for elastic collisions. Due to this the mobility is energy dependent which results in the particles in a drifting cloud having different mobilities depending on their position in the cloud. Therefore, equation 3.37 becomes

$$n(\vec{x}) = \left(\frac{1}{\sqrt{2\pi}D_\mathrm{t}^2 L}\right)^2 \left(\frac{1}{\sqrt{2\pi}D_\mathrm{l}^2 L}\right) \exp\left(\frac{-(x^2+y^2)}{2D_\mathrm{t}^2 L}\right) \exp\left(\frac{-(z-L)^2}{2D_\mathrm{l}^2 L}\right) \tag{3.44}$$

with L the drift distance. D_t and D_l are typically different but of same order of magnitude. When a magnetic field is present, the diffusion transverse to the direction of the magnetic field is reduced as the Lorentz force acts as a retarding force for particles with velocity components perpendicular to the magnetic field resulting in spiral trajectories around the drift field for $\vec{E} \parallel \vec{B}$.

Typically small diffusion constants are desirable for gaseous detectors as diffusion limits the spatial resolution. However, for the x-ray detector which is object to this thesis, large diffusion is wanted to diffuse the electrons created through ionization by the photoelectron so much that they can be separated, thus making possible to measure the incident photons energy by counting the number of electrons created through ionization.

3.4 Gas Amplification

After the charges created through ionization have been separated they drift to the ends of the detector, the ions towards the cathode and the electrons to the anode and readout plane. Of course, the electrons arriving at the readout plane cannot be detected since, they are too few to generate signals large enough to be detected with electronics. Therefore one needs to multiply the electrons creating signals large enough to be detected, for sufficiently high multiplication factors also detection of single electrons can become possible.

Multiplication of electrons will happen in strong electric fields, when the energy an electron gains from the acceleration by the electric field between two collisions becomes large enough for the electron ionizing a gas atom in an inelastic collision. If the electric field is strong enough each inelastic collision will produce a new electron ion pair. The produced electron will be accelerated too so that it will also ionize gas atoms in inelastic collisions. So, each new electron in the gas amplification region will create new electron ion pairs resulting in an avalanche. For ions gas amplification does not occur due to their high mass. Typical gains reached in a gas amplification stage reach from 10^3 to 10^5. For very high electric fields and therefore very high gains discharges become more and more likely to happen so that a stable operation of a gas amplification stage is only possible up to a certain gain depending on the type of gas amplification stage and of course on the rate of charged particles ionizing the detector gas.

To describe the gas amplification and the avalanches one can use the Townsend coefficient $\alpha(\epsilon)$ which depends of course on the electron energy ϵ and can be calculated from the number density of gas atoms n and the ionization cross section $\sigma_\mathrm{I}(\epsilon)$

$$\alpha(\epsilon) = n\sigma_\mathrm{I}(\epsilon) \tag{3.45}$$

which gives the mean number of ionizations per length. Of course many factors as e.g. gas pressure, temperature, recombination and the Penning effect enter into the Townsend coefficient [38, 41]. The Penning effect results in lower energies necessary for ionization and, therefore, increases the gas gain. For calculating the gain of a gas amplification stage it is more suitable to use $\alpha(|\vec{E}|)$ instead of $\alpha(\epsilon)$ but this transformation is non-trivial and one has to rely on simulations and measurements of $\alpha(|\vec{E}|)$ as the Townsend coefficient cannot be calculated analytically for the electric field strengths used in the gas amplification region.

The development of the number of electrons in an avalanche can be derived from the Townsend coefficient as the increase of electrons after a distance dx in the amplification region is given by

$$\mathrm{d}N = N(x)\alpha(|\vec{E}(x)|)\mathrm{d}x \tag{3.46}$$

where $N(x)$ denotes the number of electrons in the avalanche after a distance x. Therefore, $N(x = 0)$ is the number of electrons before they enter the amplification region. So the total number at the end of the amplification process is given by integrating dN from the starting point of the avalanche ($x = 0$) up to its endpoint ($x = \Delta x$)

$$N(\Delta x) = \int \mathrm{d}N = N(x = 0) \exp\left(\int_0^{\Delta x} \alpha(|\vec{E}(x)|)\mathrm{d}x\right) \tag{3.47}$$

which becomes

$$N(\Delta x) = N(x = 0) \exp\left(\alpha(|\vec{E}|)\right)\Delta x \tag{3.48}$$

for a constant electric field. The gas gain G is defined as the number of electrons at the end of the

avalanche divided by the initial number

$$G(\Delta x) = \frac{N(\Delta x)}{N(x=0)} = \exp\left(\alpha(|\vec{E}|)\right)\Delta x \tag{3.49}$$

and as a constant electric field in an amplification region is defined by the size of the amplification gap Δx and the applied potential difference ΔU

$$G(\Delta U) = \exp\left(\alpha\left(\frac{\Delta U}{\Delta x}\right)\frac{\Delta U}{|\vec{E}|}\right). \tag{3.50}$$

Taking into account that gas amplification will happen only for a potential difference greater than a certain threshold one can parameterize the gas gain as [41]

$$G(\Delta U) = A\exp\left(B\Delta U\right) \tag{3.51}$$

where the parameters A and B can obtained from gain measurements for different potential differences.

The development of the avalanche is of course a statistical process with large fluctuations. The stated gas gain is only the mean value for the gas amplification. It can be found that the distribution of gas amplification can be described by the Polya distribution [38, 42] in case of uniform or cylindrical electric fields in the amplification region. An applicable parametrization of the Polya distribution is given in [38]

$$P(N) = \frac{1}{\bar{N}}\frac{(\theta+1)^{\theta+1}}{\Gamma(\theta+1)}\left(\frac{N}{\bar{N}}\right)^{\theta}\exp\left(-(\theta+1)\frac{N}{\bar{N}}\right) \tag{3.52}$$

with $\bar{N}$ the mean of the distribution and θ related to the width σ of the distribution by

$$\sigma^2 = \frac{\bar{N}^2}{\theta+1}. \tag{3.53}$$

Inside the avalanche also photons in the UV regime are emitted due to excitation of gas atoms. The excitation can either be caused by collisions or recombination of electrons and ions. These UV photons can ionize gas atoms when they get absorbed again. If the re-absorption occurs inside the amplification region new avalanches displaced with respect to the original one will be started. If the re-absorption happens in the drift volume or this will lead to avalanches which are delayed and displaced. Even if the UV photons are not absorbed in the gas they could reach metal surfaces (e.g. electrodes) and kick out electrons by the photoelectric effect. To avoid such fake signals not originating from the ionization trace deposited in the detector, quencher gases are added to the gas of the detector which can absorb UV photons without getting ionized. Quencher gases are molecular gases (e.g. CO_2, CH_4 or iC_4H_{10}) which have absorption lines in the UV regime so that they have high cross sections for absorbing and, therefore, stopping the UV photons. As these molecular gases have vibrational states they can deexcite by emitting photons in the infrared regime or by transferring energy in collisions with other gas atoms.

3.5 Signal Development

To understand how the charges created in the gas amplification lead to signals on strips, pads or pixels of a readout structure the best way is to start with the very simple case of a single charge q and a single infinitely large electrode. The presence of the charge will induce a mirror charge $-q$ on the electrode which does not depend on the position of the charge. If the electrode is divided into several pads, the

charge q_n induced on pad n will depend on the position $\vec{x}$ of the charge q. However, summing over all pads will still give the total mirror charge induced

$$Q^{\text{ind}}_{\text{total}} = \sum_n q_n = -q. \tag{3.54}$$

When the charge moves ($\vec{x} \rightarrow \vec{x}(t)$) the charge q_n induced on a pad will change in time, a current $i_n(t)$ induced on the pad is the consequence. Of course, this current depends on the velocity of the charge

$$i_n(t) = -\frac{\mathrm{d}q_n(\vec{x}(t))}{\mathrm{d}t} = -\vec{\nabla} q_n(\vec{x}(t)) \cdot \underbrace{\frac{\mathrm{d}\vec{x}(t)}{\mathrm{d}t}}_{\text{velocity}}. \tag{3.55}$$

The total charge induced on a pad at the time T can be calculated by integrating the current on this pad

$$Q^{\text{ind}}_n(T) = \int_0^T i_n(t)\mathrm{d}t \tag{3.56}$$

assuming that at a time $T = T_{\text{end}}$ the charge q arrives on pad m the total charge on this pad is q while the integral for all other pads has to give zero. So, the charges induced on the pads will change until the charges movement stops.

In the situation of gas amplification above a readout many charges (electrons and ions) are produced. As these charges drift they induce currents on the readout pads, as electrons and ions are drifting in opposite directions the currents induced by electrons and by ions have the same sign although they have opposite charges. As electrons are moving much faster in the electric field than ions the signal they induce is very short ($\sim$ ns) but high until they arrive on the readout pads. So, the induced currents will stop when the ions drift is terminated.

To calculate the current induced on an electrode n (strip, pad or pixel) from the drifting charge q and its trajectory $\vec{x}(t)$ one can use Ramo's theorem [43]

$$i_n(t) = -q\vec{E}_n(\vec{x}(t)) \cdot \frac{\mathrm{d}\vec{x}(t)}{\mathrm{d}t} \tag{3.57}$$

with $\vec{E}_n(\vec{x})$ the weighting field of electrode n. The weighting field for an electrode can be obtained by calculating (or simulating) the electric field with the electrode of interest set to a potential of 1 V while all other electrodes are set to 0 V.

3.6 Spectrum of ^{55}Fe

^{55}Fe has a half life of 2.73 a and decays via electron capture to an excited state of ^{55}Mn. The ^{55}Mn will fall back to its ground state by emitting photons

$$^{55}\text{Fe} \rightarrow {}^{55}\text{Mn}^* \rightarrow {}^{55}\text{Mn} + \gamma \tag{3.58}$$

with energies of 5.899 keV (K_α line) or 6.490 keV (K_β line). To suppress the K_β line one can use a chromium foil which is put between the radioactive source and the detector. Chromium has a compton edge at 5.989 keV therefore the transmission for the K_α line is about 80% while it is only 15% for the K_β line when using a 10 µm thick foil [42]. By removing the K_β line one can enhance the 'measured' energy resolution of a detector in the case that the two lines could not be separated as so only one peak

at 5.899 keV appears instead of two overlapping peaks.

In pure Argon at atmospheric pressure the mean free path for the 5.899 keV photon is about 2.08 cm (2.7 cm for 6.490 keV photons) [41]. From figure 3.4 one can see that in this energy regime the photon absorption is dominated by the photoelectric effect. This is also true when quencher gases are added in fractions up to 20% [41].

When these photons are absorbed due to photoelectric effect, the emitted photoelectron comes with $\sim$ 11% probability from the L- or M-shell and carries therefore nearly the complete photon energy (photon energy minus binding energy of the electron). In the remaining $\sim$ 89% of the cases the electron is emitted from the K-shell and has an energy of 2.694 keV (K_α) or 3.286 keV (K_β) as the binding energy for electrons in the K-shell of Argon is approximately 3.2 keV. The remaining hole in the K-shell will of course be filled with an electron from the L- or M-shell. The energy emitted in this process can either be transferred to one or several Auger electrons (86.5% of the cases) or it can be emitted as a photon with energy between 2.957 keV and 3.190 keV depending on the shell from which the electron filling the hole originates. Probabilities and energies taken from [42].

The photoelectrons as well as the Auger electrons will loose energy through ionization and will be stopped within a short distance according to equation 3.13 (e.g. a 5.9 keV electron has a range of $\sim$ 630 µm in Ar/iC_4H_{10} 95/5). However, if instead of Auger electrons a photon is emitted, this might escape from the detector (or sensitive area) as it has a mean free path of $\sim$ 3.2 cm in Argon. These photons are also called escape photons. As the photons carry away some part of the energy of the incident photon when they leave the detector they lead to the appearance of new peaks in the spectrum, the escape peaks, at energies corresponding to the energies of photoelectrons emitted from the K-shell.

For Helium based mixtures the situation is different. As Helium has only a K-shell with low binding energies (24.5 eV) no escape photons can be emitted. Therefore, only the photopeak shows up resulting from the photoelectron carrying nearly the full energy of the incident photon. The ionization trace of the photoelectron in Helium based mixtures is quite long (several mm) due to the low density of the gas.

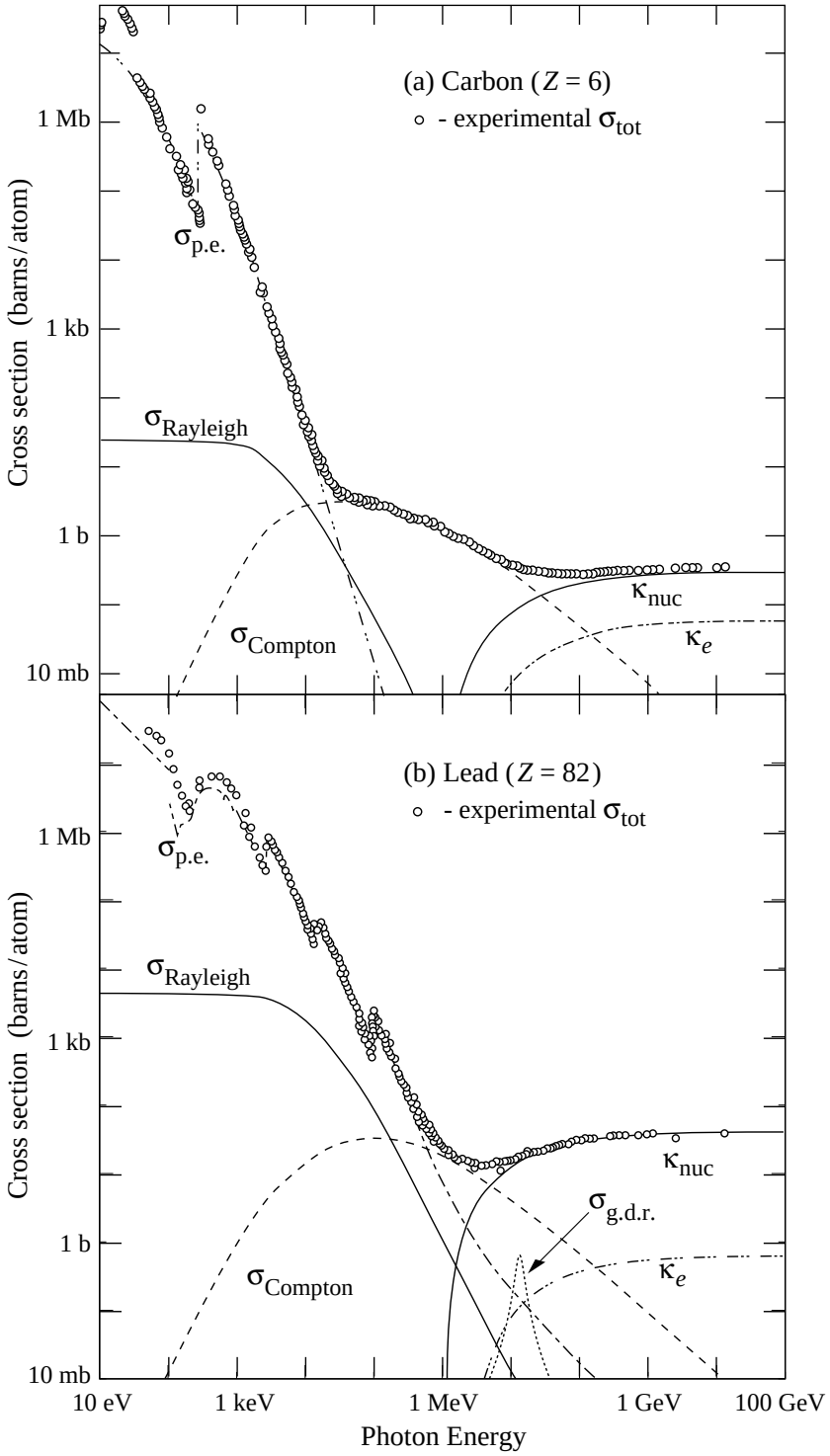

Figure 3.4: Cross section for photon interactions in carbon (top) and lead (bottom) as function of the photon energy, taken from [37]. Different contributions to total cross section are indicated: $sigma_{\text{p.e.}}$ denotes the photo-electric cross section, σ_{Compton} the cross section for Compton scattering, σ_{Rayleigh} the cross section for Rayleigh scattering, κ_{nuc} and κ_e the pair production cross sections in nuclear respectively electron field. $\sigma_{\text{g.d.r.}}$ is the cross section for photonuclear interactions.

Chapter 4

Micromegas Detectors

One kind of **M**icro**p**attern **g**aseous **d**etectors (MPGDs) are the **MicroMe**sh **Ga**soeous **S**tructures (Micromegas). Usually Micromegas are used with pad or strip based readouts. As the GridPix readout which is used for the detector constructed during this thesis is a combination of a pixelized readout chip (Timepix chip) and an integrated Micromegas produced with photolithographic postprocessing, the working principle of Micromegas will be introduced in this chapter. Also the MicroBulk-Micromegas will be shortly presented as the Micromegas detectors currently used at CAST are of this type. Last but not least remarks on the combination of Micromegas with pixelized readout will be given along with a description of how the integrated Micromegas of the GridPix are fabricated.

4.1 Micromegas principle

The Micromegas detectors were introduced in 1996 by Charpak and Giomataris [44, 45]. In Micromegas detectors the gas amplification structure is realized with a thin electroformed micromesh (a metallic grid, 3 μm thick with holes of 17 μm diameter and a pitch of 25 μm) which is stretched and glued onto a frame. The micromesh is then placed above a pad or strip based readout layer with small insulating spacers in between generating a gas amplification gap of about 100 μm. These spacers can be build directly on the readout plane with conventional lithographic procedures as used for standard printed circuit boards. By applying high voltage to the micromesh electric fields of $\sim 50\,^{\mathrm{kV}}/_{\mathrm{cm}}$ are reached inside the amplification gap so that gas amplification takes place. A sketch of a Micromegas detector is shown in figure 4.1.

One advantage of the Micromegas is that most of the ions produced during gas amplification do not flow back into the drift volume above the micromesh as they are captured on its top (if ratio between drift field and field in the amplification gap is tuned properly). Micromegas detectors have proven to be radiation hard, capable of high rates and very reliable. Also they are quite cheap and the construction of large area detectors is possible. Also very good spatial and time resolution (about 1 ns) can be achieved.

To improve the uniformity of the amplification gap the electroformed micromesh was replaced in [46] with a mesh created by chemical etching in combination with photolithographic techniques from a Kapton foil coated with copper on both sides. By this the pillars generating the amplification gap are already integrated in the mesh. With such a Micromegas an energy resolution of 12% FWHM (Full Width at Half Maximum) at an energy of 5.9 keV could be achieved along with good single electron detection at very high gas gains.

4.2 Bulk- and MicroBulk-Micromegas

In case of Bulk-Micromegas [47] a woven wire mesh is used instead of a micromesh. This is laminated onto the readout plane with a photoresistive film in between. By etching the photoresistive film with photolithographic methods it forms the pillars supporting the mesh and defining the amplification gap.

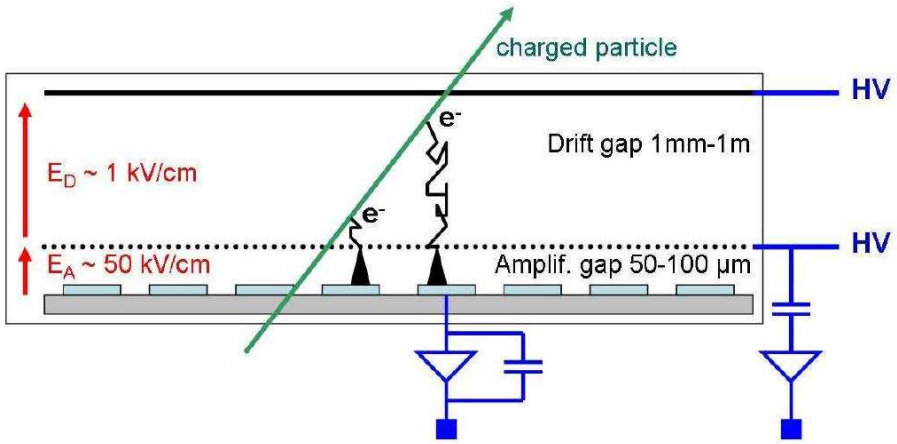

Figure 4.1: Sketch of a Micromegas detector, extracted from [41]

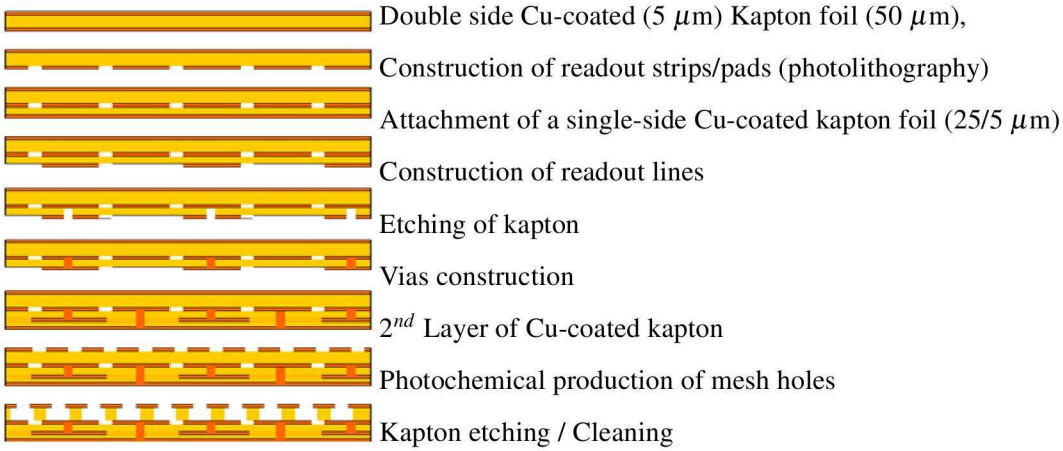

Figure 4.2: Manufacturing process of Micro-Bulk Micromegas, extracted from [48]

This procedure allows to build the Micromegas in one process and as one object. Of course this techniques simplifies the creation of large area detectors at low costs and allows to build curved Micromegas detectors with very low material budget if the readout plane is realized as a flexible board (e.g. made of Kapton foil).

For MicroBulk-Micromegas [48] the idea is to create the Micromegas not only as one object but also in one process respectively with one technique. MicroBulk-Micromegas already include the whole strip-based two dimensional readout scheme (except the readout electronics) as integrated part. The MicroBulk-Micromegas are fabricated as one object with photolithographic procedures from copper coated Kapton foils. Also, the strips for the readout and their connections to the readout electronics are manufactured in this process which is sketched in 4.2. The MicroBulk-Micromegas in the end consist mainly of Kapton and some copper. Their readout electronics are put outside the detector lowering the material budget of the detector itself.

MicroBulk-Micromegas show very good energy resolution (15% FWHM at 5.9 keV). As MicroBulk-Micromegas detectors proven to be of high radio-purity [49] and to reach very low background rates

[34] they are very attractive for experiments with low event rates. They are already used at CAST [33] and n-TOF [48, 50]. At CAST MicroBulk-Micromegas detectors could reach background rates of $10^{-6}\,\mathrm{cm}^{-2}\,\mathrm{keV}^{-1}\,\mathrm{s}^{-1}$ in the energy range of 2 to 7 keV.

4.3 Combination of Micromegas and pixelized readout

As the gas amplification structure of Micromegas regarding pitch and hole sizes of the micromesh is already in the regime of pixelized readouts one can benefit from combining a Micromegas gas amplification structure with a pixel chip (e.g. the Timepix chip which is already used in gaseous detector applications). Replacing the pad or strip based readout of standard Micromegas detectors with a pixel chip results in better spatial resolution as the dimensions of pixels ($\sim 50\,\mu\mathrm{m}$) are much smaller than those of strips or pads ($\sim 400\,\mu\mathrm{m}$ up to scale of mm). Of course, it also gets possible to separate and recognize initial electrons which were amplified in two neighboring mesh holes, if the mesh holes are correctly aligned with the pixels. Due to the better spatial resolution in combination with the ability to resolve single electrons a much higher sensitivity to the distribution of the electrons created through ionization in the detector can be achieved. Another advantage of a pixel chip as readout is that the whole electronics (preamplifier, discriminator and digitization) are integrated in the pixels instead of having to connect strips or pads with the corresponding electronics through (long) lines.

The intuitive approach to combine a Micromegas with a pixelized readout is to simply put a standard Micromegas onto a pixel chip [51]. In figure 4.3a an integral image of such a device illuminated with a ^{55}Fe source is shown. When putting a standard Micromegas onto a pixel chip small misalignment is nearly unavoidable which results in a Moiré pattern[1]. Also visible in figure 4.3a are the positions of the small cylindrical spacers defining the distance between mesh and pixel chip. They create dead pixels as they block some of them. To avoid this it would be desirable to place them between the pixels thus again requiring very precise alignment and reproducibility.

A very good way to achieve the very precise alignment between the Micromegas and the pixel chip is to integrate the gas amplification structure directly on the chip with means of photolithographic post-processing. The gas amplification stage build in such a procedure is called InGrid (Integrated Grid) [41, 52]. An image of a Timepix chip with an InGrid is shown in figure 4.3b. No Moiré pattern is visible but a very homogeneous efficiency.

As in all gas amplification structures discharges may happen (e.g. induced by alpha particles from decay of radioactive Radon) this also happens in Micromegas. However in case of Micromegas equipped with pad based readout protection devices like diodes can be used to protect the electronics. However, for the electronics in pixel chips this is not possible. So, already the first discharge may destroy the whole pixel chip or parts of it (some pixels or several columns). To avoid the destruction of the pixel chip in case of a discharge a resistive protection layer is needed which spreads the charge created in a discharge over a larger area on the chip. Such a protection layer can also be applied with photolithographic postprocessing. Materials already used as protection layers on Timepix chips are amorphous silicon and silicon nitride. Of course, a resistive protection layer also creates some drawbacks especially when the detector is operated at high rates. Then, the protection layer can be charged up, resulting in a lower effective potential difference between surface of the protection layer and grid or mesh of the gas amplification structure and, therefore, in a reduction of the gas gain [42].

[1] The Moiré pattern is an interference pattern which appears when two overlaying grids are tilted against each other with a small angle or if the grids have slightly different geometry

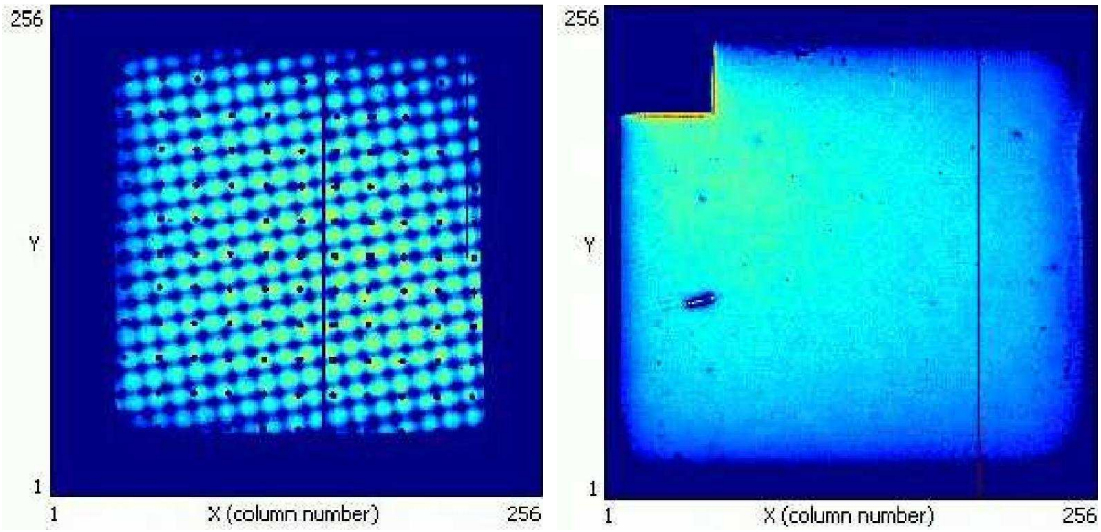

(a) (b)

Figure 4.3: Integral images of a Timepix chip equipped with a standard Micromegas (a) and of a Timepix equipped with an InGrid (b). Both illuminated with a ^{55}Fe source. In case of the standard Micromegas a Moiré pattern is visible as also dead areas created by the cylindrical spacers needed for the Micromegas. The top left corner of the InGrid was used to connect the grid with high voltage and is therefore inactive. Pictures extracted from [42].

4.3.1 Fabrication of an Integrated Grid

In the following the fabrication of an InGrid on top of a Timepix chip (more information on the Timepix chip can be found in chapter 5) will be described. The different fabrication steps to build the Micromegas-like gas amplification structure are described in [41] and sketched in figure 4.4. The enumeration of the steps listed below follows the enumeration in figure 4.4.

1. One starts the procedure with a bare Timepix chip with a passivation layer on top. The pixels (metal pads) appear as openings in the passivation layer.

2. The resistive protection layer consisting of silicon nitride is deposited on the Timepix. As this process step requires high temperatures (more than 300 °C) it is done in several substeps. The total thickness of the layer can be varied by the number of substeps. Typical thicknesses between 2 and 8 μm are used.

3. The negative photoresist (SU-8) is deposited by spin coating. From this layer later the structures supporting the grid will be created. Typically a thickness of 50 μm is deposited although 10 to 200 μm are possible with a precession of 10 to 20%. The thickness variation on one chip is in the order of 1%.

4. To form the structures supporting the grid a mask is placed on the photoresist and then the structure is exposed to ultraviolet light with a mask. The areas exposed will stay after development and cleaning of the photoresist. The structures created by this are the cylindrical pillars in the active area and walls or dikes at the sides. Typical pillar diameter is 30 μm. The pillars are of course placed between the pixels with pitches between 110 and 165 μm.

5. An aluminium layer is sputtered onto the SU-8 which will later form the grid (mesh for gas amplification). Typical a layer of 1 μm thickness is deposited.

6. To etch the grid holes a mask made of photoresist is created on top of the aluminium layer by photolithography.

7. The grid holes are etched with a solution of phosphoric acid and the photoresist mask is removed. The hole diameters can be varied between 10 μm and the value of the hole pitch with a precession of 1 to 8 μm with less than 1 μm deviation on one grid. A typical value for the hole diameter is 30 μm.

8. Development of the SU-8 which means to wash out the unexposed SU-8 in the interstitials with a special solution or cleaner. As sometimes residues of the SU-8 stay in the interstitials, these can be removed by cleaning in an oxygen plasma.

Of course the gas amplification structure obtained by this process is mechanically fragile and has to be treated with care. The first Timepixs with InGrid ontop were produced on single or few chip level at the University of Twente and the Nikhef in Amsterdam. Production on wafer level is now done in cooperation by the IZM at Berlin, the first Timepix wafer completely equipped with InGrids was delivered in August 2011.

With the photolithographic postprocessing also staggering of InGrids is possible, structures with two or three staggered grids were build [53]. Of course, these are even more fragile (already during production) than the single grid structures and also very sensitive to small misalignments in the production steps.

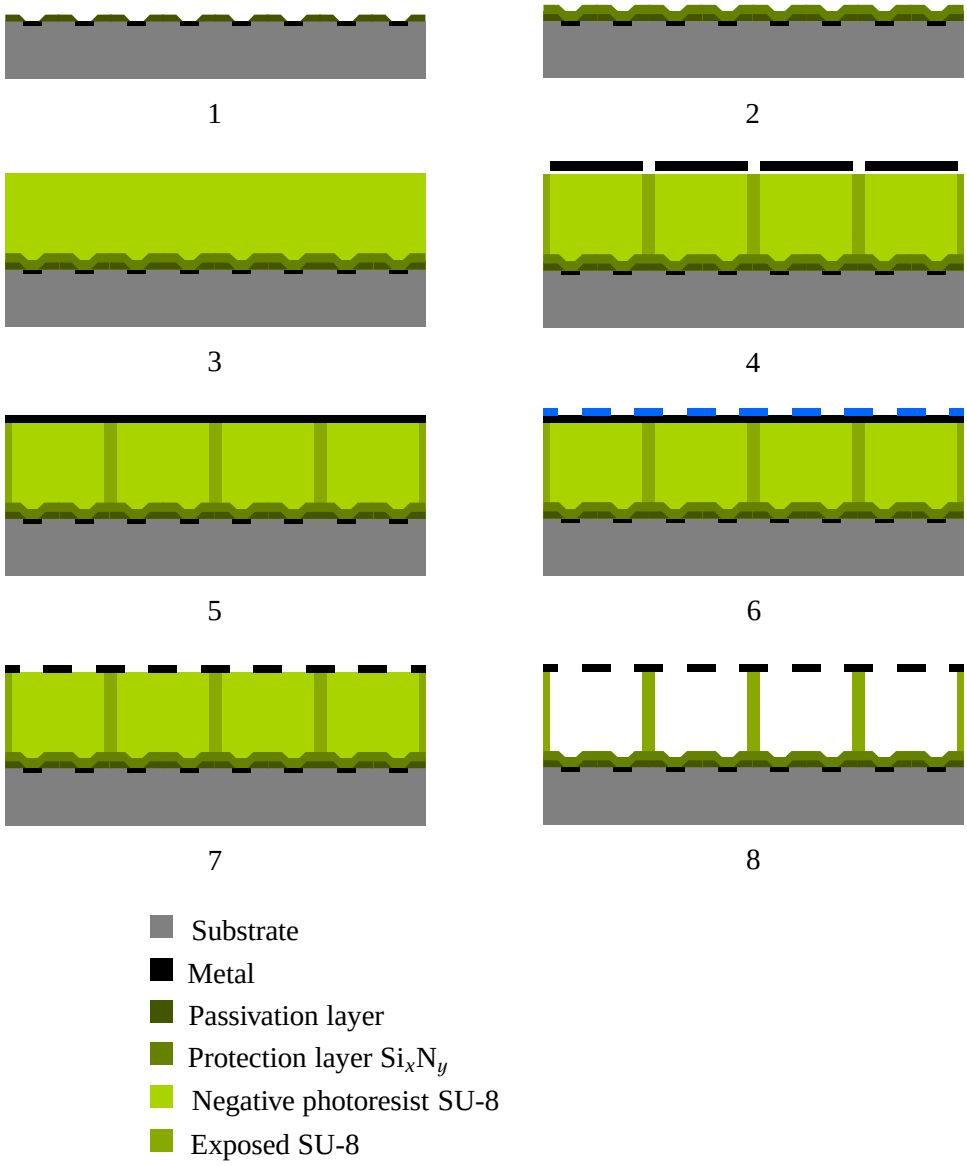

Figure 4.4: Process steps for fabricating an InGrid on top of a Timepix chip by photolithographic postprocessing

Chapter 5

X-ray detector

The x-ray detector constructed for this thesis is a small gas filled chamber with a highly granular, pixelized readout. It uses a GridPix (a Timepix chip with an InGrid on top) as readout with integrated gas amplification stage. In this chapter the requirements on the detector will be described which lead to its design criteria. Furthermore the detector itself and the readout system is object of this chapter.

5.1 Requirements on the detector

The requirements on the design of the detector can be splitted into two branches: Those requirements which are common for most gaseous detectors and are therefore generic, and the requirements arising from a possible operation at the CAST experiment.

Starting with the generic requirements, one has to build a detector which is as gas tight as possible to avoid oxygen and water contamination from the outside and the loss of gas to the outside. As the detector is flushed permanently with the gas (mixture) a small inner volume is advantageous meaning that it is possible to keep the gas inside the detector clean with low gas fluxes. For keeping the gas clean it is also important to avoid materials inside the detector volume which gas out. This especially concerns the choice of glues used inside the inner volume. An homogeneous electric drift field inside the detector especially above the readout area is required as well. Otherwise field inhomogeneities may distort the shape of drifting charge distributions inside the detector volume. To obtain an electric drift field as homogeneous as possible it is advisable to use flat anode and cathode plates to create the electric field. To avoid field inhomogeneities arising from boundary effects at the edges of the plates one can either use a field cage for shaping the electric field or one can use large anode and cathode plates to keep the volume above the readout structures as clean from field inhomogeneities as possible.

For being able to operate the detector at the CAST experiment it is necessary not to use ferromagnetic materials as at CAST the detector would have to be operable close to a magnet reaching field strengths up to 9 T. For being sensitive to low event rates (as for the CAST experiment but also any other experiment with very low event rates) it is important to take care of avoiding materials containing significant amounts of radioactive impurities. Materials with high radiopurity are for example aluminium, acrylic glass and Kapton foil [49, 54]. As the detector shall be sensitive for photons in the low x-ray regime ($\lesssim$ 10 keV) of course it has to have a window allowing the x-ray photons to enter the inner detector volume. On the one hand this window has to be transparent for x-ray photons and on the other hand it still has to be gas tight to seal the gas volume. For being sensitive in the low energy x-ray regime one also has to avoid copper inside the detector as copper has a fluorescence line at 8.1 keV which might get excited e.g. by cosmic rays. Despite copper also other metals have fluorescence lines in the x-ray regime. Aluminium has a line at 1.5 keV. But as the absorption cross section for photons is larger for lower energies in the x-ray regime the attenuation is higher so that it is less probable for x-ray photons to reach the active volume in the detector than for x-ray photons of higher energy. Thus the presence of aluminium inside the detector should less problematic than the presence of copper. To gain the necessary

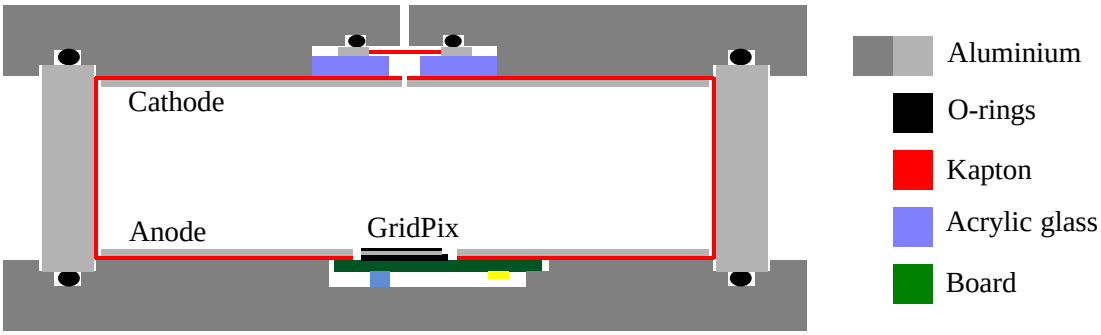

Figure 5.1: Schematic cut through the detector with used materials color coded.

sensitivity it is required for the detector to be efficient in the x-ray regime meaning to have a conversion probability for x-ray photons inside the gas volume as high as possible. Main ways to achieve this are operating the detector at high absolute gas pressure (~ 2 bar) using a gas with high atomic number. The operation at high pressure generates further requirements to the mechanical robustness of the detector (especially for the x-ray window) and again touches the requirement on gas tightness. A good candidate for a gas with high atomic number would be Xenon (or Xenon based mixtures) but as Xenon is very expensive and a closed gas loop system (with filters for oxygen, water and other gas impurities) was not available, Argon based gas mixtures were used instead.

5.2 Design of the detector

The detector consists of three parts which are mostly made of aluminium. A schematic cut through the detector can be seen in figure 5.1, the colors indicate the materials.

Starting with the part of the detector where the readout structure (GridPix) is nested is from now on called the bottom plate. The GridPix which is mounted on a carrier board is put into a slot of the bottom plate. The flat ribbon cable connecting the carrier board with an intermediate board outside the detector is fed through a well fitted slit in the bottom plate and sealed with a two component glue. From the intermediate board the connection to the readout system is done. The bottom plate is covered with the anode plate made of aluminium which has a cutout for the GridPix structure and its high voltage supply (see figure 5.2). As the anode plate will be on high voltage during operation it has to be isolated as the bottom plate is on ground potential (as also the rest of the detector's case). This is done by gluing a Kapton sheet (75 µm thickness) between anode and bottom plate. The high voltage supply for anode plate and GridPix structure are realized by feeding cables through holes in the bottom plate which are sealed with a two component glue to reach gas tightness. The electrical connection of the anode plate to its high voltage supply is done by feeding a small wire from the downside through a hole in the anode plate and clamping it with one of the plastic screws holding the anode plate at its position. The connection for the gas inlet is screwed into the bottom plate from the outside.

On top of the bottom plane is a ring. The inside of this ring is covered with Kapton foil to avoid discharges as it is close to anode and cathode plates. As the ring defines the distance between anode and cathode, the drift distance, this distance can easily be changed by replacing the ring by one with different height. The inner diameter of the ring is 82 mm. The ring used during the measurements described in chapter 7 gave a drift distance of 20 mm.

The top endcap is mounted on the ring and closes the inner detector volume. It contains the window allowing x-ray photons to enter the detector, the connection for the gas outlet and the cathode including

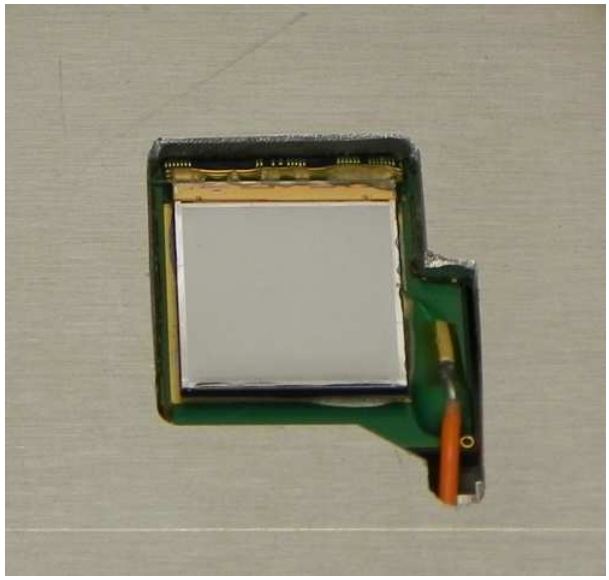

Figure 5.2: Picture showing the GridPix nested in the anode plate. At the right the high voltage supply for the GridPix can be seen (orange cable). At the top the wire bonds connecting the GridPix to its carrier board can be seen, they are covered with a glue to protect them.

its high voltage supply. The top endcap is also made of aluminium as the cathode plate is which is mounted from the inside of the detector onto the top plate and fixed with plastic screws. The connection of the cathode plate to its high voltage supply is done similar to the anode plate. Figure 5.3 shows the top plate with view onto the cathode plate. To avoid an uneven surface at the cathode the wire is put into a tiny notch leading from the feedthrough hole to the screw clamping the wire. A Kapton foil (50 µm thickness) is used as x-ray window. It is glued onto a small frame which is fixed with metal screws from the inside of the detector. To seal the point where the window is mounted an o-ring is used. The cathode plate has a small hole (1 mm diameter) where the window is located.

Gas tightness between these three parts is achieved by using o-rings and corresponding notches in the bottom plate and the top plate. In order to flush the inner detector volume, especially the volume above the GridPix the gas connections are arranged in a way that the gas flow crosses the volume above the GridPix. The completely assembled detector is shown in figure 5.4, the copper plate beneath the bottom plate can be used to mount a copper box enclosing the detector and acting as Faraday cage.

The two high voltage lines coming out of the bottom plate (one for the anode, one for the GridPix) lead to small metal box where they are connected with 10 MΩ resistors to standard high voltage connectors (SHV). In case of the high voltage line for the GridPix there are additional passive components inside the metal box for decoupling signals coming from the grid and to damp noise coming from the high voltage supply.

5.3 Distortions of the electrical field inside the detector

In an ideal case the electric drift field inside a gas-filled detector would be absolute homogeneous with no components perpendicular to the drift direction all over the readout region which would lead to perfect imaging. The detector described in the section before suffers from partly heavy field distortions. The causes for this distortions are mainly two things.

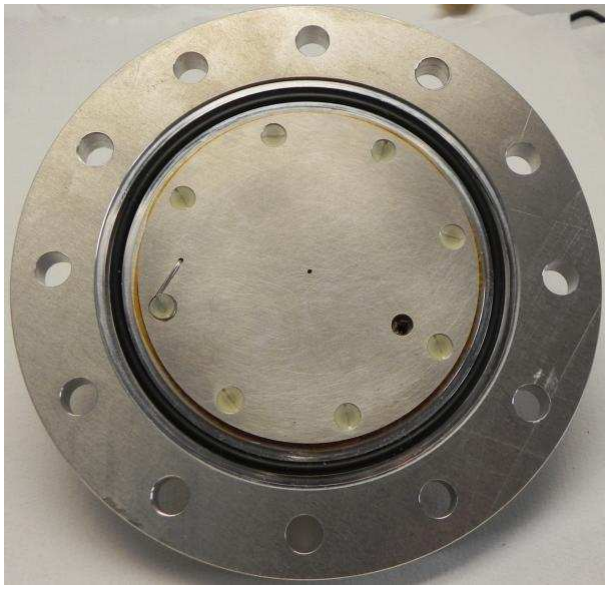

Figure 5.3: Picture of the top part of the detector as seen from inside. Cathode plate with x-ray window in its middle can be seen as well as the high voltage connection for the cathode (top left) and the gas outlet (down right).

There is on the one hand the finite size of anode and cathode which lead mainly to deviations from the design value for the drift field. As this detector was not build for reconstruction or precise measurement of tracks and as the drift distance of the electrons detected on the readout plane is not measured, the influence of this field distortions can be neglected. Also, the small maximal drift distance keeps the effect of this distortions low. Furthermore, this field distortions become higher the closer one gets to the edges of anode and cathode plate, so, for small distances between anode and cathode the influence of the distortions is very low at the middle of the detector, where the GridPix is nested. Nevertheless, this part of the whole field distortions could be minimized in a future version of the detector by using a field cage to shape the drift field better.

The second cause of field distortions inside the detector is the way the GridPix structure are mounted in the anode plate. The small gaps between the chip and the anode plate which are in the order of 0.5 to 1 mm lead to changes in the drift field at the edges and sides of the chip. These gaps also lead to electric field components perpendicular to the drift direction. The gaps are about 0.5 mm to 1 mm for most sides. However at the sides of the bond wires, the gap is about 4 mm to allow for sufficient insulation between the anode and the wire bonds which are on ground potential. Taking again a look at figure 5.2 one can see these gaps, also the part where the high voltage supply for the GridPix is done creates a very large gap.

The electric field inside the detector was simulated with the commercial simulation environment `Ansys`. Using a simplified model of the detector and typical values for the design value of the drift field and the applied grid voltage, one gets the electric fields shown in figure 5.5. There, it is clearly visible that from the gap between GridPix and anode (1 mm) quite strong field distortions arise.

There are several ways to minimize the field distortions arising from the gap between anode and GridPix or their influence. A simple approach is to reduce the size of the gap between anode and GridPix for example by applying metal foils, although, this can not be done at the side were the bond wires connecting the chip to its carrier board are localized. The only way to avoid the big gap at the bonding area of the chip would be to use a different chip instead of the Timepix in combination with the

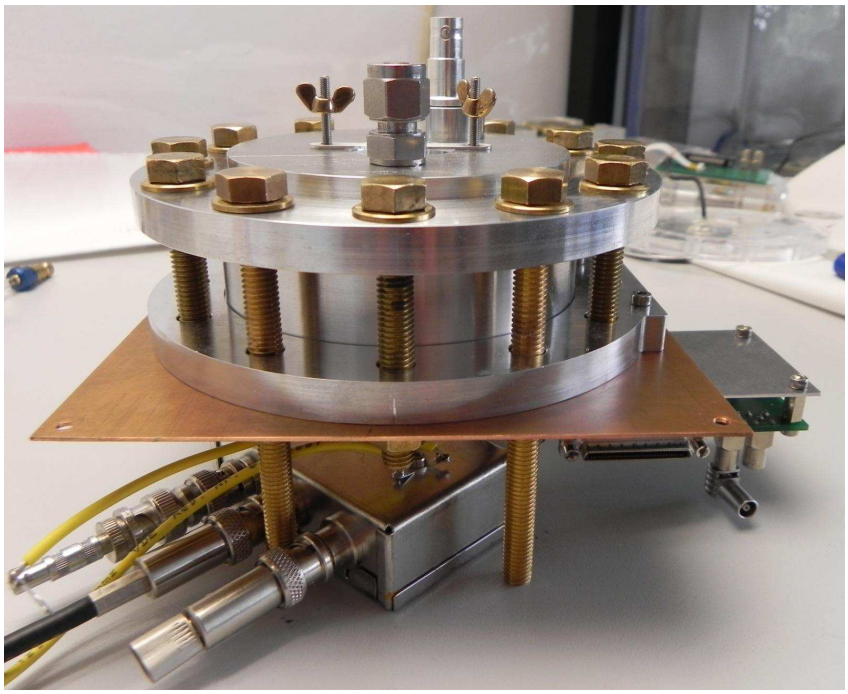

Figure 5.4: Picture of the x-ray detector, high voltage supply is connected to the connector on the top and to the connectors down left. The intermediate board at the right is connected to the MUROS.

InGrid structure on top which could be connected from the downside by Through Silicon Vias. Also, implementing the high voltage supply for the GridPix onto the carrier board would avoid the gap where the supply is done at the moment and, therefore, reduce the field distortions. One way to reduce the influence of the field distortions would be to put the GridPix deeper so that the anode plate would lie higher than the top of the InGrid which would allow to implement a Frisch grid into the anode plate for keeping the drift volume clean from the field distortions as the influence of the field distortions on the small distance between InGrid and Frisch grid [36] should be rather small.

5.4 Readout

The readout of the detector is realized by the use of a GridPix which is a pixelized readout with integrated gas amplification structure. The GridPix is glued onto a small printed circuit board called carrier board which is interconnected via a small flat ribbon cable with an intermediate board. This intermediate board is then connected with the **M**edipix re**U**sable **R**ead**O**ut **S**ystem (MUROS) which handles the communication with the GridPix. The connection of the GridPix to the carrier board is done with bonding wires. Also the high voltage supply for the grid of the GridPix is realized by a small metal pad on the carrier board from where bond wires are drawn onto the grid and attached with a conductive glue. In the following subsections a description of the GridPix and the MUROS will be given. As also attempts were done to decouple signals from the grid (gas amplification part of the GridPix) the way this was tried will be explained.

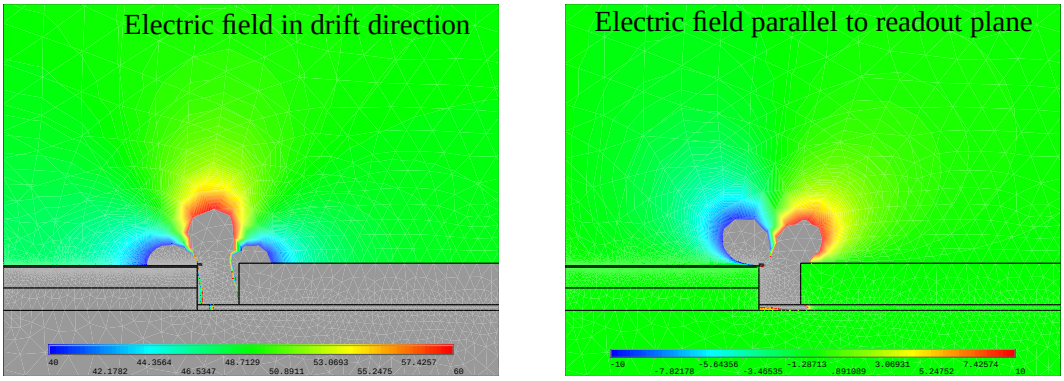

(a) (b)

Figure 5.5: Electric field inside the detector simulated with `Ansys`. Electric field in drift direction (a) and parallel to the readout plane (b). Color scale is from $-100\,{}^{\mathrm{V}}/_{\mathrm{cm}}$ (blue) to $+100\,{}^{\mathrm{V}}/_{\mathrm{cm}}$ (red) deviation from design value (green). The design value is $500\,\mathrm{V\,cm^{-1}}$ for the electric field in drift direction and $0\,\mathrm{V\,cm^{-1}}$ for the electric field parallel to the readout plane. On the left side of (a) and (b) half of the GridPix can be seen while to the right is the anode plate with a gap of 1 mm in between.

5.4.1 GridPix

GridPix is the combination of a Timepix chip (pixelized readout chip) with an integrated gas amplification structure (InGrid) which is put onto the Timepix by photolithographic postprocessing. The process used to create the integrated gas amplification structure on top of the Timepix chip was already introduced and explained at the end of chapter 4. For the chip used for the measurements done in this thesis, the protection layer was made of silicon nitride and had a thickness of 8 µm. This chip had no dead columns, just one hot pixel and a few noisy ones which were located at its sides in the dead area of the InGrid (where the ~ 500 µm wide walls are located which give mechanical stability to the InGrid structure). Even after about three months of operation and despite several discharges (especially at some of the expansion gaps of the mentioned walls) the GridPix showed no decrease of performance, meaning no detectable loss of sensitivity, no dead pixel or columns. Photos of a bare GridPix and a GridPix connected on its carrier board can be found in figure 5.6.

5.4.2 Timepix chip

The Timepix chip [55] is a pixel chip derived from the Medipix2 chip which is a pixel chip designed for the detection of single x-ray photons. The purpose of the Medipix2 is mainly medical imaging. Both, the Timepix and the Medipix2 have a total size of $14\times16\,\mathrm{mm^2}$ where $14\times14\,\mathrm{mm^2}$ are equipped with pixels. The area not equipped with pixels is used to connect the chip via bonding wires with its carrier board. Both chips have 256×256 pixels with a pitch of $55\times55\,\mu\mathrm{m^2}$. In fact these pixels are bumpbond pads used for bumpbonding a semiconductor detector onto the readout chip in which photons can convert into several electrons which are then collected at the pixel. The bumpbond pads are made of aluminium and are of octagonal shape with side length 10 µm. As the pixels do not cover the whole active area of the chip the remaining surface is covered with a passivation layer. Therefore, the pixels appear as openings in the passivation revealing the underlaying metal layer. Each of the pixels contains a charge sensitive amplifier, a discriminator, a 14-bit pseudo-random counter and the necessary communication

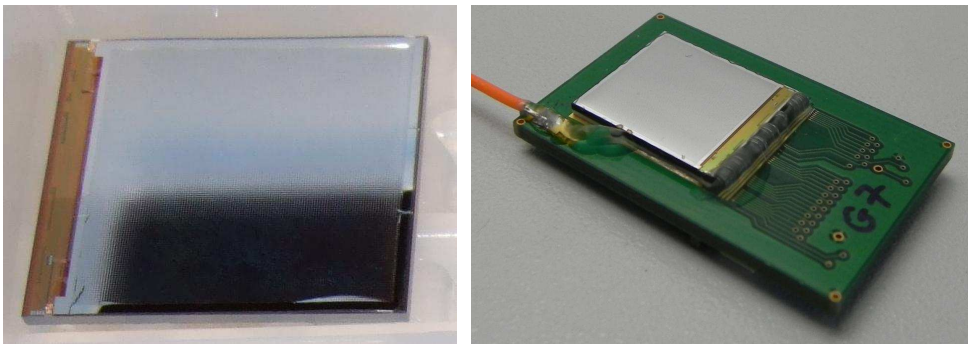

(a) (b)

Figure 5.6: Images showing a bare GridPix (a) and a GridPix on a carrier board (b) with high voltage supply on the left (orange cable).

logics. Settings for the readout electronics (for example thresholds for the discriminator) can be changed by the use of the chips internal 8-bit **D**igital to **A**nalog **C**onverters (DACs). To detect electrons directly with a Medipix2 or Timepix one removes the semiconductor detector and uses the bumpbond pads as charge collecting anodes of a gas amplification structure which has to be put on top to multiply incoming electrons to achieve amounts of charge large enough that the chip can detect them.

As the Medipix2 was designed for imaging it was just able to register if a pixel was activated (meaning that the charge collected on this pixel was higher than a threshold) or to count how often a pixel was activated during the acquisition.

The Timepix chip is a modification of the Medipix2 to make it suitable for gaseous detectors. The Timepix was produced by IBM using a 250 nm CMOS (Complementary Metal Oxide Semiconductor) process. The electronics contained in one of its pixel is shown in figure 5.7 as block diagram. The charge sensitive amplifier is an operational amplifier with capacitive feedback. To avoid pileup of incoming charges a constant current source (in this case a so called Krummenacher feedback [56]) is also implemented in the feedback loop of the amplifier. Charge arriving at the input of the amplifier is therefore integrated and generates a voltage signal at its output which has a fast rising edge and due to the Krummenacher feedback a slow and linearly falling edge. The output of the following discriminator is logical high when the output signal of the amplifier passes the adjustable threshold of the discriminator. It goes back to logical low when the amplifiers output signal falls below the threshold again. The equivalent noise charge for the Timepix is about 90 e.

The Timepix has to supplied with an external clock of up to 150 MHz. The Timepix offers two possibilities to use this clock signal. The 14-bit pseudo-random counters can count the clock cycles as long as the discriminator output is high meaning that the preamplifier output is above the discriminator threshold thus measuring the time the signal is above the threshold (**T**ime **o**ver **T**hreshold (ToT)). The ToT is proportional to the charge integrated in the charge sensitive amplifier due to the linearly falling edge of the amplifiers output signal. The other way is to count the clock cycles starting from the point the discriminator becomes high for the first time until the end of the acquisition thus measuring the **T**ime **o**f **A**rrival (ToA). Although the counters have 14-bit the highest number they can count is 11810 as they are pseudo-random counters and as some bits are reserved for other information. A timing scheme of the Timepix is shown in figure 5.8 already revealing some of its drawbacks.

The Timepix is not self-triggering, it needs a shutter signal. Only during the time this signal is logical low the pixels are armed meaning that they can measure something. Therefore, one needs to

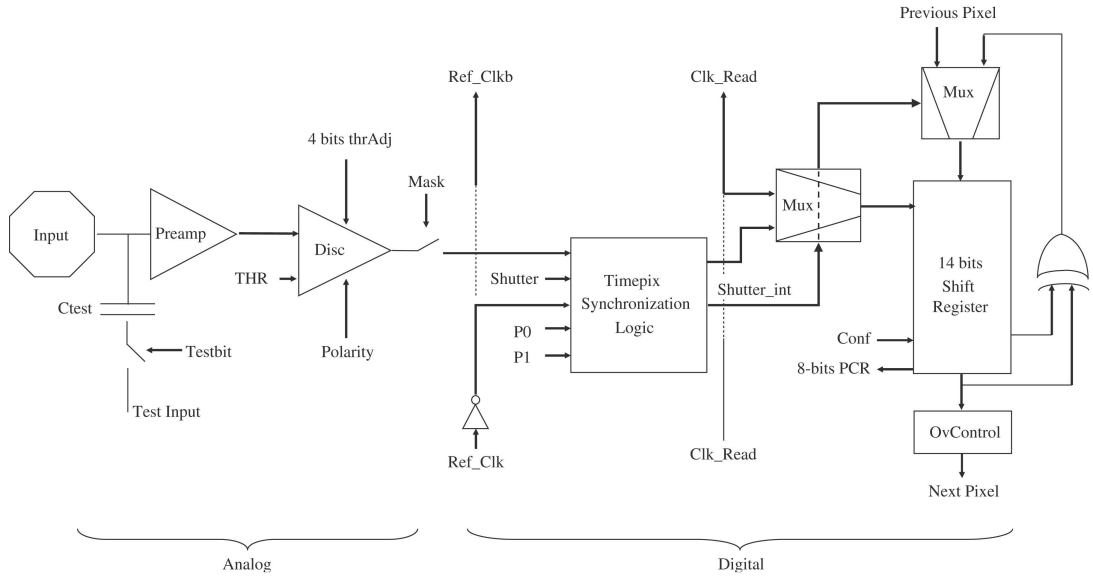

Figure 5.7: Block diagram of the electronics integrated in a Timepix pixel, taken from [55]. In the analog part on the left are the pad connected to the charge sensitive preamplifier and the discriminator. Test pulses can be injected with the capacitance also connected to the preamplifier input. The digital part of the pixel's electronics is shown on the right. Here the logics are located for defining the pixels mode, for counting clock cycles and for sending out the data.

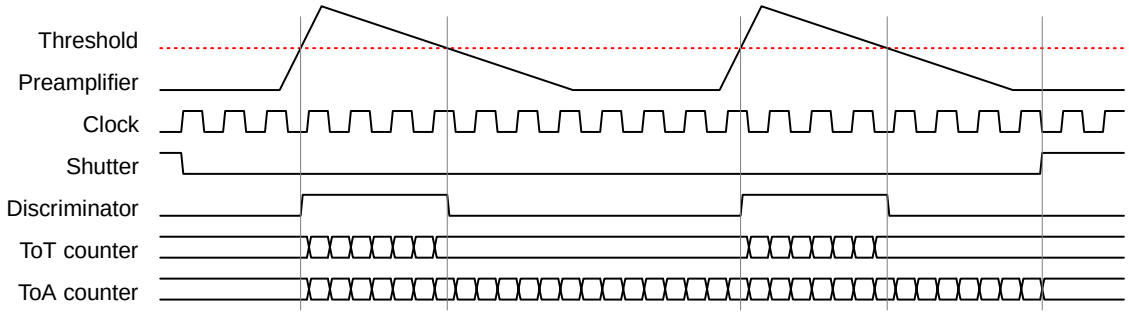

Figure 5.8: Timing diagram for the Timepix chip.

open the shutter window already before charge arrives at the pixels. Furthermore, in ToT or ToA mode the Timepix is not able to separate multihits, it is cannot distinguish if a pixel was activated once or several times, in case of ToT measurement it just integrates the whole charge arriving on the pixels during the time the shutter is open. This also illustrated in 5.8, when the preamplifier output passes the discriminator threshold a second time during one shutter window the counters just continue counting. In case of ToA measurement just the ToA of a pixels first hit is measured. Another drawback is of course, that the Timepix can only measure ToT or ToA for one pixel.

A new chip, the Timepix3, is under development and may be submitted in 2012. This chip will not need a shutter window anymore, it can trigger itself and is capable of dealing correctly with multihits. Also, the Timepix3 will be designed for connection via Through-Silicon-Vias.

For every pixel in the Timepix chip a small capacitance is connected to the charge sensitive amplifiers input. It is possible to send test pulses into the chip which are then distributed to the pixels' capacitance. By this one can inject defined charge pulses into the pixel electronics to calibrate the chip making it

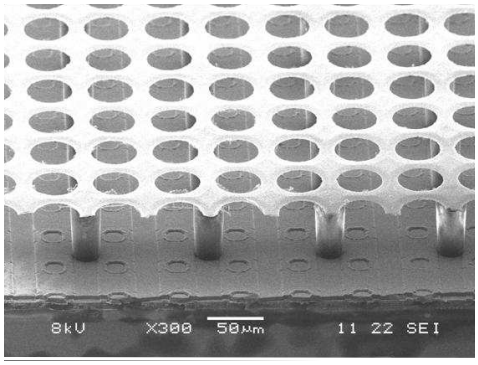

Figure 5.9: Scanning electron microscope image of an InGrid put ontop of a Timepix chip with protection layer in between, extracted from [41]

possible to convert the counted clock cycles for ToT measurement into amounts of charge. Due to process fluctuations during production of the Timepix chips the threshold of the discriminator may vary over the pixels of one chip resulting in a spread of the individual pixel thresholds. To compensate this each pixel has a 4-bit DAC with which the individual threshold can be tuned to reduce the threshold dispersion.

5.4.3 InGrid

The gas amplification structure of the GridPix is an integrated Micromegas or **In**tegrated **Grid** (InGrid). It is put onto the Timepix chip with photolithographic postprocessing. For the GridPix used in this thesis this was done on chip level at University of Twente and Nikhef in Amsterdam. In figure 5.9 a photo of an InGrid structure can be seen, there one can see the pixels of the Timepix as openings in the passivation layer of course the surface is covered with silicon nitride as protection layer. Also visible are the tiny insulating pillars holding the grid. By means of the very good alignment achieved with the postprocessing techniques the holes of the grid are centered above the pixels. For a suitable gas gain one is able to detect single electrons with the combination of Timepix with an InGrid.

For mechanical stability it is not possible to cover the whole Timepix active area with an active InGrid structure. To retain mechanical stability the sides of the active area are covered with $\sim 500\,\mu m$ wide walls instead of the tiny pillars. Those walls support the whole InGrid structure, on top they are also covered with the grid. They provide a place for connecting the grid with its high voltage supply. The negative photoresist (SU-8) which is used to form the pillars and the walls is hygroscopic and has different thermal expansion coefficients than the metal grid on top of it and as the underlaying silicon nitride. Therefore, expansion gaps are in the walls to avoid mechanical destruction of the InGrid structure due to thermal expansion. Of course these gaps can be preferred regions for discharges, if e.g. residuals from the fabrication process remained in these gaps. This was also seen during operation of the GridPix used in this thesis, but the frequency of this discharges decreased with the total operation time. As these discharges at the gaps are located in the inactive region of the InGrid they did not influence the GridPix operation.

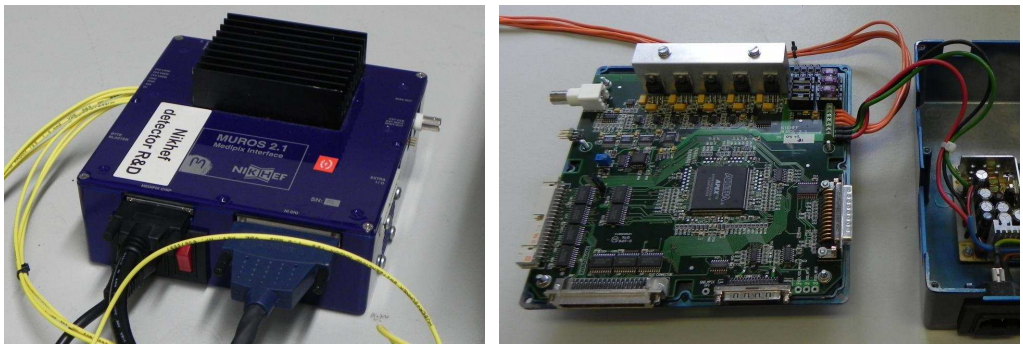

(a) (b)

Figure 5.10: Pictures showing the MUROS, closed (a) and opened (b).

5.4.4 The MUROS

The **M**edipix re**U**sable **R**ead**O**ut **S**ystem [57] is an interface system based on a FPGA (**F**ield **P**rogrammable **G**ate **A**rray). It is used as interface between the Timepix' carrier board and National Instruments DIO card (**D**igital **I**nput **O**utput). This DIO card is plugged into a computer. The MUROS was developed at the National Institute for Nuclear Physics and High Energy Physics (Nikhef) in Amsterdam. The MUROS handles the communication between computer and Timepix chip. For reading out a Timepix chip version 2.1 of the MUROS has to be used since version 1 is only capable of handling Medipix chips. Pictures of a MUROS2.1 can be seen in figure 5.10. The power supply for the Timepix chip is also implemented in the MUROS. The necessary voltages can either be created internally or they can be supplied from a stabilized power supply. The internal power supply of the MUROS supplying its electronics was also shunted out and replaced by a stabilized laboratory power supply to avoid noise coming from the internal power supply. The external clock signal needed for operation of the Timepix is also generated in the MUROS2.1, it can be set by using a screw driver on the potentiometer on its board. For the measurements of this thesis the frequency of the external clock was set to 59.8 MHz.

Readout and configuring of the Timepix chip as well as storing the data which was readout and visualizing it is done by the Pixelman software [58, 59] on a PC. This program is also capable of tuning the individual thresholds (Threshold equalization) in an automated way generating a matrix with the necessary DAC information to reduce the threshold spread. The injection of test pulses is also handled by the Pixelman software. During this thesis the Java version of Pixelman ‚JPixelman, was used in version 2.06.

5.4.5 Decoupling signals from the grid

To decouple the charge pulse from the high voltage supply of the GridPix' grid which is generated on it by the gas amplification a circuit as shown in figure 5.11 was used. The decoupled signal is then fed into a charge sensitive amplifier. The charge sensitive amplifier which was used to amplify the signal grid signal was a small preamplifier from the Honeycomb strip chambers [60] which were used at the P2 experiment (CERN), a picture of the amplifier is shown in figure 5.12. The signal at the output of the amplifier is inverted and shaped. The amplifier's integration time is approximately 10 µs and the height

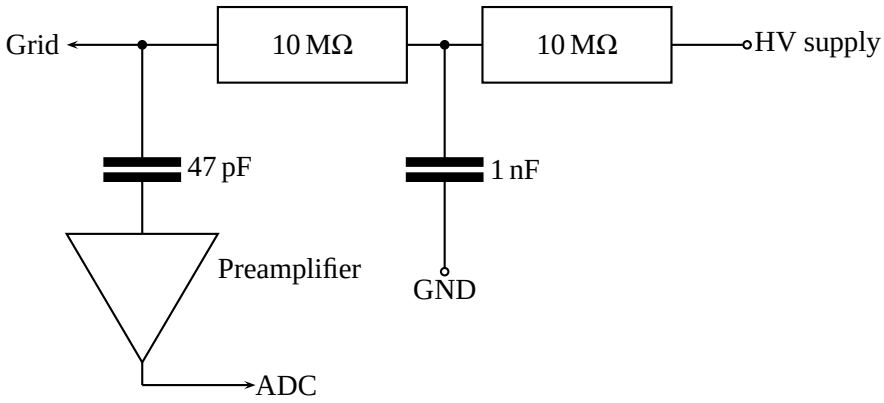

Figure 5.11: Circuit for decoupling signals from the grid.

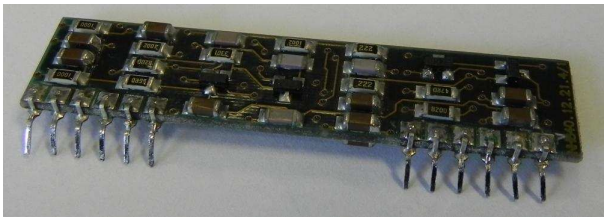

Figure 5.12: Picture of a Honeycomb preamplifier.

of the output signal correlates with the charge at its input as follows

$$U[\text{mV}] \approx 935 \cdot Q[\text{pC}] \tag{5.1}$$

$$\approx 1.5 \times 10^{-4} \cdot Q[e] \tag{5.2}$$

It was planned to sample the output signal of the charge sensitive amplifier with a FADC (Fast Analog to Digital Converter) to gain time information from the signal as for example the signal shape. Also, the decoupled signal may be used as a kind of trigger to end the current frame by triggering the shutter signal to go high (with some delay) and, therefore, start the readout of the Timepix chip (this is not possible yet as the MUROS does not support such operation, but a new more flexible readout system for the Timepix is under development). As during readout of the Timepix chip crosstalk from its data lines to the grid is expected and unavoidable one could use the Timepix' signals which indicate its status (meaning if its transmitting or receiving data) to veto the FADC.

Unfortunately, it was impossible to sample the output signal of the amplifier as there was a large amount of noise on its output (not coming from communication of the Timepix chip). The noise' amplitude was in the range where real signals from the grid were to be expected (50 to 200 mV). Therefore, many fake triggers would have shown up in the self-triggering FADC which makes the sampling of the grid's signal useless. For this reason the signal from the grid was not used for the measurements of this thesis. Nevertheless, it was possible to see signals from the grid in case of discharges which generate very large amounts of charge on the grid large enough to clearly be separated from noise. Most of these discharge signals already put the amplifier's output into saturation meaning more than 1.5 pC ($9.36 \times 10^6\, e$) arriving at the grid.

The before mentioned noise seemed to couple in from the outside or by the grounding of the detector

and the amplifier. So, it should be possible to get rid of most of the noise by applying proper grounding to the detector, its supplies and of course readout electronics and amplifier. Also improvements of the electromagnetic shielding (meaning Faraday cage(s) and shielding of cables) should improve the noise problem. Especially a proper shielding of the small piece of cable between the grid an the point where the signal is decoupled from the high voltage supply may have a positive effect on this. Also the use of an Online-UPS (**U**ninteruptable **P**ower **S**upply) might be useful as it fully decouples the systems supplied by it from the energy net. By this one could get rid of noise which is on the power lines and would therefore couple in through all devices which have to be supplied with power.

Chapter 6

Data analysis

In this chapter the analysis framework MarlinTPC [61] will be shortly introduced. Also, the charge calibration performed for the Timepix chip used in this thesis will be presented shortly. It will be explained how the x-ray events were reconstructed and analyzed. Also the cuts applied to obtain clean spectra of the used ^{55}Fe source will be presented and motivated. A very simple simulation of x-ray events based on `root` libraries will be presented which was used to check the reconstruction and analysis chain for artifacts as well as to look for imperfections of the detector.

Last but not least the algorithm based on likelihood ratios which was used to discriminate background events from x-ray events, will be introduced and explained.

6.1 Analysis framework

The reconstruction and analysis of data was done using the MarlinTPC framework which is based on the Marlin (Modular Analysis and Reconstruction for the Linear Collider) but has additional tools for reconstruction of data taken with time projection chambers (TPC). The framework was chosen because several analysis steps like reading in data and calibration were already implemented.

This modular framework consists of different modules which process the events one after another resulting in a reconstruction and analysis chain. One module reads in the data and converts it into the data format of the framework, the next modules suppresses zeros in the data, the next applies a charge calibration, the next one reconstructs e.g. clusters and so on. The last modules create the analysis plots. The sequence of this modules and their individual parameters are defined in steering files (XML files) which define and control the reconstruction and analysis chain.

This framework was already used for data with Timepix chips (TPCs with Triple-GEM stack and Timepix readout) many modules needed for working with Timepix data already exited so that only a few new modules had to be created for this thesis and the analysis of x-ray events. Sometimes also existing modules could be modified to be used for the x-ray events. As MarlinTPC is designed for tracking applications many modules to find and reconstruct tracks of charged particles are already included which could be used for the discrimination of background events as it was done in this thesis by differentiating the hypothesis of a x-ray event and the hypothesis of a charged particles track.

6.2 Charge Calibration

In order to convert the number of clock cycles measured in the ToT mode to a charge, a charge calibration needed. As already mentioned each pixel on the Timepix chip has its own test input which can be used to send test pulses to the pixels. The distribution of the pulses over the chip is handled by the electronics of the Timepix chip. The control of the test pulse distribution is done with the Pixelman software, an external pulser is connected to the test pulse input of the intermediate board of the readout electronics.

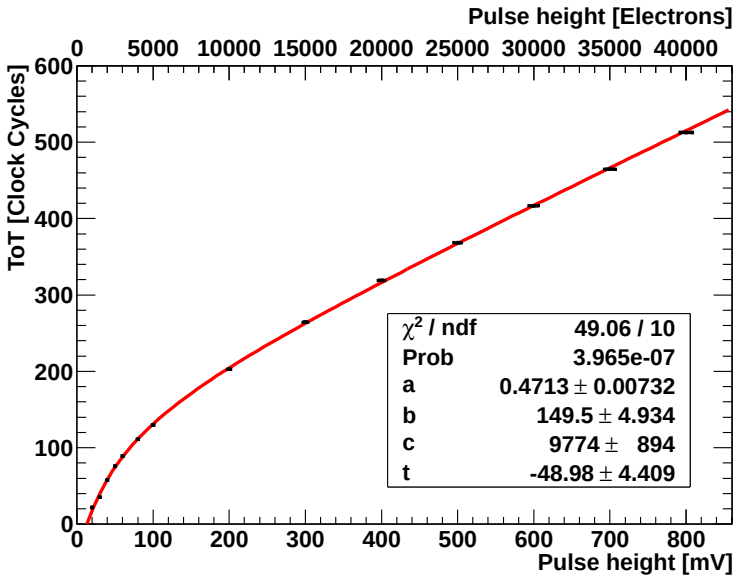

Figure 6.1: Charge calibration for the Timepix used in this thesis, fit function which is later used to calibrate the taken data including fit parameters is also shown.

The pulser gets triggered by the MUROS. The calibration procedure is done as described in [62]. The calibration is done for the whole chip by averaging over all pixels. The result for the chip used in this thesis is shown in figure 6.1, a function

$$\mathrm{ToT[clockcycles]} = aU_{\mathrm{inj}}[\mathrm{mV}] + b - \frac{c}{U_{\mathrm{inj}}[\mathrm{mV}] - t} \tag{6.1}$$

$$\mathrm{ToT[clockcycles]} = \frac{a}{50}Q_{\mathrm{inj}}[e] + b - \frac{c}{\frac{Q_{\mathrm{inj}}[e]}{50} - t} \tag{6.2}$$

$$Q_{\mathrm{inj}}[e] = \frac{CU_{\mathrm{inj}}}{e} \approx 50 \cdot U_{\mathrm{inj}}[\mathrm{mV}] \tag{6.3}$$

with $C = 8\,\mathrm{fF}$ the capacitance for injecting test pulses and a, b, c and t as free parameters was fitted to the calibration data for later converting the measured number of clock cycles into the accumulated charge. The fitted function is arbitrary and has no physical motivation, it was chosen in [62] to fit the data.

From the calibration graph one can see that the threshold used for the measurements is at approximately $800\,e$ and therefore far above the noise level of the Timepix chip as it has an equivalent noise charge of about $90\,e$ [55]. The obtained fit parameters which are used later for charge calibration of the data are

$$a = 0.4713 \tag{6.4}$$

$$b = 149.49 \tag{6.5}$$

$$c = 9774 \tag{6.6}$$

$$t = -48.98 \tag{6.7}$$

they were gathered by using a ROOT fit.

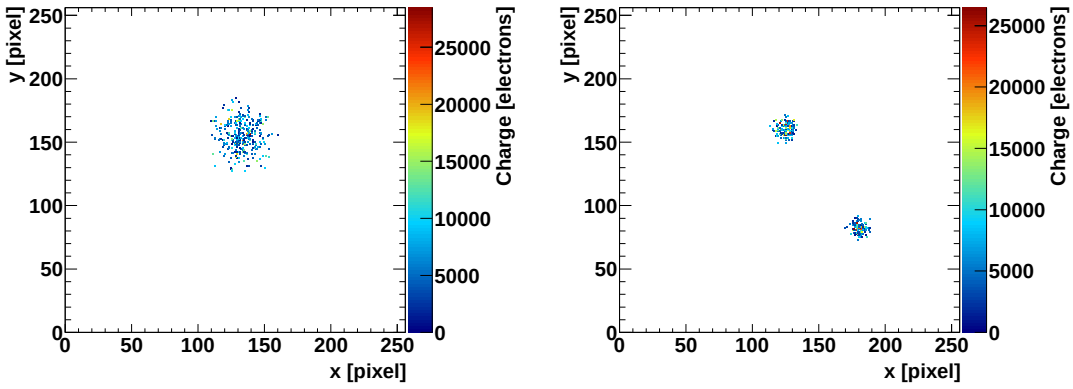

(a) (b)

Figure 6.2: Typical x-ray events as they are recorded with the GridPix: Charge cloud of a single x-ray photon (a) and charge clouds of two x-ray photons converted in one frame (b) where the second photon might be an escape photon. Both events were recorded using a gas mixture of 95% Argon and 5% Isobutane (Ar/iC_4H_{10} 95/5).

6.3 Analysis of x-ray events

X-ray photons converting inside the detector leave an ionization trace in the detector. The electrons in this trace drift to the readout (GridPix = Timepix + InGrid) where they get multiplied and detected. Due to diffusion the cloud of secondary electrons widens during drift. Therefore, the GridPix records a projection of the electron distribution onto the readout plane. If the charge cloud has drifted a distance long enough to separate all electrons by means of diffusion the position of each individual electron in the cloud can be recorded with a precision of $55\,\mu m/\sqrt{12} \approx 16\,\mu m$ in both coordinates. This high spatial resolution can be exploited to do a precise event shape analysis which can be used to separate x-ray events from background events. Figure 6.2 shows two typical x-ray events as they are observed with the GridPix readout, it is clearly visible that the high spatial resolution for single electrons allows a precise analysis of the event shape.

The first step of course is to reconstruct the x-ray photons in one event which means to combine all electrons (or pixels) originating from one x-ray photon in one x-ray object. To recognize the pixels belonging together an algorithm was implemented by modifying a standard cluster algorithm which takes adjacent pixels and puts them into one cluster object. This standard cluster algorithm for use with data from a Timepix chip was already implemented in MarlinTPC [63]. This algorithm was modified to search not only for adjacent pixels but also for nearby pixels in an adjustable square around every pixel. Thus allowing some distance between the pixels of one x-ray object ensures taking all pixels of one x-ray object into account but also enables separation of two x-ray objects in one event if their gap is wide enough. An distance of 10 pixels in each direction was found sufficient to find all pixels of one x-ray object but still allowing some separation.

For the x-ray objects some characteristic properties can be given, their center, the number of activated pixels which is the number of secondary electrons in the charge cloud for full separation and also the total amount of charge (sum of charge over all activated pixels) in one x-ray object. The latter should correspond to the number of secondary electrons and, therefore, to the energy of the incident x-ray photon. In case of low diffusion, when secondary electrons may end up on the same pixel, the total charge should still be a good estimator for the energy of the x-ray photon, since it is integrated over

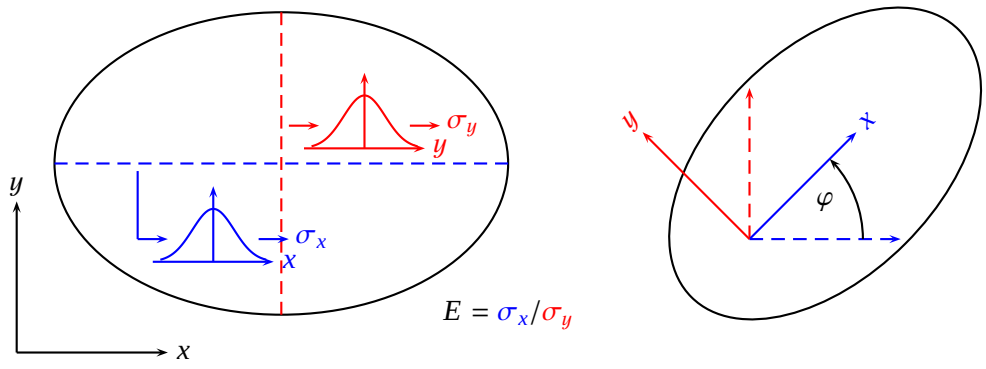

(a) (b)

Figure 6.3: Sketches illustrating the calculation of the eccentricity E. A two dimensional distribution is projected on the axis of the coordinate system (a), E is calculated from the widths of the projected distributions. To find the eccentricity for randomly oriented distributions, the coordinate system is rotated by an angle φ (b) so that the eccentricity resulting from the projection on the axis of the coordinate system becomes maximum.

overlapping electrons.

The general shape of the x-ray objects is elliptical so that they can be described by the direction of their long axis and their eccentricity E. The eccentricity is a measure for the deviation from a circular shape, it is defined as the width of a two dimensional distribution along one axis divided by the width of the distribution along the perpendicular axis (see figure 6.3a)

$$E = \frac{\sigma_x}{\sigma_y} \tag{6.8}$$

where σ_x and σ_y are the widths of the distributions along the two perpendicular axis. For getting the eccentricity characterizing the elliptical shape one has to find the long respectively the short axis of the ellipsis and calculate the eccentricity in the coordinate system given by these axis. Therefore, one has to rotate the coordinate system to match it with ellipsis' axis. This was done by taking the eccentricity as function of the rotation angle φ and maximizing this expression with the tool `Minuit2` which is included in `ROOT`. The resulting angle φ defines the direction of the long axis of the ellipsis (see figure 6.3b).

For the following analysis of the object's shape the coordinate system defined by the long and short axis of the ellipsis is used which can be transformed to by rotating the standard coordinate system given by the Timepix with the angle φ. As the electron cloud originates from the ionization trace of an primary electron for small drift distances the direction of this primary electron is still visible and is the reason for the eccentricity of the cloud. For longer drift distances this direction is washed out due to diffusion. For gas mixtures with large effective ranges for electrons along with small diffusion coefficient (gas mixtures with low density) the track of the primary electron can become clearly visible even for long drift distances. So there are two cases, that the eccentricity is caused by the direction of the primary electron still dominating the clouds shape or by statistical fluctuations of the diffusion causing the distribution to deviate from a circle. As the direction of emission in this plane is uniformly distributed for photoelectrons as well as for Auger electrons, the angle φ is expected to follow a uniform distribution.

To analyze the events shape statistical momenta are calculated for the distributions of the electrons projected either onto the long or onto the short axis of the ellipsis. First of all the width σ_x of the projected distribution is calculated which is the second central moment of the distribution and is also known as the root mean squared

$$\sigma_x^2 = \frac{1}{n}\sum_i (x_i - \bar{x})^2 \tag{6.9}$$

where n is the number of pixels, $\bar{x}$ the mean value for the distribution along one of the axis and x denotes the coordinate of the pixels projected onto either the long or the short axis. The next statistical moment used in the analysis is the Skewness S_x which is the third central moment of a distribution defined as

$$S_x = \frac{1}{n\sigma_x^3}\sum_i (x_i - \bar{x})^3 \tag{6.10}$$

which is measure for the asymmetry of a distribution. A distribution with $S_x = 0$ is completely symmetric around its mean, while $S_x \neq 0$ indicates an asymmetry. A distribution with $S_x < 0$ has a longer tail left to its mean than to the right and therefore more entries larger than its mean than lower and for $S_x > 0$ vice versa. Also the fourth central momentum is used for the event shape analysis. The statistical moment Kurtosis K_x is given by

$$K_x = \left(\frac{1}{n\sigma_x^4}\sum_i (x_i - \bar{x})^4\right) - 3 \tag{6.11}$$

and holds information about the shape of the distribution. A Gaussian distribution results in a $K_x = 0$. Smaller values of K_x indicate more flat distributions while larger values show up for narrower distributions.

6.4 Simulation of x-ray events

In order to check the full reconstruction and analysis chain a small simulation was implemented to create artificial x-ray events. For this toy Monte Carlo a tool was designed by using `ROOT` libraries and especially the random number generators implemented in `ROOT`. To avoid correlations between the generated random numbers the generator `TRandom3` (which is based on the `Mersenne Twister` [64]) was used if possible. The simulation is based on phenomenological descriptions of the physics processes and does not involve a full simulation from first principles. The simulation setup for this thesis assumes an ideal detector without field distortions and so on. To improve the simulation, the tool `garfield++` could be used in combination with electric field maps generated with `Ansys`.

The simulation starts with generating a photon of energy 5.9 keV with a random direction within the cone defined by the opening angle of the detectors x-ray window. The distance the photon travels before it converts by the photoelectric effect is randomized according to

$$\frac{\mathrm{d}\Delta N(x)}{\mathrm{d}x} \propto \mu e^{-\mu x} \tag{6.12}$$

which gives the number of photons absorbed in dx with x the distance the photon traveled. This expression can be derived from the intensity attenuation of a photon beam

$$I(x) = I_0 e^{-\mu x} \tag{6.13}$$

where $I(x) \propto N(x)$ is used. If the photon converts inside the detector three cases are considered:

- The full energy is transferred to one photoelectron
- One photoelectron with 2.694 keV plus one Auger electron are emitted
- One photoelectron with 2.694 keV plus one escape photon are emitted

The probabilities for the three cases are given at the end of chapter 3. The direction of an emitted Auger electron is generated randomly according to uniform distribution in solid angle. The direction of emission for photoelectrons is generated according to uniform distribution in the azimuthal angle with respect to the incident photons direction. The angle θ inclined with the incident photon's direction, however, is distributed according to

$$\frac{\sin^2\theta}{(1-\beta\cos\theta)^4} \tag{6.14}$$

where β is calculated from the electron energy. The length of the electron tracks is calculated from their energy from equation 3.13. The number of secondary electrons created through ionization along the track is distributed Gaussian with the mean given by the electrons energy divided by the mean ionization energy of the gas mixture and a width including the Fano factor (see chapter 3). The secondary electrons are uniformly distributed along the track.

The mapping of the secondary electrons onto the readout plane is diffused with a two dimensional Gaussian distribution around its point of origin and with a width given by the diffusion coefficient for the gas mixture and its distance to the readout plane.

The positions of the secondary electrons at the readout plane are then matched to a grid defined by the Timepix pixels. For each electron the gasamplification is generated according to a Polya distribution for which the parameters are taken from a fit to real data. After the number of electrons per pixel is calculated the total charge on each pixel is converted into the number of clock counts for ToT mode using the calibration curve for the chip. The simulation tool writes the data in the same format as the Pixelman software, so that the whole chain of reconstruction and analysis can be applied also on the artificial events.

This simulation was compared with real data taken at a grid voltage of 350 V with Ar/iC_4H_{10} 95/5. The diffusion coefficient for the used drift field of 225 $^{\mathrm{V}}/_{\mathrm{cm}}$ was simulated by using `Magboltz` [65] to have a value of $D_t = 479\,\mu\mathrm{m}/\sqrt{cm}$. A Fano factor of 0.25 was assumed and the mean ionization energy was calculated from the mean ionization energies of Argon and Isobutane

$$w_{95/5} = 0.95 w_{\mathrm{Ar}} + 0.05 w_{\mathrm{iC_4H_{10}}} = 26\,\mathrm{eV} \tag{6.15}$$

with numbers taken from [37]. As the simulation does not include Penning effect or charge sharing between pixels the spectra are expected to only match qualitatively with real data. The parameters for the Polya distribution were obtained by fitting a Polya distribution to the distribution of the charge per isolated (no activated neighbors) pixel. Due to charge sharing between pixels (see chapter 7) this is also a simplification of the simulation. To illustrate the qualitative agreement of the simulated and therefore artificial x-ray events with real data, in figure 6.4 one artificial and one real x-ray event are shown. In figures 6.5 to 6.8 only the results of the event shape analysis for the Monte Carlo x-ray events are compared for real data.

One can see that the reconstructed event shape (Kurtosis, Skewness and Width) match quite well with the real x-ray events. For this one can conclude that the Monte Carlo x-ray event production reproduces the physical processes in the detector qualitatively. Differences can be seen for the eccentricity, the real x-ray events are more lengthy and they show a kind of preferred direction which cannot be explained by the conversion of the x-ray events inside the detector. Interestingly the preferred direction can be

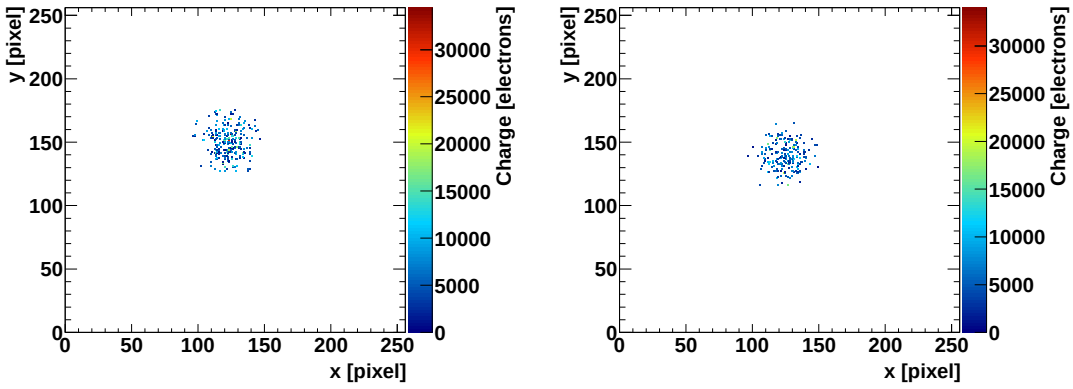

(a) (b)

Figure 6.4: Artificial (b) and real (a) x-ray events

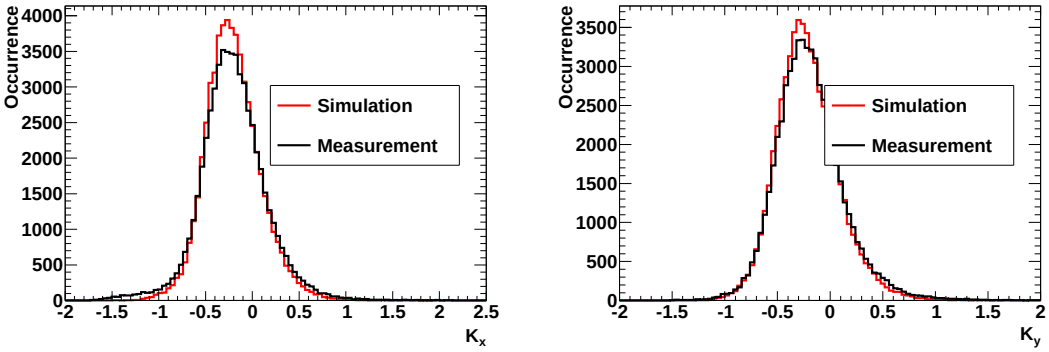

(a) (b)

Figure 6.5: Comparison of Kurtosis for artificial and real x-ray events: Kurtosis along the long axis (a) and along the short axis (b)

identified with direction in which the bonding wires of the Timepix and therefore the largest gap between GridPix and anode plate is oriented. So, probably the preferred direction and the larger eccentricity is due to distortions of the electric field which are not taken into account by the simplified simulation.

6.5 Energy Spectra

In order to obtain clean energy spectra from the data taken with the radioactive ^{55}Fe source it is necessary to clean the data. There two kinds of events which have to be removed in order to be able to extract characteristics of the detector from the data, as efficiency, energy resolution and obtained gas gain. The one kind are background events e.g. tracks of cosmic muons or other charged particles. The other kind of events to be removed from data are events where two or more x-ray photons converted in one frame which could not be separated due to low distances to each other.

Cleaning of data from those invalid (x-ray) events is done by applying cuts on the data. The cuts used

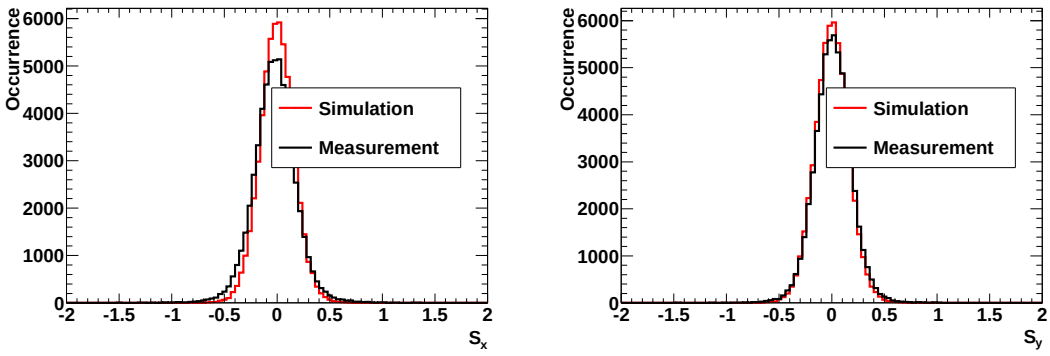

(a) (b)

Figure 6.6: Comparison of Skewness for artificial and real x-ray events: Skewness along the long axis (a) and along the short axis (b)

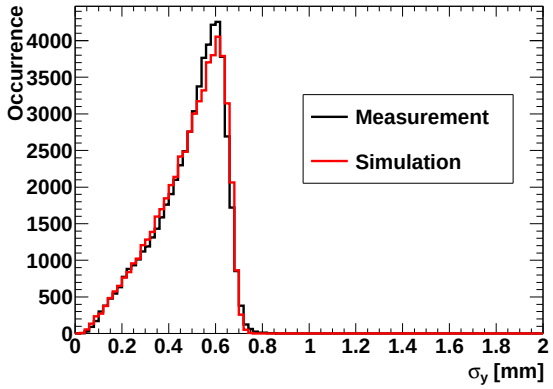

Figure 6.7: Comparison of width along short axis for artificial and real x-ray events.

will be presented in the following. As the x-ray photons originating from the radioactive source can enter the detector only through the small window in its top the center positions of the resulting electron clouds detected by the GridPix have to be in a certain area of the readout plane. The position of the window is governed by looking at an integral image of whole run with radioactive source consisting of ~ 50 k x-ray events. Summing up of all these events gives a clear image (see figure 6.9) of the radioactive source seen through the x-ray window. From this one can extract the position of the window, as one can already see in figure 6.9 it is slightly displaced with respect to the GridPix' center. Around this center point a circle with radius 2 mm is defined as area for valid x-ray events. The radius of the circle takes into account the opening angle of the detector as well as the displacement of the center of the charge cloud with respect to the photons conversion point. The cut on the center position is shown in figure 6.10.

In addition to this cut on the position also cuts on the events shape are used. Cuts on the Skewness and Kurtosis along the short axis (figures 6.11 and 6.12) are applied to remove events deviating too much from the mean of the distributions. As the width of the charge clouds is limited due to diffusion given by the diffusion coefficient and the maximum drift distance of 2 cm x-ray objects with $\sigma_y > 700\,\mu$m were

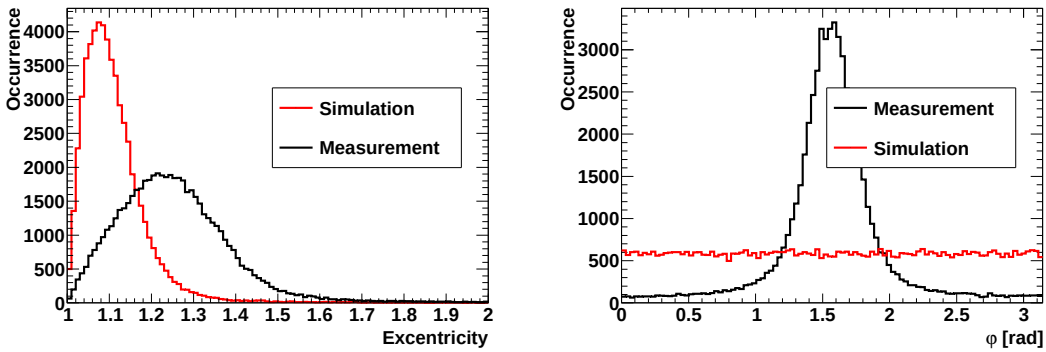

(a) (b)

Figure 6.8: Comparison of eccentricity for artificial and real x-ray events: Excentricity (a) and direction of the long axis (b) which is given by the rotation angle φ

removed. This cut on the width along the short axis is shown in figure 6.13.

To remove the unseparated multiphoton events in a last step a cut on the eccentricity is applied. Unseparated events result in lengthy x-ray objects and therefore in a larger eccentricity than single photon events. The cut on eccentricity is shown in figure 6.14. Figure 6.15 shows the result of the applied cuts. In the spectra the cuts reduce the background at the very left of the distributions as well as the number of x-ray objects with two times the number of pixels of the photopeak which result from unseparated double photon events.

6.6 Discrimination of background events

In a gaseous x-ray detector there are two kinds of background events which occur. On the one side there are real x-ray photons emitted by the detector material itself either due to radioactive impurities or due to excitation of fluorescence lines in the x-ray regime. This kind of background limits the detectors performance, background rate, as it not possible to distinguish those x-rays from the x-rays one is looking for in an experiment with low event rates. Additionally there is background originating from charged particles traversing the detector and creating ionization traces (tracks) (see figure 6.16 for a typical track as observed in the detector). These straight tracks are in principle rather simple to discriminate in the analysis, but parts of the ionization trace may look like the electron clouds produced by x-ray photons (this may e.g. happen when δ-electrons are created or if a charged particle is stopped inside the detector). Therefore, parts of the tracks can mimic x-ray events.

To discriminate the background events originating from charged particles track an algorithm was build using a likelihood ratio method. Therefore, for every event two hypothesis were stated, that this event was either created by a x-ray photon or by the track of a charged particle. For every event a track reconstruction was done, consisting of finding the track with a Hough transformation [66] and calculating the track parameters with a linear regression. The modules for track finding and reconstruction were already implemented in MarlinTPC [63]. These algorithms also reconstruct tracks of x-ray events. Also for every event x-ray objects were reconstructed with the algorithm presented before. Now, for the reconstructed track and the reconstructed x-ray objects properties describing the events shape are used to decide between the two hypothesis.

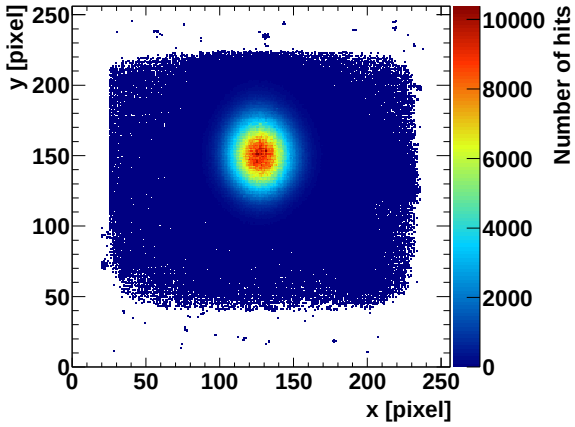

Figure 6.9: Integral image of the ^{55}Fe source as seen through the x-ray window. Integral image recorded at grid voltage of 350 V. Position of source is clearly visible.

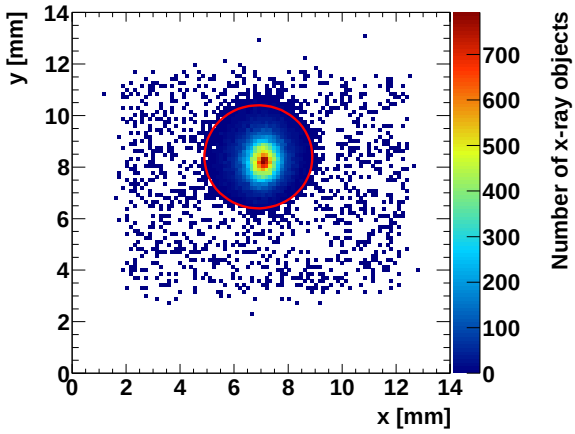

Figure 6.10: Center positions of x-ray objects and cut applied. Data shown was recorded at grid voltage of 350 V.

The likelihood $\mathcal{L}$ is the probability that under assuming a certain hypothesis the measured value for some variable occurs. This probability can be obtained from a histogram created either with reference data or by simulation. The likelihood ratio is a way to decide between two hypothesis. If one has to distinguish between two hypothesis H_1 and H_2 and has measured the value χ for the variable x the likelihood ratio Q is given by

$$Q = \frac{\mathcal{L}(x = \chi|H_1)}{\mathcal{L}(x = \chi|H_2)} \tag{6.16}$$

where $Q < 1$ would lead to rejection of H_1 and $Q > 1$ to a rejection of H_2. If several variables x_i with measured values χ_i exist, these can be combined in one likelihood ratio

$$Q = \prod_i \frac{\mathcal{L}(x_i = \chi_i|H_1)}{\mathcal{L}(x_i = \chi_i|H_2)} \tag{6.17}$$

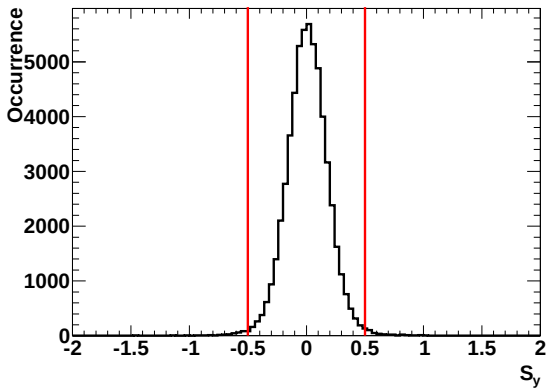

Figure 6.11: Skewness along short axis and cuts applied. Data shown was recorded at grid voltage of 350 V.

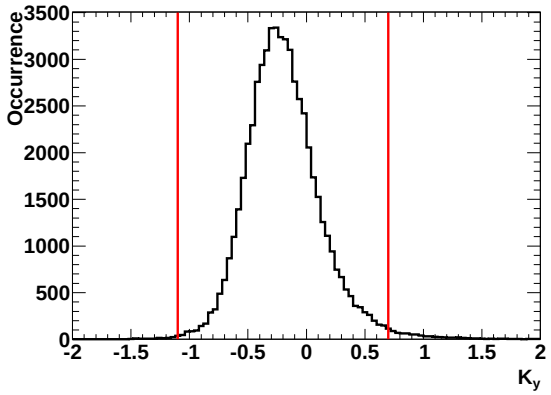

Figure 6.12: Kurtosis along short axis and cuts applied. Data shown was recorded at grid voltage of 350 V.

or by using the logarithmic likelihoods

$$\log Q = \sum_i \log \mathcal{L}(x_i = \chi_i | H_1) - \sum_i \log \mathcal{L}(x_i = \chi_i | H_2) \tag{6.18}$$

which is often more convenient as addition is easier than multiplication. In the latter case H_2 is rejected for $\log Q > 0$ and H_1 is rejected for $\log Q < 0$. Despite the quite intuitive cut at $\log Q = 0$, which arises from the definition of the likelihood ratio, other cut values are of course possible.

For the discrimination between the track and the x-ray hypothesis different event shape variables from the reconstructed track and the reconstructed x-ray object were considered. The likelihoods were obtained from reference data sets. For the x-ray hypothesis data from the runs with radioactive source was used as reference assuming only very low contamination with background events. As the energies emitted by the source are known, x-ray objects which could not be assigned to the peaks in the spectrum were removed to clean the data set a bit. The reference data for the track hypothesis was created from data obtained during a background run with full lead shielding, again assuming only low amounts of background. Using the same dataset for defining the reference set and for the final analysis will give rise to correlations, but could not be avoided since only this dataset was available.

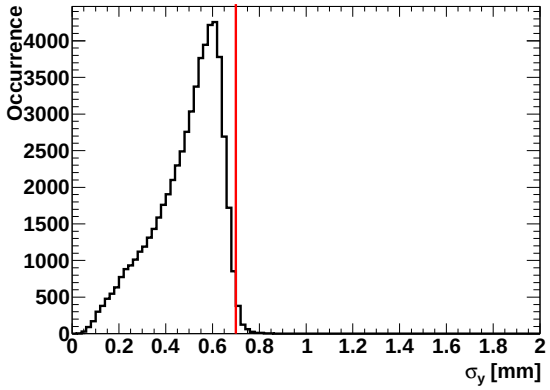

Figure 6.13: Width along short axis and cut applied. Data shown was recorded at grid voltage of 350 V.

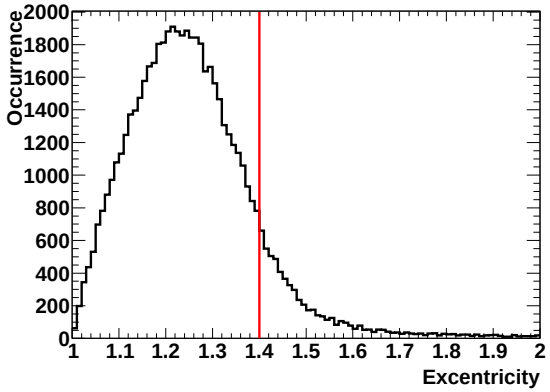

Figure 6.14: Excentricity of x-ray objects and cut applied. Data shown was recorded at grid voltage of 350 V.

The variables used in the likelihood ratio will presented in the following and the according distributions for x-ray and track reference will be shown. From the reconstructed track, the track length (figure 6.17), the number of pixels per tracklength (figure 6.18), the Kurtosis along the track direction (figure 6.19) and the eccentricity of the track (figure 6.20) are used. The direction of the reconstructed track is interpreted as the long axis in case of the eccentricity. From the reconstructed x-ray objects the Kurtosis along the long axis (figure 6.21) and the eccentricity (figure 6.22) are used. The resulting likelihood ratio distributions for x-ray and track reference data are shown in figure 6.23, a clear separation is obtained. The software efficiency can be calculated from the number of real x-ray events passing the discrimination algorithm. On a similar way the background rejection can be obtained from the number of non-x-ray events rejected by the algorithm. Using the x-ray and track reference data set respectively one can get the software efficiency as function of the cut value applied on $\log Q$ (see figure 6.24a) as well as the background rejection (6.24b). The visible separation in $\log Q$ (figure 6.23) in combination with the software efficiency and background rejection support the choice of the (intuitive) cut at $\log Q = 0$. Although, higher cut values could give benefit in terms of background rates.

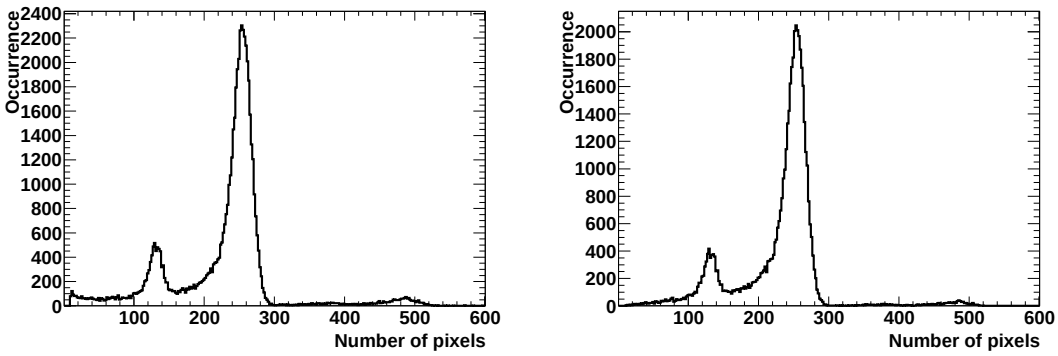

(a) (b)

Figure 6.15: Spectra of the ^{55}Fe source before (a) and after (b) the cuts. Data shown was recorded at grid voltage of 350 V.

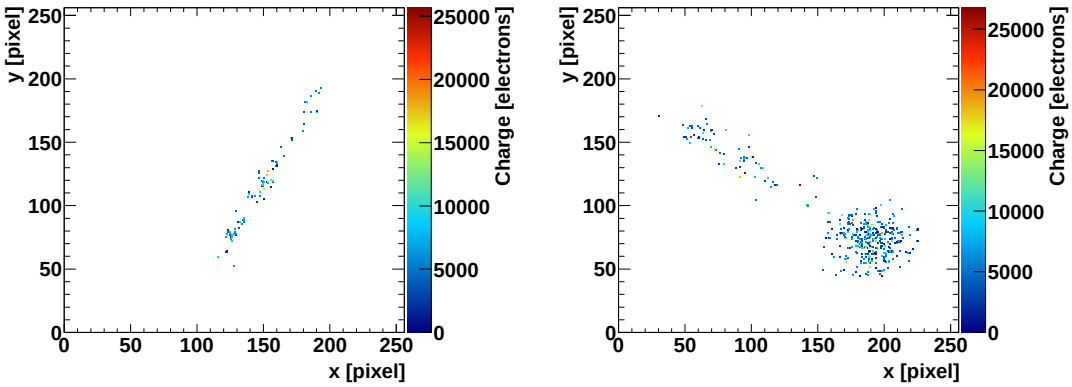

(a) (b)

Figure 6.16: Typical tracks observed in the detector. Events like (b) might mimic a x-ray object.

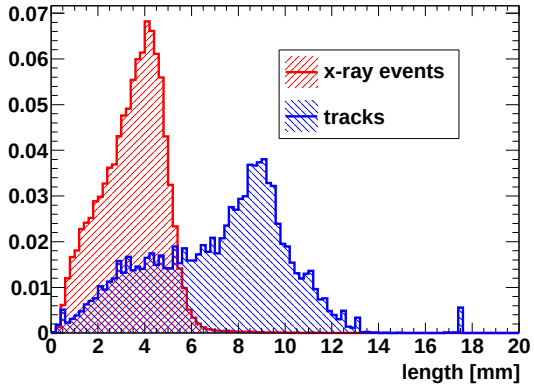

Figure 6.17: Length of reconstructed track. Distributions for reference data containing either x-ray events (red) or tracks (blue).

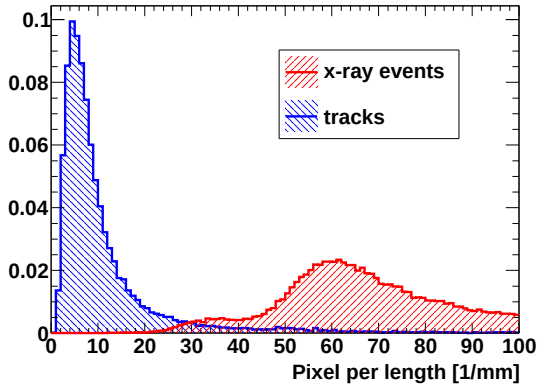

Figure 6.18: Number of pixel per track length. Distributions for reference data containing either x-ray events (red) or tracks (blue).

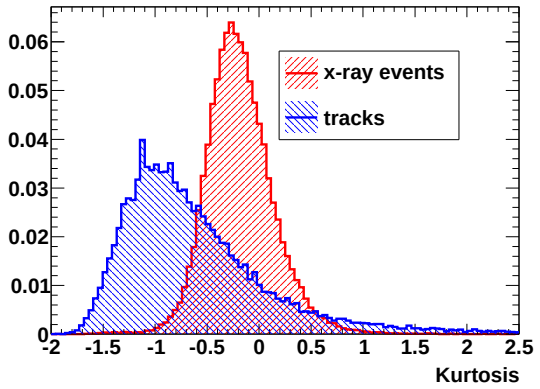

Figure 6.19: Kurtosis along the reconstructed track. Distributions for reference data containing either x-ray events (red) or tracks (blue).

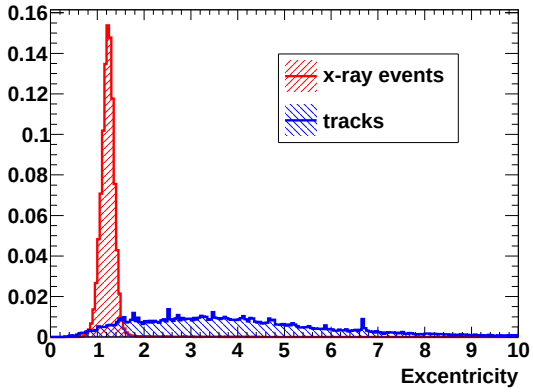

Figure 6.20: Excentricity of reconstructed track. Distributions for reference data containing either x-ray events (red) or tracks (blue).

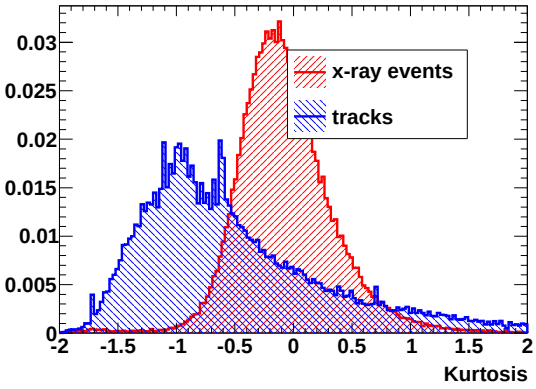

Figure 6.21: Kurtosis along short axis of reconstructed x-ray object. Distributions for reference data containing either x-ray events (red) or tracks (blue).

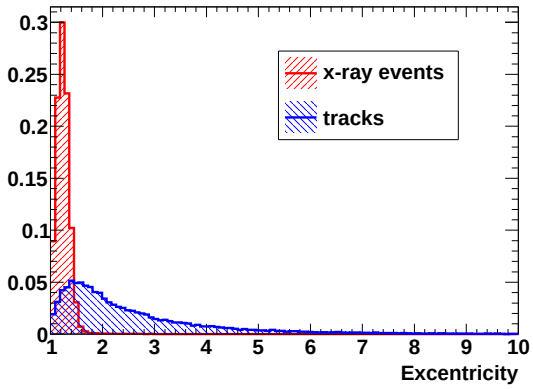

Figure 6.22: Excentricity of reconstructed x-ray object. Distributions for reference data containing either x-ray events (red) or tracks (blue).

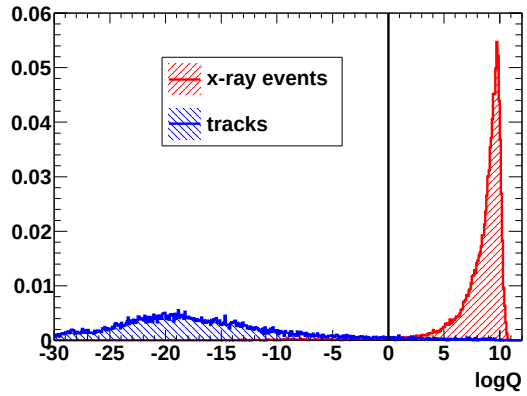

Figure 6.23: Logarithmic likelihood ratio $\log Q$. Distributions for reference data containing either x-ray events (red) or tracks (blue). Used cut value on $\log Q$ to discriminate between x-ray objects and tracks is indicated as black line.

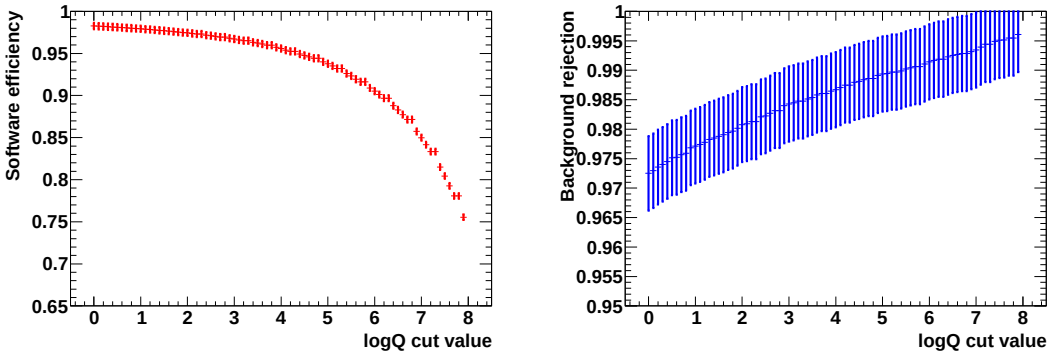

(a) (b)

Figure 6.24: Software efficiency (a) and background rejection (b) as function of the $\log Q$ cut value.

Chapter 7

Measurements & Results

The measurements performed will be presented in this chapter along with the results obtained. The characteristics of the detector were obtained from measurements with a ^{55}Fe source. Results concerning the energy resolution, efficiency and gas gain will be shown along with hints for distortions of the electric field in the detector. Some phenomena observed in the distributions of the charge per pixel which indicate charge sharing between pixels will be presented too. At last the results of the background measurements: background spectra and resulting background rates, will be shown.

7.1 Measurements with ^{55}Fe source

Measurements with a radioactive ^{55}Fe source were done to obtain the energy resolution of the detector, its gas gain and to get an energy calibration from the two lines of ^{55}Fe (5.9 keV and escape peak) which can be used for the background data taking. In order to enhance the energy resolution a chromium foil (75 µm thickness) was used to filter the K_β line of ^{55}Fe which else would widen the observed peak as it cannot be separated from the K_α line.

A photo of the whole measurement setup including data acquisition and controlling systems, power and high voltage supplies can be found in figure 7.1a. The detector was supplied with a gas mixture from premixed gas bottles (figure 7.1b). For all measurements a mixture of Argon and Isobutane was used, the fraction of Isobutane was 5% (Ar/iC_4H_{10} 95/5). This mixture was chosen for two reasons. The large diffusion coefficient of Ar/iC_4H_{10} 95/5 causes the charge clouds created by absorbed x-ray photons to widen during drift so that the individual electrons in the cloud can be observed. As Ar/iC_4H_{10} 95/5 is a Penning gas mixture it allows to achieve high gas gains at relatively low grid voltages. During all measurements the detector was flushed with $\sim 2\,^{l}/_{h}$. The gas pressure in the detector could not be controlled or measured. Operation was therefore done at approximately atmospheric pressure ($\sim 0.2 mbar$ overpressure with respect to the environment) with the gas outlet of the detector connected to a long tube with open end.

The measurements were done for different grid voltages. The grid voltage was raised in steps of 10 V beginning from 290 V up to 400 V. For all grid voltages a drift field of $225\,^{V}/_{cm}$ was applied. To reduce the number of events with two x-ray photons in them to a minimum an acquisition time (time during which the shutter of the Timepix is 'open') of 20 ms was chosen. For every grid voltage 15 000 to 20 000 x-ray events were recorded except for 350 V. For this voltage about 50 000 x-ray events were taken as this data set was used for the energy calibration of the background measurements and as reference data set for the background discrimination.

To reduce background rates during measurements the detector was shielded. Starting from the inside of the shielding, the detector was surrounded by a copper box of thickness 1 mm acting as Faraday cage which was flushed with pure nitrogen to reduce the Radon contamination of the direct detector environment. An outer shielding was done by burying the detector in a lead grave build from lead bricks (5 cm at sides and bottom and 10 cm on the top). The detector covered with lead can be seen in figure

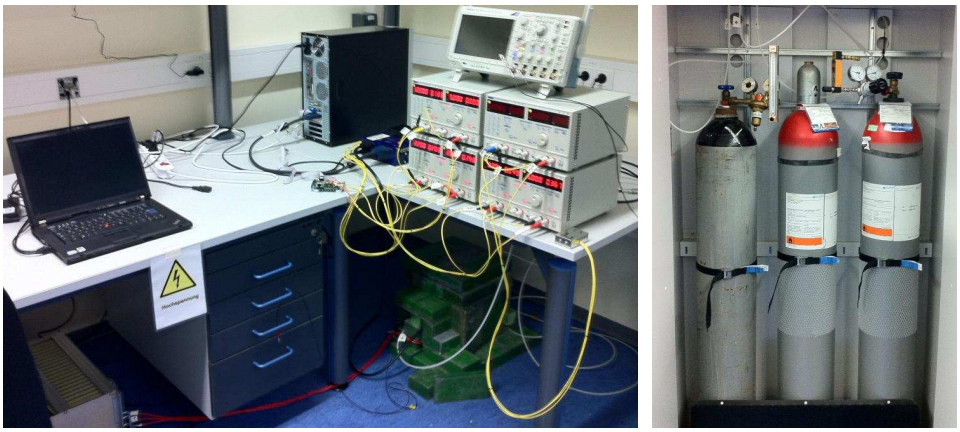

(a) (b)

Figure 7.1: Pictures showing the shielded detectors, its readout systems and supplies. In (a) one can see the computer and the MUROS used to readout the GridPix (in the middle), the laboratory power supplies delivering the power for the MUROS and the chip (on the right), the high voltage supply (down on the left) and the notebook used to control the high voltage. The shielded detector can be found below the table on the right. In (b) two premixed gas bottles (on the right) containing Ar/iC_4H_{10} 95/5 and the nitrogen bottle for flushing the shielding (on the left) are shown.

7.2a, a view into the partially opened shielding also showing the opened copper box can be found in figure 7.2b.

7.2 Energy resolution

After applying the cuts presented in the last chapter one can extract the energy resolution from either a histogram of the number of pixels (figure 7.3) or of the total charge in one x-ray object (figure 7.4). In both spectra the escape peak and photopeak of the ^{55}Fe source are clearly visible, also a small accumulation at twice the photopeak is visible. The latter is caused by events with two x-ray photons converted in one frame which are too close to be separated.

By fitting Gaussians with mean μ and width σ to the (top parts of the) peaks one can determine the energy resolution for energies of 2.7 keV and 5.9 keV

$$\left(\frac{\sigma}{\mu}\right)_{2.7\,\text{keV}} = (6.82 \pm 0.17)\% \tag{7.1}$$

$$\left(\frac{\sigma}{\mu}\right)_{5.9\,\text{keV}} = (4.95 \pm 0.04)\%. \tag{7.2}$$

The large tail to the left of the photopeak in figure 7.3 originates from charge clouds which have drifted only s short distance so that the single electrons cannot be separated due to lack of diffusion. Therefore, only for long drift distances the energy of a x-ray photon can be reconstructed by counting the pixels.

From the charge spectrum in figure 7.4 one can also determine an energy resolution. But the shape of the peaks in the charge spectrum is not completely Gaussian, the left side and the top part are described well by a Gaussian while to the right a tail appears. The energy resolution obtained from the Gaussian

(a) (b)

Figure 7.2: Pictures showing the detectors shielding. The detector fully shielded with lead bricks (a) and partially opened shielding (b). In (b) also the opened copper box with the connections for nitrogen flushing on the left can be seen as also the ^{55}Fe source mounted on the detector.

fits to parts of the peaks are

$$\left(\frac{\sigma}{\mu}\right)_{2.7\,\mathrm{keV}} = (9.36 \pm 0.19)\% \tag{7.3}$$

$$\left(\frac{\sigma}{\mu}\right)_{5.9\,\mathrm{keV}} = (6.17 \pm 0.04)\% \tag{7.4}$$

and, therefore, a bit worse than the energy resolutions in the pixel spectrum. The tails to the right of the peaks are probably caused by the Polya distribution of the gas gain which results in very high gas amplifications at a low amount of multiplied electrons. If more than one electron enters one grid hole all of them are multiplied so that although multiple electrons are detected as one pixel the charge accumulated on this pixel is the integrated charge created by all of them. Therefore, the charge information holds a valid energy information also for charge clouds with short drift distance.

7.3 Efficiency

In case of full single electron efficiency each electron arriving at the GridPix will undergo sufficient multiplication to be detected. This is possible for the gas gain being higher than a certain threshold value. So starting at low gas gains the single electron efficiency will rise up to a certain gas gain (or grid voltage) at which full efficiency is reached. A measure for the single electron efficiency is the number of electrons (or activated pixels in case of the GridPix) which is observed in the photopeak of the ^{55}Fe spectrum (see figure 7.3). The number of pixels can be obtained by fitting a Gaussian to the photopeak in the spectrum. The expected value for this number N is given by the photoelectrons energy divided by the mean ionization energy $w_{95/5}$ for the gas mixture

$$N = \frac{5.9\,\mathrm{keV}}{26\,\mathrm{eV}} \approx 230 \tag{7.5}$$

although the real number may deviate from this due to the Penning effect.

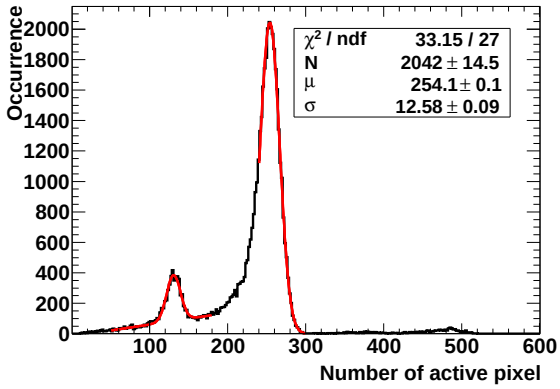

Figure 7.3: Spectrum of ^{55}Fe recorded at a grid voltage of 350 V. Number of active pixel is used as measure for the energy, Gaussian distributions fitted to the peaks are shown in red, stated fit parameters belong to the 5.9 keV peak. To the Gaussian fitted to the escape peak a linear function was added to describe the 'background' originating from not fully separated charge clouds.

In figure 7.5 the observed number of pixels in the photopeak is shown as function of the applied grid voltage. For low voltages ($\lesssim$ 350 V) the behavior is as expected, starting at low number and approaching a saturation value as the single electron efficiency rises with the gas gain. At voltages larger than 350 V however the number of pixels rises faster again ending at much to high numbers at 400 V. From figure 7.5 one can obtain that full singe electron efficiency is reached if 340 V to 350 V are applied at the grid for the GridPix.

A possible explanation for the excess of pixels (i.e. electrons) would be that for high gas gains the charge created in the gas amplification from one electron is not collected by only one pixel. If some fraction of the charge is collected on a neighboring pixel, this pixel could be activated, if the gas amplification is high enough that the amount of electrons is larger than the threshold of the pixels.

7.4 Gas gain

There are two ways for measuring the mean gas gain of the GridPix. One is to look at isolated pixels (pixels with no neighbors) and take the mean charge on these pixels. The charge per (isolated) pixel follows a Polya distribution (see figure 7.6) as the gas amplification does. Taking the mean of this distribution gives therefore the mean gas gain. Isolated pixels are chosen as they have a lower probability of more than one electron having entered the corresponding grid hole. The other method to obtain the gas gain is to take the amount of charge for the photopeak from the spectrum (figure 7.4) and divide it by the number of electrons observed in the peak (figure 7.3).

The gas gain obtained with both methods is shown as function of the grid voltage in figure 7.7. Since the number of pixels exceed the expected value by far (see section before) the observed number of electrons was replaced by the expected number (230) for voltages above 340 V. Both methods give very different gas gains for high voltages. The gas gain taken from the charge per pixel seems to underestimate the gas gain. This backs the assumption that for high gas amplifications charge is shared onto a neighboring pixel. Therefore, high gas amplifications could not result in isolated pixels. Isolated pixels could only occur for low gas amplifications so that the mean charge per isolated pixels takes into account gas amplifications up to some value. One can see that both methods approach each other for

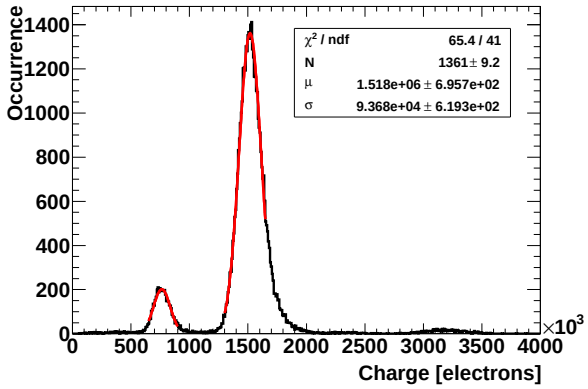

Figure 7.4: Spectrum of ^{55}Fe recorded at a grid voltage of 350 V. Total charge of reconstructed x-ray objects is used as measure for the energy, Gaussian distributions fitted to the peaks are shown in red, stated fit parameters belong to the 5.9 keV peak.

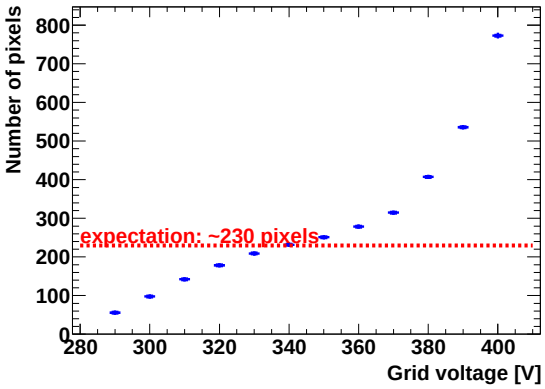

Figure 7.5: Number of pixel observed in the photopeak as function of the grid voltage. Expected number indicated in red.

low voltages which also backs the assumption of charge sharing as this would not occur for low voltages resulting in lower gas gains. Combining figure 7.5 with the gas gains from figure 7.7 one can conclude that full single electron efficiency is reached for gas gains $\gtrsim 5000$.

The rise of the gain with the voltage is roughly exponential as expected but an exponential function does not fit to the data points well. Probably this is due to change of environmental conditions (e.g. gas pressure or temperature) between the measurements for different voltages. Also the charge sharing might lower the measured gas gain for low voltages. If the charge shared onto a neighboring pixel is too low to activate the pixel it is lost. This would result in more charge not being detected for low gas gains as for high gas gains as for high gas gains the shared charge is larger and will, therefore, in more cases be sufficient to be detected on a pixel.

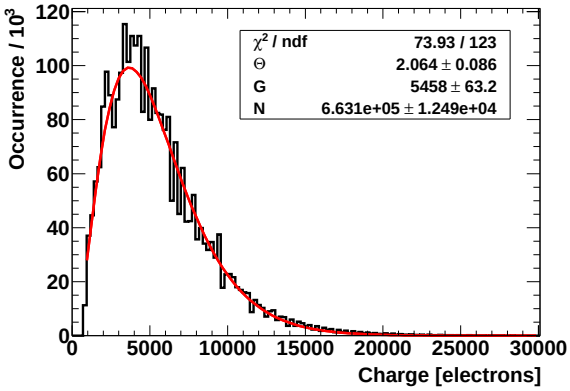

Figure 7.6: Charge per isolated pixel for grid voltage of 350 V. A Polya distribution (as parameterized in equation 3.52) is fitted to the distribution and gives a mean gas gain of ~ 5500.

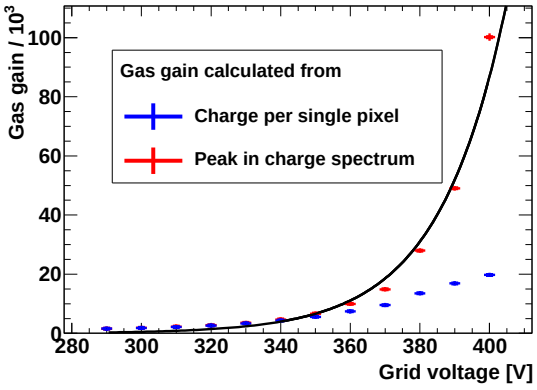

Figure 7.7: Gas gain as function of grid voltage. The gas gain was calculated on two ways: From the mean charge per pixel and from the 5.9 keV peak in the charge spectrum.

7.5 Charge sharing between pixels

To support the assumption of charged shared between neighboring pixels in case of high gas amplifications one can take a look at the charge per pixel. In figures 7.8 to 7.10 the charge per pixel is shown for grid voltages of 320 V, 350 V and 380 V. The distributions for the remaining voltages from 290 V to 400 V can be found in appendix B. In the histograms it is differentiated between all pixels, isolated pixels and pixels with exact one neighbor (more precise a neighbor with which one side is shared).

In case of no charge sharing the distributions for the three kind of pixels are expected to be almost the same, despite of effects of multiple electrons in one grid hole which more unlikely for isolated pixels than for those with many neighbors as the density of activated pixels in an area should be correlated with the electron density of the charge cloud in this region.

For low grid voltages the distributions match roughly as shown in figure 7.8 for a grid voltage of 320 V. For 350 V a small shoulder appears in the distribution of pixels with one neighbor for low charges (figure 7.9). Also the tails to the right of the distributions do not match anymore, for pixel with neighbors there is a surplus of high charges compared to isolated pixels. This behavior is expected in case of charge

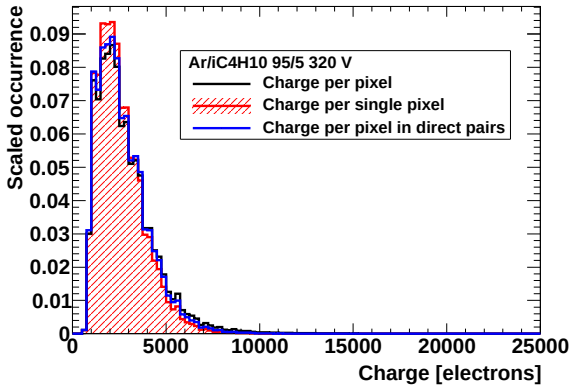

Figure 7.8: Charge per pixel at a grid voltage of 320 V. Three kinds of pixels were differentiated: all pixels, isolated pixels and pixels with exactly one neighbor. Histograms have been scaled to have an integrated area of 1.

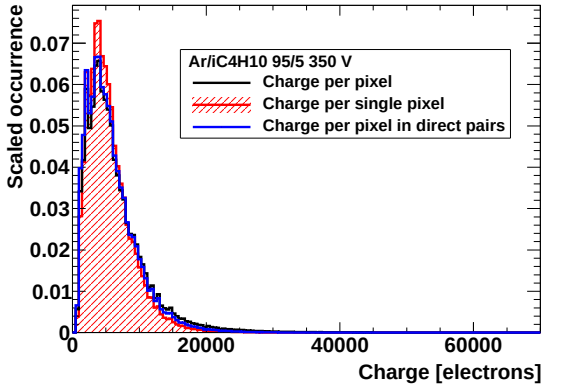

Figure 7.9: Charge per pixel at a grid voltage of 350 V. Three kinds of pixels were differentiated: all pixels, isolated pixels and pixels with exactly one neighbor. Histograms have been scaled to have an integrated area of 1.

sharing, the shoulder is due to pixels which only measure charge shared from their neighbor (which is of course a small fraction of the charge the neighbor collects). This increases the number of pixels measuring low charges with respect to the number one would expect from the distribution of the gas gain. In case of isolated pixels no charge is shared or the charge transferred to a neighboring pixel is too low to activate it. The surplus of pixels seeing high charges in case of non-isolated pixels might have two reasons. If two neighboring pixels are hit the charge normally cut off is transferred to the other pixel and therefore increases the charge. The other reason might be that if for a gas amplification larger than a certain value always neighboring pixels are activated by the charge shared, there will be no isolated pixels with charges corresponding to this gas amplifications. As the mentioned effects only appear slightly for 350 V going to even higher voltages they become more and more visible. For 380 V the shoulder at low charges as well as the lack of isolated pixels with high charges get very pronounced as one can see in figure 7.10.

Assuming a simple model for the distribution of the electrons in the avalanche created in the gas amplification stage one can compute what fraction of charge is transferred on a neighboring pixel. In the following it is assumed that the distribution of electrons in the avalanche can be described by diffusion

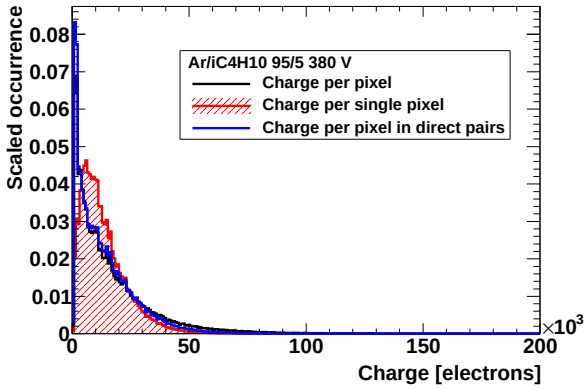

Figure 7.10: Charge per pixel at a grid voltage of 380 V. Three kinds of pixels were differentiated: all pixels, isolated pixels and pixels with exactly one neighbor. Histograms have been scaled to have an integrated area of 1.

Grid voltage in V	$D_t[\mu m/\sqrt{cm}]$	$\sigma[\mu m]$	Shared fraction[%]	Gas amplification
290	154.588	10.93	0.589	135 916
300	151.575	10.72	0.513	155 885
310	148.104	10.47	0.428	186 829
320	147.828	10.45	0.422	189 573
330	141.648	10.01	0.300	266 400
340	143.281	10.13	0.328	244 126
350	140.186	9.91	0.273	293 363
360	136.374	9.64	0.217	368 664
370	135.457	9.58	0.204	393 120
380	135.063	9.55	0.198	404 449
390	133.905	9.47	0.183	437 876
400	130.897	9.26	0.146	547 196

Table 7.1: Charge fractions transferred by diffusion on neighboring pixel for different grid voltages, diffusion coefficients D_t calculated with `Magboltz`, amplification gap of 50 µm assumed for calculation of σ. Stated gas amplification is gas amplification necessary to get 800 e on neighboring pixel.

during the avalanches propagation in the amplification gap. Therefore, for the distribution on the readout plane a two dimensional Gaussian is assumed. The area from which charge is collected into one pixel is assumed to be of quadratic shape with 55 µm side length. In table 7.1 the fraction collected on one neighboring pixel is calculated. The diffusion coefficients for different grid voltages were calculated with `Magboltz`. The gas amplification stated in table 7.1 is the gas amplification necessary to achieve 800 e on the neighboring pixel so that it is activated. The avalanche is assumed to start in the center of a grid hole.

Comparing this results with mean gas gains in figure 7.7 it is still not very likely even for high grid voltages to activate neighboring pixels. But in table 7.1 the avalanche was always assumed to start in the hole center. For a displaced avalanche the charge fractions on a neighboring pixel are listed in table 7.2. As the grid hole diameter is 30 µm the displacement from the center can be up to 15 µm. By taking into account the displacement activating a neighboring becomes quite likely for high gas gains so that the assumption of charge sharing can be motivated by diffusion in the gas amplification region. Of course,

Displacement in μm	Shared fraction[%]	Gas amplification
0.0	0.27	293 363
2.5	0.58	137 339
5.0	1.16	69 252
7.5	2.17	36 804
10.0	3.87	20 696
12.5	6.53	12 252
15.0	10.36	7725

Table 7.2: Charge fractions transferred by diffusion on neighboring pixel for different displacements from the center, diffusion coefficient for 350 V grid voltage was used, therefore $\sigma = 9.91\,\mu\text{m}$. Stated gas amplification is gas amplification necessary to get 800 e on neighboring pixel.

this simple approach cannot explain the extensive surplus of observed pixels for very high gains (figure 7.5). Probably also the resistive protection layer has to be taken into account. This layer spreads large amounts of charge arriving on the surface over a larger area as it is supposed to do in case of discharges.

7.6 Hints for distortions of the electric field

The differences between measured and simulated x-ray events in eccentricity and distribution of the rotation angle φ as shown in figure 6.8 the chapter before give hints that field distortions in the detector change the shape of the events and give a preferred direction. The causes for this field distortions were already discussed along with possible solutions in chapter 5. To be able to conclude that these changes in shape arise from the influence of field distortions one can take a look at some scatter plots.

In figure 7.11 the width σ_y of the x-ray objects along their short axis is plotted versus the observed rotation angle φ. As the width along the short axis is caused by diffusion it is correlated with distance z the charge cloud has drifted

$$\sigma_y = D_\text{t} \sqrt{z} \tag{7.6}$$

one can see that the preferred direction shows up mainly for x-ray objects which have drifted a long distance. This would back the assumption of the field distortions as their influence is larger the longer the charge clouds are exposed to the distortions.

In figure 7.12 the width σ_y of the x-ray objects along their short axis is plotted versus the observed eccentricity. Larger eccentricity appear for larger widths and therefore larger drift distances. This is counterfeiting the expectation as one would expect the eccentricity to be lower for large drift distance as the natural eccentricity is washed by diffusion which increases with the drift distance. The observed behavior could be explained with the influence of field distortions.

Although the field distortions change the events shape their influence on the analysis is not large. In figure 7.13 ellipses for different eccentricities are drawn. One can see that the difference between an eccentricity of 1.25 (as observed in the measurements) and an eccentricity of 1.1 (as observed for the artificial x-ray events) is rather small, although it is visible.

7.7 Background measurements

To measure the background rates of the detector, large data sets were taken with acquisition times of 1 s. Background data was taken for different shielding setups:

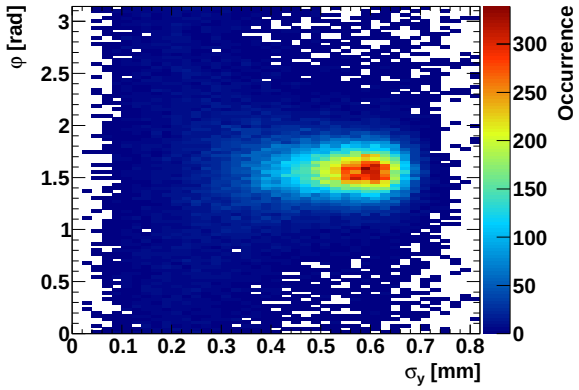

Figure 7.11: Width σ_y along short axis versus rotation angle φ. Those x-ray objects which show a preferred direction are those with largest σ_y and therefore those with the longest drift distance.

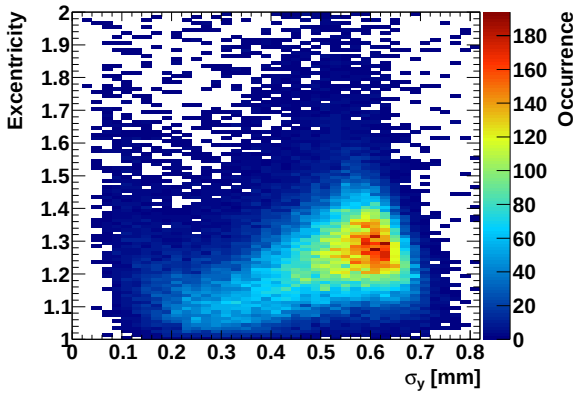

Figure 7.12: Width σ_y along short axis versus eccentricity. The x-ray objects which have the largest eccentricity are those with largest σ_y and therefore those with the longest drift distance.

- No shielding
- Only copper box
- Copper box flushed with nitrogen
- Full shielding including 5 to 10 cm lead shielding

For each setup about 500 000 events were recorded corresponding to one week of data taking for each shielding setup. For the background measurements the detector was operated at a grid voltage of 350 V with again Ar/iC_4H_{10} 95/5.

7.8 Background rates

For the four different shielding setups the background data was cleaned with the background discrimination algorithm described in chapter 6. The results of the discrimination are listed in table 7.3. N_{total}

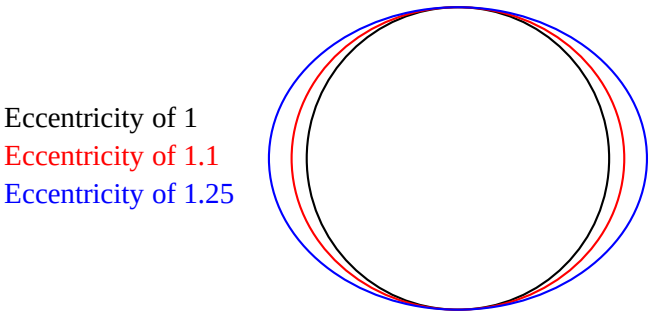

Figure 7.13: Ellipses with different eccentricities.

is the number of frames recorded, $N_{\text{non-empty}}$ the number of frames which have at least one hit pixel in the active area, $N_{\text{x-ray}}$ the number of x-ray events which passed the discrimination and N_{window} the number of x-ray events which passed the discrimination and are located in the area assigned to the x-ray window. To convert the charge information of the remaining x-ray objects into an energy information the results of the runs with radioactive source were used. Gaussian distributions were fitted to the top parts of the two peaks of the charge spectrum in figure 7.4 giving

$$E = 5.9\,\text{keV} \rightarrow Q = 1.518 \times 10^6\,e \pm 6.957 \times 10^2\,e \tag{7.7}$$

$$E = 2.7\,\text{keV} \rightarrow Q = 7.641 \times 10^5\,e \pm 1.267 \times 10^3\,e \tag{7.8}$$

which could be used for an extrapolation line

$$E = -5.433 \times 10^{-1}\,\text{keV} + 4.245 \times 10^{-6}\,\text{keV} \cdot Q[e]. \tag{7.9}$$

Shielding setup	N_{total}	$N_{\text{non-empty}}$	$N_{\text{x-ray}}$	N_{window}
no shielding	496 279	54 636	1440	124
copper box	532 388	74 042	1656	135
copper box flushed with nitrogen	500 124	56 035	1563	119
full shielding	520 995	37 109	710	59

Table 7.3: Overview of the background data taking. N_{total} is the number of frames recorded for one shielding setup, $N_{\text{non-empty}}$ the number of non-empty frames, $N_{\text{x-ray}}$ the number of x-ray objects passing the discrimination and N_{window} the number of x-ray objects which passed the discrimination and are located in the area assigned to the x-ray window.

Applying this energy calibration to the x-ray objects remaining after the background discrimination one obtains the background spectra shown in figures 7.14 to 7.17. In the spectra no peak is visible which could be assigned to fluorescence lines but for low energies up to $\sim 3\,\text{keV}$ the number of x-ray objects seems to be rather large. Reasons for this might be the fluorescence line of aluminium although no clear peak for this line is visible, also the efficiency of the background discrimination at those low energies is unknown as the reference data set only has photon energies of 2.7 keV and 5.9 keV.

Of course the energy calibration is not of high quality as due to lack of a pressure control it is very likely that the gas gain has changed during measurements which would lead to different energy charge relations. Also only two points were available for the calibration allowing just a linear extrapolation. It would be desirable to have more reference points between 1 keV and 10 keV to improve the calibration.

To calculate the background rates from the energy spectra one has to divide the number of entries

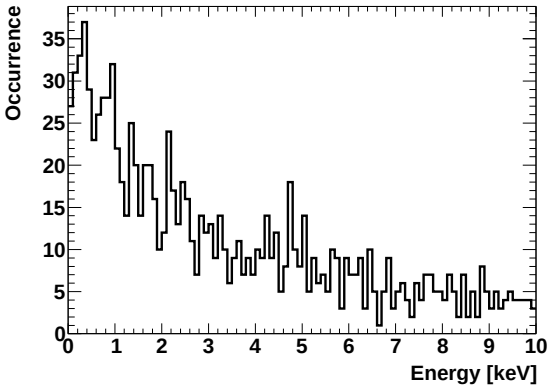

Figure 7.14: Background spectrum recorded without any shielding.

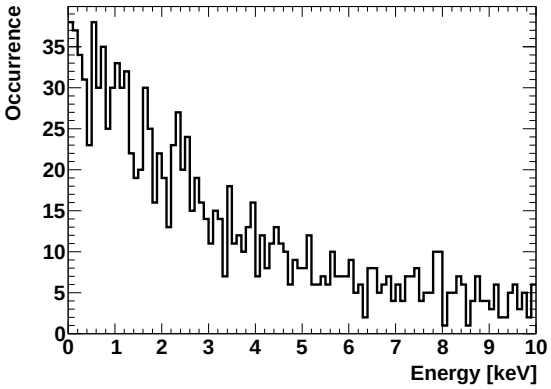

Figure 7.15: Background spectrum recorded with copper box as Faraday cage.

in the energy bins by the total measurement time, the energy bin width and the total active area of the detector. The measurement time is given by the total number of frames recorded for one shielding setup times 1 s as each frame was 1 s long. For the area the walls supporting the InGrid structure have to be considered as they reduce the active area. The walls are 500 µm thick, thus giving an active area of $A = 1.3 \times 1.3\,\mathrm{cm}^2 = 1.69\,\mathrm{cm}^2$. The resulting background rates are shown in figure 7.18 for all four shielding setups, 1 keV bins were used. One can see that the rates are almost the same for all setups except the lead shielding which reduces the rate by a factor of about 3.

The fact that only the lead shielding shows visible influence on the background rates can be explained by the assumption that at the reached background level the background is dominated by (parts of) charged particles tracks misinterpreted as x-ray events because charged particles entering at a very large angle will pass through the cathode and the grid. Due to diffusion such events look quite similar to a real x-ray event. If a certain fraction of these events passes the background discrimination, a reduction of the total number of charged particles tracks (as caused by the lead shielding) would result in a reduction of the number of misidentified events and, therefore, in a reduction of the background rates. Looking at a map (figure 7.19) showing the positions of the reconstructed x-ray objects in case of the full shielding one can see that they are almost uniformly distributed over the central region of

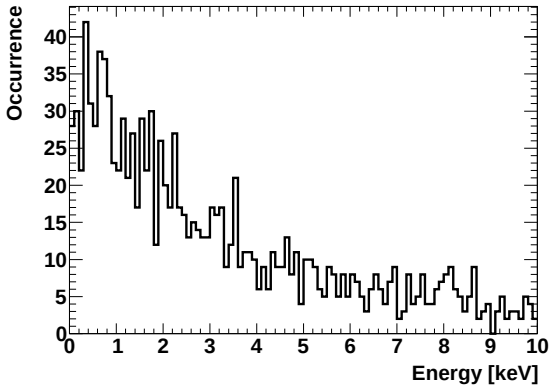

Figure 7.16: Background spectrum recorded with copper box flushed with nitrogen.

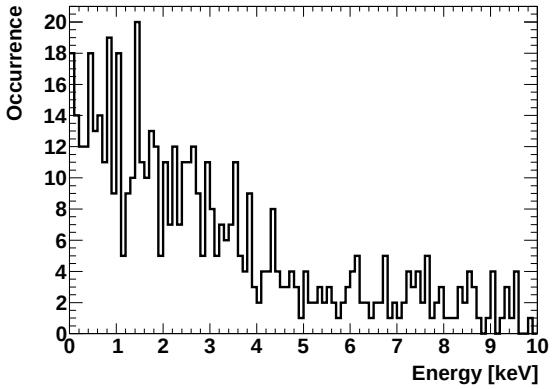

Figure 7.17: Background spectrum recorded with full shielding including copper box flushed with nitrogen and lead shielding.

the GridPix, although it seems as if there are a bit less events in the very central region. There are no hot spots visible except one in the upper left which is probably caused by discharges at the edge. The lack of events at the sides is due to the inactive regions covered by the walls supporting the grid. The accumulation of events at the edges of the active region are probably caused by the distortions of the electric field which have much more influence near to the chips sides than in the central region.

In figure 7.20 two background events are shown which pass the discrimination clearly ($\log Q > 7$) and are therefore most likely (compare figure 6.23) real x-ray events. Background events only barely passing the discrimination ($\log Q < 1$) are shown in figure 7.21. The latter ones might most likely be no real x-ray events but still pass the (intuitive) cut on $\log Q$.

Looking at the number of events passing the background discrimination which also are in the area assigned to the x-ray window given in table 7.3 one can see that these roughly correspond to the total number of events passing the discrimination scaled with the ratio of the areas considered. In case of events assigned to the x-ray window the considered area is a circle with 2 mm radius.

Comparing the background rates with the rates reached with the MicroBulk-Micromegas used at CAST [34, 33] the rates achieved in this thesis are roughly a factor 50 higher than those of the MicroBulk-Micromegas. And of course in the low energy regime (where MicroBulk-Micromegas are not sensitive)

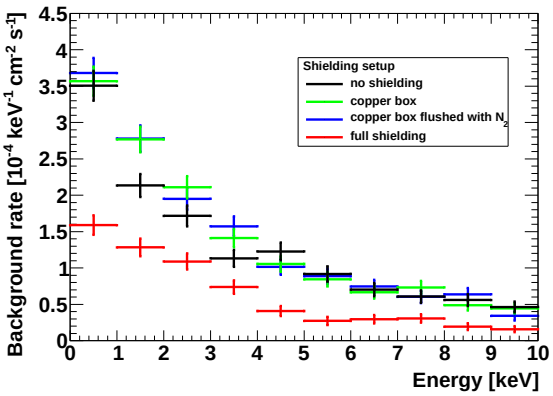

Figure 7.18: Background rates for different shielding setups.

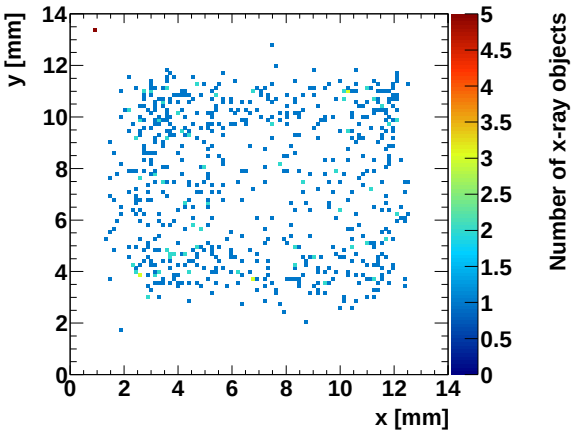

Figure 7.19: Distribution of background x-ray events which passed the discrimination. Full shielding was used.

the rates are much too high. But it should be possible to improve the detector and the analysis to be able to compete with the CAST detectors. Improvements could be a further event shape analysis or the employment of a neural network for background discrimination. Of course also decoupling the signal from the grid should deliver significant benefit for background discrimination by use of the time information of the signal including its shape.

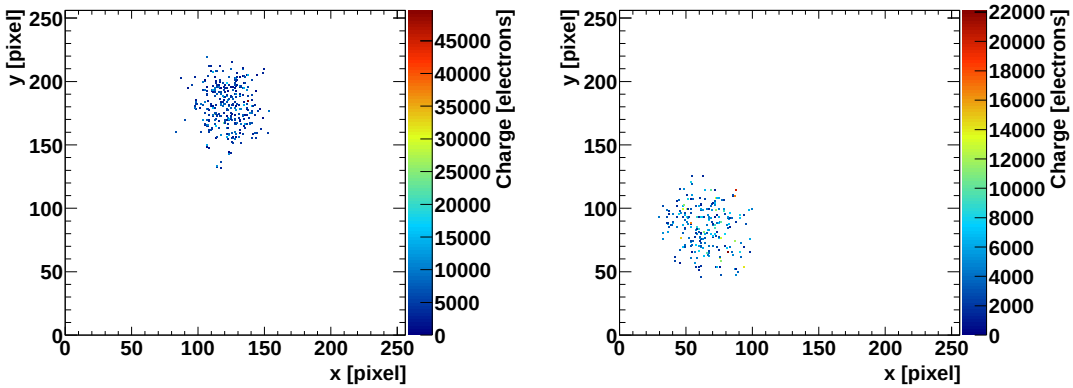

(a) (b)

Figure 7.20: Background events clearly passing the discrimination: $\log Q = 7.806$ (a) and $\log Q = 9.244$ (b).

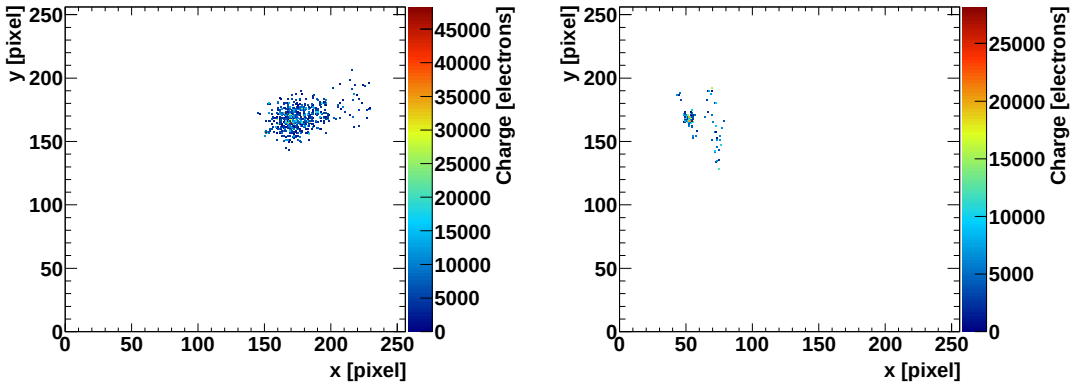

(a) (b)

Figure 7.21: Background events barely passing the discrimination: $\log Q = 0.137$ (a) and $\log Q = 0.056$ (b).

Chapter 8

Conclusion & Outlook

A GridPix based x-ray detector was successfully designed, constructed and commissioned. The detector and especially the GridPix worked for more than three months of data taking and are still operational. Stable operation and data taking was possible at a gas gain of $\sim$ 6600 where single electron efficiency was reached. Furthermore, the InGrid structure of the GridPix could be operated at gas gains up to approximately 100 000. The detector has shown good performance. The detector's characteristics, e.g. gas gain and efficiency, were determined with a ^{55}Fe source. The spectra showed an energy resolution of 5% (respectively 6.2% in the charge spectrum) at 5.9 keV underlining the detector performance.

The background rates reached with the detector in combination with the likelihood ratio based background discrimination are already promising, especially considering that this was a first study for a low background detector based on a GridPix gas amplification and readout structure. As the background rates achieved in the region of x-ray energies between 3 keV and 10 keV are in the order of $5 \times 10^{-5}\,\mathrm{keV}^{-1}\,\mathrm{cm}^{-2}\,\mathrm{s}^{-1}$ the improvement necessary to compete with CAST detectors are likely to be reached by a modified version of the current detector. As discussed in the thesis, several ideas are already available. In addition to this the x-ray detector is in principle sensitive in an energy range below 2 keV where the CAST MicroBulk Micromegas are not sensitive due to their energy threshold caused by noise.

To reach lower background rates the detector will be improved in near future. These improvements will mainly concern the implementation of the GridPix in the readout plane, proper grounding and electromagnetic shielding. Additionally the grid signal will be decoupled and sampled to gain information of the time development. This can be used to discriminate the background further. Of course, using the grid signal will improve also the energy resolution. A test of the detector with Xenon based gas mixtures will be possible at CERN soon. Also, some aspects of the detector (e.g. the observed effect of charge sharing) will be studied in more detail. To further improve the background discrimination the use of a neural network will be considered.

Summing up, the proof of principle for a GridPix based low background x-ray detector is done and it should be possible to reach with some improvements background rates low enough. So, that a GridPix based x-ray detector will become a future CAST detector.

Appendix A

List of measurements

The complete list of all measurements are in tables A.1 and A.2.

run name	run number	abort	U_{grid}[V]	U_{anode}[V]	U_{cathode}[V]	gas flux [l/h]	T_{acq}[s]	shielding	comments	T_{total}[s]	N_{frames}	$N_{\text{non-empty}}$
150711_01	0		350	350	800	3.0	1.0	none		260 429	197 322	22 744
180711_01	1		350	350	800	3.0	1.0	none		143 341	122 474	13 949
200711_01	2		350	350	800	3.0	1.0	none		188 804	188 804	17 543
220711_01	3		350	350	800	2.0	0.02	full shielding	^{55}Fe source	57 600	186 682	15 010
230711_01	4		350	350	800	2.0	0.02	full shielding	^{55}Fe source	47 589	171 339	13 753
240711_01	5		350	350	800	2.0	0.02	full shielding	^{55}Fe source	37 897	151 183	12 216
240711_02	6		350	350	800	2.0	0.02	full shielding	^{55}Fe source	39 712	158 433	12 694
240711_03	7	gas bottle change	350	350	800	2.0	0.02	full shielding	^{55}Fe source	37 011	155 137	12 367
270711_01	8		350	350	800	2.0	1.0	full shielding		10 753	10 000	891
1 270711_02	9		350	350	800	2.0	1.0	full shielding		140 766	122 182	8908
290711_01	10		350	350	800	2.0	1.0	full shielding		185 304	154 478	11 188
310711_01	11		350	350	800	2.0	1.0	full shielding		169 863	143 971	9827
020811_01	12		350	350	800	2.0	1.0	full shielding		102 519	90 364	6295
030811_01	13		340	340	790	2.0	0.02	full shielding	^{55}Fe source	46 407	169 226	13 343
040811_01	14		340	340	790	2.0	0.02	full shielding	^{55}Fe source	12 920	65 997	5172
040811_oldPM	15		350	350	800	2.0	0.02	full shielding	^{55}Fe source, Pixelman 1.7.2	1411	10 000	1180
040811_02	16		340	340	790	2.0	0.02	full shielding	^{55}Fe source	11 189	71 587	5526
040811_03	17		330	330	780	2.0	0.02	full shielding	^{55}Fe source	10 185	66 363	5125
040811_04	18		330	330	780	2.0	0.02	full shielding	^{55}Fe source	10 631	67 524	5234
050811_01	19		330	330	780	2.0	0.02	full shielding	^{55}Fe source	10 198	65 645	5193
050811_02	20		330	330	780	2.0	0.02	full shielding	^{55}Fe source	10 361	66 324	5132
050811_03	21		330	330	780	2.0	0.02	full shielding	^{55}Fe source	5583	40 001	3130
050811_04	22		320	320	770	2.0	0.02	full shielding	^{55}Fe source	17 503	91 582	7135
050811_05	23		320	320	770	2.0	0.02	full shielding	^{55}Fe source	44 981	158 496	12 327
060811_01	24		320	320	770	2.0	0.02	full shielding	^{55}Fe source	13 137	74 347	5826
060811_02	25		310	310	760	2.0	0.02	full shielding	^{55}Fe source	8065	58 044	4507
060811_03	26		310	310	760	2.0	0.02	full shielding	^{55}Fe source	14 724	74 028	5740
060811_04	27		310	310	760	2.0	0.02	full shielding	^{55}Fe source	47 179	162 375	12 679
070811_01	28	bluescreen	300	300	750	2.0	0.02	full shielding	^{55}Fe source	11 668	66 256	5240
070811_02	29		300	300	750	2.0	0.02	full shielding	^{55}Fe source	8679	60 909	4782
070811_03	30		300	300	750	2.0	0.02	full shielding	^{55}Fe source	14 906	85 015	6431
070811_04	31		300	300	750	2.0	0.02	full shielding	^{55}Fe source	8596	60 123	4604
070811_05	32		290	290	740	2.0	0.02	full shielding	^{55}Fe source	26 322	108 477	8402
080811_01	33	gas bottle change	290	290	740	2.0	0.02	full shielding	^{55}Fe source	4377	29 949	2336
080811_02	34	full disk	290	290	740	2.0	0.02	full shielding	^{55}Fe source	10 322	61 434	4646
080811_03	35		290	290	740	2.0	0.02	full shielding	^{55}Fe source	14 790	68 574	5302
090811_01	36		350	350	800	2.0	0.02	full shielding	^{55}Fe source	31 051	142 046	11 057
150811_01	38	calibration	350	350	800	2.0	1.0	cu-box + N_2		65 960	60 141	6983
160811_01	39		350	350	800	2.0	1.0	cu-box + N_2		144 217	125 049	13 908
180811_01	40	N_2 bottle change	350	350	800	2.0	1.0	cu-box + N_2		108 094	94 077	10 495
190811_01	41		350	350	800	2.0	1.0	cu-box + N_2		165 295	139 806	15 536
210811_01	42		350	350	800	2.0	1.0	cu-box + N_2		91 355	81 051	9113

Table A.1: List of measurements 1/2. For all measurements Ar/iC_4H_{10} 95/5 was used. U_{grid}, U_{anode} and U_{cathode} denote the voltages applied at the grid, anode and cathode respectively. T_{total} is the total measurement time for one run including dead times due to readout. N_{frames} is the number of frames recorded in one run and $N_{\text{non-empty}}$ the number of frames with at least one pixel hit in the active area.

run name	run number	abort	U_{grid}[V]	U_{anode}[V]	$U_{cathode}$[V]	gas flux [l/h]	T_{acq}[s]	shielding	comments	T_{total}[s]	N_{frames}	$N_{non\text{-}empty}$
220811_01	43	gas bottle change	350	350	800	2.0	1.0	cu-box		87 757	78 231	8708
230811_01	44		350	350	800	2.0	1.0	cu-box		246 399	191 204	20 936
260811_01	45		350	350	800	2.0	1.0	cu-box		262 374	199 452	21 807
290811_01	46		350	350	800	2.0	1.0	cu-box		69 916	63 501	6887
300811_01	47		350	350	800	2.0	1.0	none		167 302	142 748	15 704
010911_01	48		350	350	800	2.0	1.0	none		116 602	101 028	11 036
020911_01	49	gas bottle change	350	350	800	2.0	1.0	none		71 397	64 816	7254
030911_01	50		350	350	800	2.0	1.0	none		157 366	134 415	14 854
050911_01	51		350	350	800	2.0	1.0	none		57 981	53 272	5788
060911_01	52	readout error	350	350	800	2.0	0.02	full shielding	^{55}Fe source + Cr foil	5480	46 743	4546
060911_02	53		350	350	800	2.0	0.02	full shielding	^{55}Fe source + Cr foil	24 060	121 189	11 861
070911_02	54		350	350	800	2.0	0.02	full shielding	^{55}Fe source + Cr foil	9909	66 483	6618
070911_03	56	bluescreen	350	350	800	2.0	0.02	full shielding	^{55}Fe source + Cr foil	9616	66 955	6526
080911_01	57	bluescreen	350	350	800	2.0	0.02	full shielding	^{55}Fe source + Cr foil	8274	59 810	5832
080911_02	58		350	350	800	2.0	0.02	full shielding	^{55}Fe source + Cr foil	8615	63 088	6064
080911_03	59		290	290	740	2.0	0.02	full shielding	^{55}Fe source + Cr foil	10 376	70 343	6788
080911_04	60		290	290	740	2.0	0.02	full shielding	^{55}Fe source + Cr foil	10 598	72 254	6974
080911_05	61		290	290	740	2.0	0.02	full shielding	^{55}Fe source + Cr foil	3261	30 025	2924
080911_06	62		300	300	750	2.0	0.02	full shielding	^{55}Fe source + Cr foil	35 600	153 053	14 371
090911_01	63		300	300	750	2.0	0.02	full shielding	^{55}Fe source + Cr foil	3848	35 120	3399
090911_02	64		310	310	760	2.0	0.02	full shielding	^{55}Fe source + Cr foil	14 420	80 141	7909
090911_03	65		310	310	760	2.0	0.02	full shielding	^{55}Fe source + Cr foil	5971	50 073	4953
090911_04	66		310	310	760	2.0	0.02	full shielding	^{55}Fe source + Cr foil	4730	41 744	4026
090911_05	67		320	320	770	2.0	0.02	full shielding	^{55}Fe source + Cr foil	57 241	184 722	17 895
100911_01	68		330	330	780	2.0	0.02	full shielding	^{55}Fe source + Cr foil	57 241	167 344	16 141
100911_02	69		340	340	790	2.0	0.02	full shielding	^{55}Fe source + Cr foil	49 699	176 494	17 035
110911_01	70		360	360	810	2.0	0.02	full shielding	^{55}Fe source + Cr foil	79 105	211 291	20 611
120911_01	71	full disk	370	370	820	2.0	0.02	full shielding	^{55}Fe source + Cr foil	3520	25 240	2451
120911_02	72		370	370	820	2.0	0.02	full shielding	^{55}Fe source + Cr foil	8419	63 669	6199
120911_03	73		370	370	820	2.0	0.02	full shielding	^{55}Fe source + Cr foil	7824	60 523	5907
120911_04	74		370	370	820	2.0	0.02	full shielding	^{55}Fe source + Cr foil	4481	40 070	3886
120911_05	75	readout error	380	380	830	2.0	0.02	full shielding	^{55}Fe source + Cr foil	652	5620	581
130911_01	76		380	380	830	2.0	0.02	full shielding	^{55}Fe source + Cr foil	7738	60 017	5863
130911_02	77		380	380	830	2.0	0.02	full shielding	^{55}Fe source + Cr foil	8850	65 761	6518
130911_03	78		380	380	830	2.0	0.02	full shielding	^{55}Fe source + Cr foil	5153	45 017	4565
130911_04	79		390	390	840	2.0	0.02	full shielding	^{55}Fe source + Cr foil	8438	60 565	6190
130911_05	80		390	390	840	2.0	0.02	full shielding	^{55}Fe source + Cr foil	8381	63 393	6703
130911_06	81		390	390	840	2.0	0.02	full shielding	^{55}Fe source + Cr foil	44 454	167 573	17 888
140911_01	82	gas bottle change	400	400	850	2.0	0.02	full shielding	^{55}Fe source + Cr foil	4213	38 861	4311
140911_02	83	readout error	400	400	850	2.0	0.02	full shielding	^{55}Fe source + Cr foil	1700	13 408	1387
140911_03	84	readout error	400	400	850	2.0	0.02	full shielding	^{55}Fe source + Cr foil	1311	10 928	1132
140911_04	85		400	400	850	2.0	0.02	full shielding	^{55}Fe source + Cr foil	8907	65 585	7281
140911_05	86	readout error	400	400	850	2.0	0.02	full shielding	^{55}Fe source + Cr foil	1782	16 140	1741
140911_06	87		400	400	850	2.0	0.02	full shielding	^{55}Fe source + Cr foil	3391	30 480	3217

Table A.2: List of measurements 2/2. For all measurements Ar/iC$_4$H$_{10}$ 95/5 was used. U_{grid}, U_{anode} and $U_{cathode}$ denote the voltages applied at the grid, anode and cathode respectively. T_{total} is the total measurement time for one run including dead times due to readout. N_{frames} is the number of frames recorded in one run and $N_{non\text{-}empty}$ the number of frames with at least one pixel hit in the active area.

Appendix B

Charge per pixel

The histograms of the charge per pixel for the voltages not shown in chapter 7 are presented in the following. The grid voltages were 290 V (figure B.1), 300 V (figure B.2), 310 V (figure B.3), 330 V (figure B.4), 340 V (figure B.5), 360 V (figure B.6), 370 V (figure B.7), 390 V (figure B.8) and 400 V (figure B.9). The development of the shoulder at low charges for pixels with neighbor with rising grid voltage (or with rising gas gain) is clearly visible.

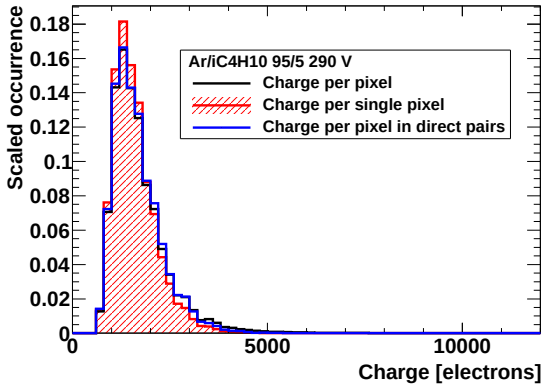

Figure B.1: Charge per pixel at a grid voltage of 290 V. Three kinds of pixels were differentiated: all pixels, isolated pixels and pixels with exactly one neighbor. Histograms have been scaled to have an integrated area of 1.

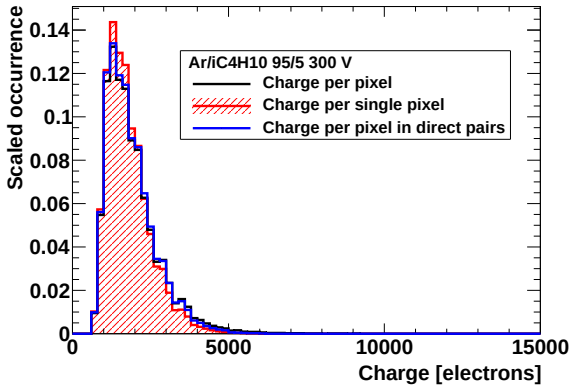

Figure B.2: Charge per pixel at a grid voltage of 300 V. Three kinds of pixels were differentiated: all pixels, isolated pixels and pixels with exactly one neighbor. Histograms have been scaled to have an integrated area of 1.

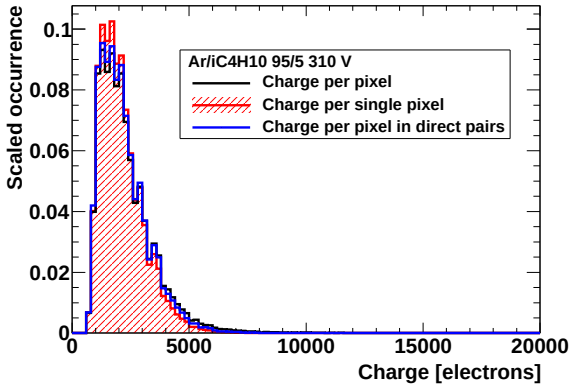

Figure B.3: Charge per pixel at a grid voltage of 310 V. Three kinds of pixels were differentiated: all pixels, isolated pixels and pixels with exactly one neighbor. Histograms have been scaled to have an integrated area of 1.

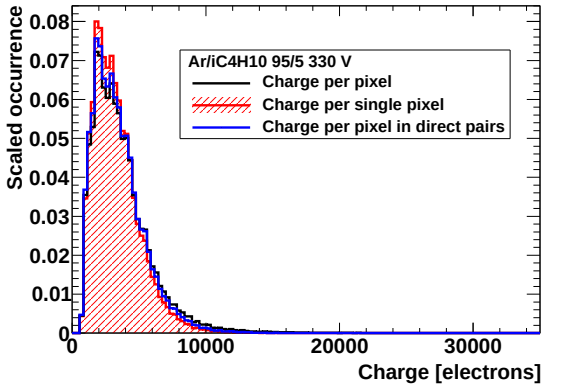

Figure B.4: Charge per pixel at a grid voltage of 330 V. Three kinds of pixels were differentiated: all pixels, isolated pixels and pixels with exactly one neighbor. Histograms have been scaled to have an integrated area of 1.

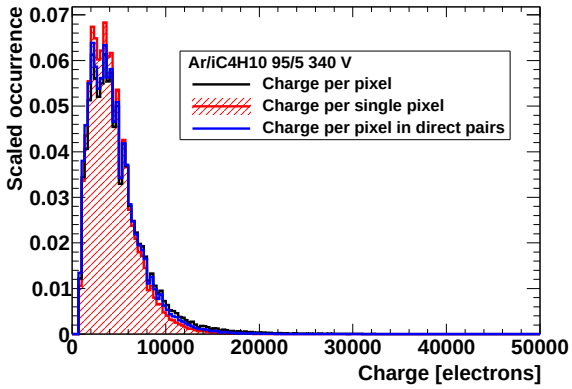

Figure B.5: Charge per pixel at a grid voltage of 340 V. Three kinds of pixels were differentiated: all pixels, isolated pixels and pixels with exactly one neighbor. Histograms have been scaled to have an integrated area of 1.

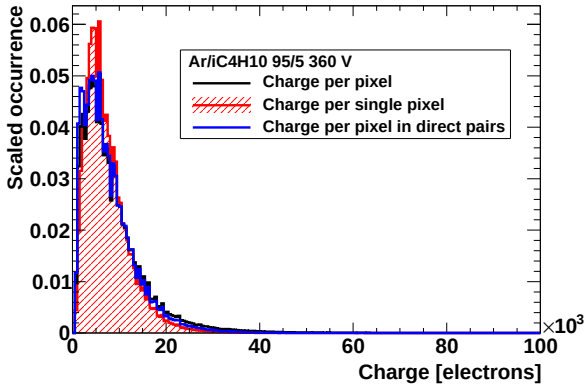

Figure B.6: Charge per pixel at a grid voltage of 360 V. Three kinds of pixels were differentiated: all pixels, isolated pixels and pixels with exactly one neighbor. Histograms have been scaled to have an integrated area of 1.

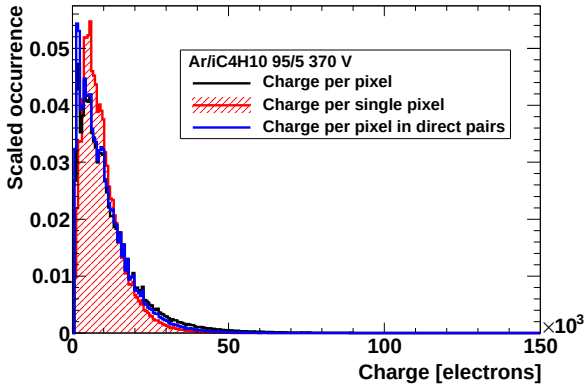

Figure B.7: Charge per pixel at a grid voltage of 370 V. Three kinds of pixels were differentiated: all pixels, isolated pixels and pixels with exactly one neighbor. Histograms have been scaled to have an integrated area of 1.

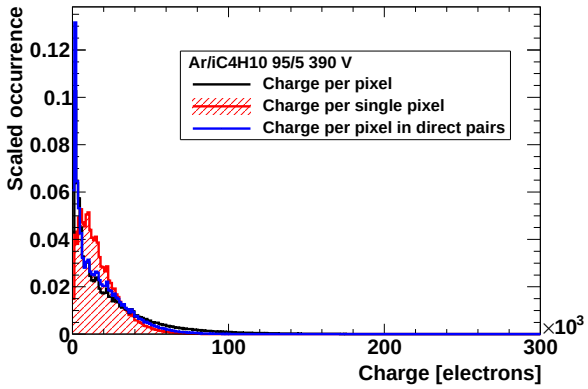

Figure B.8: Charge per pixel at a grid voltage of 390 V. Three kinds of pixels were differentiated: all pixels, isolated pixels and pixels with exactly one neighbor. Histograms have been scaled to have an integrated area of 1.

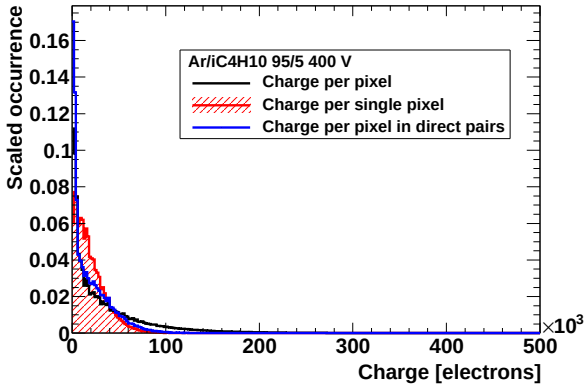

Figure B.9: Charge per pixel at a grid voltage of 400 V. Three kinds of pixels were differentiated: all pixels, isolated pixels and pixels with exactly one neighbor. Histograms have been scaled to have an integrated area of 1.

Bibliography

[1] G. Hinshaw et al. ‘Five-Year Wilkinson Microwave Anisotropy Probe (WMAP) Observations: Data Processing, Sky Maps, and Basic Results’. In: *Astrophys.J.Suppl.* 180 (2009). DOI: 10.1088/0067-0049/180/2/225.

[2] R.D. Peccei and H.R. Quinn. ‘CP Conservation in the Presence of Instantons’. In: *Phys.Rev.Lett.* 38 (1977). DOI: 10.1103/PhysRevLett.38.1440.

[3] S. Weinberg. ‘The U(1) Problem’. In: *Phys.Rev.* D11 (1975). DOI: 10.1103/PhysRevD.11.3583.

[4] G. ’t Hooft. ‘Computation of the Quantum Effects Due to a Four-Dimensional Pseudoparticle’. In: *Phys.Rev.* D14 (1976). DOI: 10.1103/PhysRevD.14.3432.

[5] G. ’t Hooft. ‘Symmetry Breaking Through Bell-Jackiw Anomalies’. In: *Phys.Rev.Lett.* 37 (1976). DOI: 10.1103/PhysRevLett.37.8.

[6] J. Vogel. ‘Probing the eV-mass range for solar axions with the CAST experiment’. PhD thesis. Albert-Ludwigs-Universität Freiburg, 2009.

[7] C.A. Baker et al. ‘An Improved experimental limit on the electric dipole moment of the neutron’. In: *Phys.Rev.Lett.* 97 (2006). DOI: 10.1103/PhysRevLett.97.131801.

[8] S. Weinberg. ‘A New Light Boson?’ In: *Phys.Rev.Lett.* 40 (1978). DOI: 10.1103/PhysRevLett.40.223.

[9] F. Wilczek. ‘Problem of Strong p and t Invariance in the Presence of Instantons’. In: *Phys.Rev.Lett.* 40 (1978). DOI: 10.1103/PhysRevLett.40.279.

[10] J. Galan. ‘Probing eV-mass scale axions with a Micromegas detector in the CAST experiment’. PhD thesis. University of Zaragoza, 2011.

[11] H. Leutwyler. ‘The Ratios of the light quark masses’. In: *Phys.Lett.* B378 (1996). DOI: 10.1016/0370-2693(96)00386-3.

[12] R.D. Peccei and H.R. Quinn. ‘Constraints Imposed by CP Conservation in the Presence of Instantons’. In: *Phys.Rev.* D16 (1977). DOI: 10.1103/PhysRevD.16.1791.

[13] I. Antoniadis and T.N. Truong. ‘Lower bound for branching ration of $K^+ \to \pi^+$ axion and nonexistence of Peccei-Quinn axion’. In: *Phys.Lett.* B109 (1982). DOI: 10.1016/0370-2693(82)90465-8.

[14] M.A. Shifman, A.I. Vainshtein and V.I. Zakharov. ‘Can Confinement Ensure Natural CP Invariance of Strong Interactions?’ In: *Nucl.Phys.* B166 (1980). DOI: 10.1016/0550-3213(80)90209-6.

[15] J.E. Kim. ‘Weak Interaction Singlet and Strong CP Invariance’. In: *Phys.Rev.Lett.* 43 (1979). DOI: 10.1103/PhysRevLett.43.103.

[16] M. Dine, W. Fischler and M. Srednicki. ‘A Simple Solution to the Strong CP Problem with a Harmless Axion’. In: *Phys.Lett.* B104 (1981). DOI: 10.1016/0370-2693(81)90590-6.

[17] X.-L. Chen and M. Kamionkowski. 'Particle decays during the cosmic dark ages'. In: *Phys.Rev.* D70 (2004). DOI: 10.1103/PhysRevD.70.043502.

[18] K. van Bibber et al. 'A practical laboratory detector for solar axions'. In: *Phys.Rev.* D39 (1989). DOI: 10.1103/PhysRevD.39.2089.

[19] P. Sikivie. 'Experimental Tests of the Invisible Axion'. In: *Phys.Rev.Lett.* 51 (1983). DOI: 10.1103/PhysRevLett.51.1415.

[20] C. Hagmann et al. 'Results from a high sensitivity search for cosmic axions'. In: *Phys.Rev.Lett.* 80 (1998). DOI: 10.1103/PhysRevLett.80.2043.

[21] O. Usenko et al. 'A SQUID based read-out of sub-attoNewton force sensor operating at millikelvin temperatures'. In: (2010).

[22] R. Cameron et al. 'Search for nearly massless, weakly coupled particles by optical techniques'. In: *Phys.Rev.* D47 (1993). DOI: 10.1103/PhysRevD.47.3707.

[23] D.M. Lazarus et al. 'A Search for solar axions'. In: *Phys.Rev.Lett.* 69 (1992). DOI: 10.1103/PhysRevLett.69.2333.

[24] S. Moriyama et al. 'Direct search for solar axions by using strong magnetic field and x-ray detectors'. In: *Phys.Lett.* B434 (1998). DOI: 10.1016/S0370-2693(98)00766-7.

[25] S. Andriamonje et al. 'An Improved limit on the axion-photon coupling from the CAST experiment'. In: *JCAP* 0704 (2007). DOI: 10.1088/1475-7516/2007/04/010.

[26] B. Lakic et al. 'Search for solar axions with the CAST experiment'. In: *PoS* IDM2008 (2008).

[27] J.N. Bahcall and M.H. Pinsonneault. 'What do we (not) know theoretically about solar neutrino fluxes?' In: *Phys.Rev.Lett.* 92 (2004). DOI: 10.1103/PhysRevLett.92.121301.

[28] C.E. Aalseth et al. 'A Solar axion search using a decommissioned LHC test magnet: Proposal to the SPSC'. In: (1999).

[29] B. Lizarraga. 'A TPC (Time Projection Chamber) for axion searches in the CAST experiment at CERN'. PhD thesis. University of Zaragoza, 2006.

[30] K. Zioutas et al. 'A Decommissioned LHC model magnet as an axion telescope'. In: *Nucl.Instrum.Meth.* A425 (1999). DOI: 10.1016/S0168-9002(98)01442-9.

[31] K. Zioutas et al. 'First results from the CERN Axion Solar Telescope (CAST)'. In: *Phys.Rev.Lett.* 94 (2005). DOI: 10.1103/PhysRevLett.94.121301.

[32] E. Arik et al. 'Probing eV-scale axions with CAST'. In: *JCAP* 0902 (2009). DOI: 10.1088/1475-7516/2009/02/008.

[33] J. Galan et al. 'Micromegas detectors in the CAST experiment'. In: *JINST* 5 (2010). DOI: 10.1088/1748-0221/5/01/P01009.

[34] F.J. Iguaz et al. 'Ultralow background periods in CAST Micromegas detectors and tests in the Canfranc underground laboratory'. In: *J.Phys.Conf.Ser.* 309 (2011). DOI: 10.1088/1742-6596/309/1/012002.

[35] G. Luzon et al. 'Background studies and shielding effects for the TPC detector of the CAST experiment'. In: *New J.Phys.* 9 (2007). DOI: 10.1088/1367-2630/9/7/208.

[36] C. Grupen. *Particle Detectors*. Cambridge University Press, 1996. ISBN: 0-521-55216-8.

[37] K. Nakamura et al. 'Review of particle physics'. In: *J. Phys.* G37.7A (2010). ISSN: 0954-3899. DOI: 10.1088/0954-3899/37/7A/075021.

[38] W. Blum, W. Riegler and L. Rolandi. *Particle Detection with Drift Chambers*. Second Edition. Springer, 2008. ISBN: 978-3-540-76683-4.

[39] R. Bellazzini and F. Muleri. 'X-ray Polarimetry: a new window on the high energy sky'. In: *Nucl.Instrum.Meth.* A623 (2010). DOI: 10.1016/j.nima.2010.04.006.

[40] E. B. Wagner, F. J. Davis and G. S. Hurst. 'Time-of-Flight Investigations of Electron Transport in Some Atomic and Molecular Gases'. In: 47.9 (1967). ISSN: 00219606. DOI: DOI:10.1063/1.1712365.

[41] M. Chefdeville. 'Development of micromegas-like gaseous detectors using a pixel readout chip as collecting anode'. PhD thesis. University of Amsterdam, 2009.

[42] M. Lupberger. 'Avalanche statistics and single electron counting with a Timepix-InGrid detector'. MA thesis. Albert-Ludwigs Universität Freiburg, 2010.

[43] S. Ramo. 'Currents induced by electron motion'. In: *Proc.Ire.* 27 (1939).

[44] Y. Giomataris et al. 'MICROMEGAS: a high-granularity position-sensitive gaseous detector for high particle-flux environments'. In: *Nucl.Instrum.Meth.* 376.1 (1996). ISSN: 0168-9002. DOI: 10.1016/0168-9002(96)00175-1.

[45] Y. Giomataris. 'Development and prospects of the new gaseous detector "Micromegas"'. In: *Nucl.Instrum.Meth.* 419.2-3 (1998). ISSN: 0168-9002. DOI: 10.1016/S0168-9002(98)00865-1.

[46] A. Delbart et al. 'New developments of Micromegas detector'. In: *Nucl.Instrum.Meth.* 461.1-3 (2001). 8th Pisa Meeting on Advanced Detectors. ISSN: 0168-9002. DOI: 10.1016/S0168-9002(00)01175-X.

[47] I. Giomataris et al. 'Micromegas in a bulk'. In: *Nucl.Instrum.Meth.* 560.2 (2006). ISSN: 0168-9002. DOI: 10.1016/j.nima.2005.12.222.

[48] S. Andriamonje et al. 'Development and performance of Microbulk Micromegas detectors'. In: *JINST* 5 (2010). DOI: 10.1088/1748-0221/5/02/P02001.

[49] S. Cebrian et al. 'Radiopurity of Micromegas readout planes'. In: *Astropart.Phys.* 34 (2011). DOI: 10.1016/j.astropartphys.2010.09.003.

[50] J. Pancin et al. 'Measurement of the n_TOF beam profile with a micromegas detector'. In: *Nucl.Instrum.Meth.* A524 (2004). DOI: 10.1016/j.nima.2004.01.055.

[51] M. Campbell et al. 'Detection of single electrons by means of a Micromegas-covered MediPix2 pixel CMOS readout circuit'. In: *Nucl.Instrum.Meth.* A540.2–3 (2005). ISSN: 0168-9002. DOI: 10.1016/j.nima.2004.11.036.

[52] M. Chefdeville et al. 'An electron-multiplying 'Micromegas' grid made in silicon wafer post-processing technology'. In: *Nucl.Instrum.Meth.* A556.2 (2006). ISSN: 0168-9002. DOI: 10.1016/j.nima.2005.11.065.

[53] Y. Bilevych et al. 'TwinGrid: A wafer post-processed multistage Micro Patterned Gaseous Detector'. In: *Nucl.Instrum.Meth.* 610.3 (2009). ISSN: 0168-9002. DOI: 10.1016/j.nima.2009.09.054.

[54] D.S. Leonard et al. 'Systematic study of trace radioactive impurities in candidate construction materials for EXO-200'. In: *Nucl.Instrum.Meth.* A591 (2008). DOI: 10.1016/j.nima.2008.03.001.

[55] X. Llopart et al. 'Timepix, a 65k programmable pixel readout chip for arrival time, energy and/or photon counting measurements'. In: *Nucl.Instrum.Meth.* 581.1-2 (2007). Proceedings of the 11th International Vienna Conference on Instrumentation. ISSN: 0168-9002. DOI: 10.1016/j.nima.2007.08.079.

[56] F. Krummenacher. 'Pixel detectors with local intelligence: an IC designer point of view'. In: *Nucl.Instrum.Meth.* A305.3 (1991). ISSN: 0168-9002. DOI: 10.1016/0168-9002(91)90152-G.

[57] D. San Segundo Bello. *MUROS2 User's Manual*. An interface board for the Medipix2 chips. URL: http://www.nikhef.nl/pub/experiments/medipix/files/muros2.0_manual.pdf.

[58] T. Holy et al. 'Data acquisition and processing software package for Medipix2'. In: *Nucl.Instrum.Meth.* 563.1 (2006). Proceedings of the 7th International Workshop on Radiation Imaging Detectors. ISSN: 0168-9002. DOI: 10.1016/j.nima.2006.01.122.

[59] D. Turecek et al. 'Pixelman: a multi-platform data acquisition and processing software package for Medipix2, Timepix and Medipix3 detectors'. In: *JINST* 6.01 (2011). DOI: 10.1088/1748-0221/6/01/C01046.

[60] *Honeycomb Strip-Preamplifier*. Strip Front End Electronics.

[61] J. Abernathy et al. 'MarlinTPC: A common software framework for TPC development'. In: *Nuclear Science Symposium Conference Record, 2008. NSS '08. IEEE*. 2008. DOI: 10.1109/NSSMIC.2008.4774731.

[62] R. Ulman. 'Calibration of the Timepix pixel chip for the readout of gaseous particle detectors'. MA thesis. University of Bonn, 2011.

[63] S. Zimmermann. 'Data Reconstruction and Analysis of GEM-Based Time Projection Chambers with Pixel Readout'. MA thesis. University of Bonn, 2008.

[64] M. Matsumoto and T. Nishimura. 'Mersenne twister: a 623-dimensionally equidistributed uniform pseudo-random number generator'. In: *ACM Trans. Model. Comput. Simul.* 8 (1 1998). ISSN: 1049-3301. DOI: 10.1145/272991.272995.

[65] S.F. Biagi. 'Monte Carlo simulation of electron drift and diffusion in counting gases under the influence of electric and magnetic fields'. In: *Nucl.Instrum.Meth.* A421.1-2 (1999). ISSN: 0168-9002. DOI: 10.1016/S0168-9002(98)01233-9.

[66] R. Frühwirth et al. *Data Analysis Techniques for High-Energy Physics*. second edition. Cambridge University Press, 2000. ISBN: 978-0521635486.

List of Figures

List of Tables

Acknowledgements

At the end, I would like to thank all the people which have supported me during my thesis. First of all, I want to thank my mother, Gerlind Krieger for her great financial and mental support. Especially during the final phase of my thesis the latter one was most important. I also would like to thank for the large amounts of moral support provided by my cousins Jana Nöckel and Sandra Thiele who always have been like sisters to me, and their husbands. Furthermore I thank my aunt and uncle, Anke and Dietmar Hartmann and my cousin Peter Krieger, for their encouragement.

I want to thank Prof. Dr. Klaus Desch for the opportunity to write my thesis under his supervision. I also thank the whole group for the great support, the many advises and of course, for the great time I had during my thesis. In this context I want to send a special thank to Dr. Jochen Kaminski for proofreading my thesis.

Last but not least I want to thank the CAST collaboration for giving the opportunity to present the results of my thesis at their collaboration meeting at CERN.

I hereby certify that the work presented here was accomplished by myself and without use of illegitimate means or support, and that no sources and tools were used than those cited.

Bonn, _____ _____

Date Christoph Krieger